University of Tokyo
Graduate School of Science
Department of Physics

# Measuring Stellar Rotation Periods and Stellar Inclinations of Kepler Solar-type Stars (ケプラー衛星の観測した太陽型星に対する自転周期と傾斜角の測定)

**Yuting Lu**

A thesis submitted to

the graduate school of science,

the University of Tokyo

in partial fulfillment of

the requirements for the degree

of

Master of Science in Physics

Jan 2021

# Abstract

The accurate determination of stellar rotation period $P$ and stellar inclination angle $i_*$ has been important in studying the distribution of spin-orbit angle $\psi$ of exoplanetary systems. Spin-orbit angle $\psi$ is the angle between stellar rotational spin and planetary orbital axis. Unlike our solar system, some exoplanetary systems show a misalignment between these two axes. Such misalignment is revealed by the study of a spectroscopic phenomenon, the Rossiter-McLaughlin effect. Most of the misaligned cases reported are hot Jupiter systems due to the selection bias of the spectroscopic RM effect. As spectroscopic RM effect is a minor effect, it can only be detected for systems with giant transiting planets in close orbits. Different theories have been proposed on the origin of such misalignment. However, consensus has not been reached due to the limited sample of observations. The determination of the spin-orbit angle $\psi$ for other types of system is urged.

Nowadays, space missions like CoRoT, Kepler and the TESS provide high quality photometric data for a large number of stars. The precise determination of stellar inclination angle $i_*$, as a complementary constraint on $\psi$, by the asteroseismic analysis becomes possible. Current problem encountered by asteroseismic analysis is the bias of parameter estimation for slow rotators and around $i_*$ close to 0° and 90°. Our work explores three methods in improving the $i_*$ measurement. The first one is to use the photometric estimation of rotation period as a prior for asteroseismic analysis. For this purpose, we examine the three widely used photometric analyses and then discuss about the suitability of using photometric periods as priors for extracting $i_*$. The remaining two methods modify the mostly used strategy in fitting stellar oscillation pattern. This last part is an ongoing project. Our main findings are summarized as follows:

- Firstly, we measure the rotation period for 91 solar type stars using three photometric methods. Three photometric analyses show more than 80% consistency within $1\sigma$ uncertainty in their measurement. Discrepancy occurs when there are multiple periodic signals with different period in the light curve. Photometric analyses are not able to distinguish between the signal of rotation period and that of contamination from other light source. Hence, we classify our targets into two groups, a reliable $P_{\mathrm{photo}}$ group (22/91) where targets have only one dominant peak in their power spectra and a less reliable $P_{\mathrm{photo}}$ group (69/91) where multiple signals are found in the light curve of targets.

- We combine our $P_{\mathrm{photo}}$ with stellar radius $R$ to give estimations of rotational velocities $v$. Then we compare our result with reliable spectroscopic estimations of $v \sin i_*$ for 25 targets, 9 from reliable $P_{\mathrm{photo}}$ group and 14 from less reliable $P_{\mathrm{photo}}$ group. Only 2/25 targets from less reliable $P_{\mathrm{photo}}$ group lie in physically unreasonable region ($\sin i_* < 1$). Hence, the reliability of photometric period is validated by spectroscopic analysis.

- Next, we compare our $P_{\mathrm{photo}}$ with asteroseismic estimations $P_{\mathrm{astero}}$ from Kamiaka et al. (2018). Kamiaka et al. (2018) also divide their targets into reliable $P_{astero}$ group and less reliable $P_{\mathrm{astero}}$ group. A general comparison for all targets gives $\sim 80\%$ consistency. For targets with reliable $P_{\mathrm{photo}}$ and $P_{\mathrm{astero}}$, 7 out of 8 targets show good consistency within $1\sigma$ uncertainty. For the remaining one target, KIC 5773345, we suggest that either differential rotation or presence of close companion lead to the discrepancy between estimations from different approaches. Hence, We think that $P_{\mathrm{photo}}$ are suitable choices for priors in asteroseismic analysis when they meet two criteria. Firstly, in the power spectra of photometric analysis of the target, there is only one dominant peak. Secondly, $P_{\mathrm{photo}}$ has overlapped $1\sigma$ confidence regions with $P_{\mathrm{astero}}$. From our sample, we identify 3 candidates that fit the requirement, which are one planet hosting star KIC 3425851 and two planet-less stars KIC 9098294 and KIC 1225851.

- Finally, we attempt additional two methods that might improve the accuracy of the stellar inclination $i$ measurements using asteroseismic analysis. Firstly, instead of traditional global fitting, We apply local fitting to slices of power spectrum. Then we average the posterior samples of inclination angle $i_*$ using a Hierarchical Bayesian inference. This method improve the measurement around $i_* \sim 0°$ and $90°$. However, we spot a large underestimation of $i_*$ from input value in the range of $i \in [20.40°]$ with this attempt. Our second approach is to remove the influence of non-linear relation between the mode height H and the stellar inclination $i_*$ from the global fitting. We perform the global fitting of power spectrum by fitting the mode Height H directly instead of $i_*$ and then derive inclination angle independently using posterior arrays of H. This approach aims to test whether the introduction of non-linear relation between mode height H and $i_*$ jeopardizes the fitting of spectrum. This attempt does not improve much the results comparing to traditional global fitting which indicates that the non-linear relation is not largely responsible for the inaccuracy in asteroseismic estimations.

# Acknowledgements

I would like to express my deepest gratitude to my supervisor, Prof. Yasushi Suto, for his continuous support, enlightening discussions and patient mentoring during the past two years. Next, I would like to thank Dr. Othman Benomar for his insightful suggestions, constant guidance and great encouragement. I would also like to thank my defence committee members, Prof. Fujihiro Hamba and Prof. Hiroya Yamaguchi for their constructive suggestions on this thesis as well as my future research. I would like to thank Dr. Masataka Aizawa who led me into the field of Kepler data analysis and UTAP/RESCEU members who contributed to fruitful discussions of this project. Finally I would like to extend my appreciation to my parents who provide me with tremendous support both mentally and financially.

# Contents

**Abstract** **i**

**Acknowledgements** **iii**

**1 Introduction** **1**

**2 Spin-orbit Angles of Exoplanetary Systems** **4**

2.1 On The Origin of Spin-Orbit Misalignment . . . . . . . . . . . . . . . . . . . . . . 4

2.2 Methods to Constrain The Spin-Orbit Angle $\psi$ . . . . . . . . . . . . . . . . . . . . 6

2.2.1 The Projected Spin-orbit Angle $\lambda$ . . . . . . . . . . . . . . . . . . . . . . 7

2.2.2 The Stellar Inclination Angles $i_*$ . . . . . . . . . . . . . . . . . . . . . . 9

2.2.3 The planetary orbital inclination $i_{\rm orb}$ . . . . . . . . . . . . . . . . . . . 11

2.3 Constraints on Spin-orbit Angle From Stellar Inclination . . . . . . . . . . . . 12

**3 Stellar Rotation Period** **14**

3.1 Introduction . . . . . . . . . . . . . . . . . . . . . . . . . . . . . . . . . . . . 14

3.2 Target Selection . . . . . . . . . . . . . . . . . . . . . . . . . . . . . . . . . . 17

3.3 Preparation of Light Curves . . . . . . . . . . . . . . . . . . . . . . . . . . . 18

3.4 Method . . . . . . . . . . . . . . . . . . . . . . . . . . . . . . . . . . . . . . . 21

3.4.1 The Lomb-Scargle Periodogram . . . . . . . . . . . . . . . . . . . . . . . 21

3.4.2 The Auto-correlation Function . . . . . . . . . . . . . . . . . . . . . . . . 24

3.4.3 Wavelet Analysis . . . . . . . . . . . . . . . . . . . . . . . . . . . . . 26

3.5 Results and Discussion: Stellar Rotation Period . . . . . . . . . . . . . . . . . . . . 29

3.5.1 Comparison with Previous Photometric Analysis . . . . . . . . . . . . . 29

3.5.2 Comparison Among Three Photometric Method . . . . . . . . . . . . . 32

3.5.3 Classification . . . . . . . . . . . . . . . . . . . . . . . . . . . . . 35

3.5.4 Comparison with Spectroscopic Analysis . . . . . . . . . . . . . . . . . . . 35

3.5.5 Comparison with Asteroseismic Analysis . . . . . . . . . . . . . . . . . . . 37

3.6 Conclusion and Future Perspective . . . . . . . . . . . . . . . . . . . . . . . 42

**4 Asteroseismic Analysis of Stellar Inclination Angle 45**

4.1 Motivation . . . . . . . . . . . . . . . . . . . . . . . . . . . . . . . . . . . 45

4.2 Model of Stellar Oscillation Spectrum . . . . . . . . . . . . . . . . . . . . . 45

4.3 Past Attempt to Extract Stellar Parameters . . . . . . . . . . . . . . . . . . 47

4.4 Method . . . . . . . . . . . . . . . . . . . . . . . . . . . . . . . . . . . . 49

4.4.1 Hierarchical Bayesian Model . . . . . . . . . . . . . . . . . . . . . . 51

4.4.2 Fitting of Mode Height H . . . . . . . . . . . . . . . . . . . . . . . 55

4.5 Results . . . . . . . . . . . . . . . . . . . . . . . . . . . . . . . . . . . . . 56

**5 Conclusion and Future Work 59**

**A Appendix 61**

A.1 Modeled Power Spectrum of Asteroseismic Analysis . . . . . . . . . . . . . . . . 61

A.2 Stellar Rotation Period of 91 Solar Type Stars . . . . . . . . . . . . . . . . . . . 62

**Bibliography 62**

# List of Tables

2.1 Summary of exoplanetary systems with spin-orbit angle $\psi$ measured. . . . . . . 13

4.1 Grids of the control parameters for simulation of power spectra. . . . . . . . . . 51

4.2 Parameters and priors for fitting of $l = 1$ mode of power spectrum . . . . . . . . 54

A.1 Stellar rotation period. . . . . . . . . . . . . . . . . . . . . . . . . . . . . . . . 63

A.2 Stellar rotation period. . . . . . . . . . . . . . . . . . . . . . . . . . . . . . . . 64

A.3 Stellar rotation period. . . . . . . . . . . . . . . . . . . . . . . . . . . . . . . . 65

A.4 Stellar rotation period. . . . . . . . . . . . . . . . . . . . . . . . . . . . . . . . 66

A.5 Stellar rotation period. . . . . . . . . . . . . . . . . . . . . . . . . . . . . . . . 67

# List of Figures

1.1 Cumulative histogram for number of planets detected. Figure credits to NASA11[1]. 2

2.1 Sky-projected spin-orbit angle as a function of the stellar effective temperature for 110 transiting hot Jupiter systems. We define stars with temperature $T < 6100K$ as cool star and those with $T > 6100K$ as hot star (see e.g. Kraft, 1967). Large spin-orbit misalignments are observed in systems with hot stars. (Data from TEPCat, Southworth, 2011) . . . . . . . . . . . . . . . . . . . . . . . . . . 5

2.2 Schematic illustration of the geometry of star-planet system. The coordinate system is centered on the star with $+Z$ axis pointing towards observer and $+Y$ axis in the direction of sky projected stellar spin.The red dot represents the host star of the exoplanetary system. The red arrow is the stellar rotational spin and the green arrow is the planetary orbital axis. . . . . . . . . . . . . . . . . . . . . . 7

2.3 Pole on views of an exoplanetary system which illustrates of the configuration which causes the Rossiter-McLaughlin effect. The black circle is the orbit of a planet. In this plot, an aligned stellar rotation spin and planetary orbital axis is assumed. The stellar inclination relative to the line of sight is 90°. As the planet move in front of its host star with respect to the observer, it blocks a part of light from the star. . . . . . . . . . . . . . . . . . . . . . . . . . . . . . . . 8

2.4 Schematic illustration of radial velocity anomaly due to the Rossiter-McLaughlin effect for different values of projected spin-orbit angle $\lambda$. $\lambda = 0^\circ$ represents an aligned system. The blue curve is the radial velocity curve when the planet transits and the dotted line shows the curve when the planet does not. Figure adapted from Gaudi & Winn (2007). . . . . . . . . . . . . . . . . . . . . . . 8

2.5 Schematic illustration of planetary transit with impact parameter b. Transit of planet causes a dipping with flux variation $\delta$. Figure adapted from Winn (2010). 11

3.1 Figure of sunspots on solar surface. The upper panel shows a series of shots for one spotted region as it rotates with the Sun. The bottom panel shows a enlarged version of the region. The darkest part in the center of spot is the umbra and the slightly brighter region in peripheral is the penumbra. Credit to NASA/SOHO `https://sohowww.nascom.nasa.gov/home.html`. . . . . . . . . . 15

3.2 Butterfly diagram of the Sunspot. Y-axis is the latitude. X-axis is the Date. This plot illustrates the change of spot distribution over the 11-year solar cycle. The color mark indicates the % of band area covered by spots. Credit to Hathaway at NASA Marshall Space Flight Center `http://SolarCycleScience.com`. . . . 16

3.3 A depiction of Kepler's field of view. Each square represents the view of a CCD module composed of 2 CCDs. Credit to NASA `www.nasa.gov/mission_pages/kepler/multimedia/images/fov-kepler-drawing.html`. . . . . . . . . . . . . 17

3.4 HR diagram in the form of surface gravity vs effective temperature. The 94 solar-type stars in the sample of Kamiaka et al. (2018) is plotted. The blue circles represent the planet host stars (KOI stars) and the red circle represent the planet less stars. Plot adopted from the doctoral thesis of Shoya Kamiaka. . 18

3.5 Normalized Q2-Q14 light curve from KIC 7206837, which is one of our target with no reported planet detection. The normalized flux is in the unit of parts per million (ppm). The black dotted lines mark the boundary between quarters. 19

3.6 An example of light curve with sudden increase in flux variation within single quarters. Normalized Q2-Q14 light curve from KIC 4141376. Q4, Q8, and Q12 shows the sudden increase in flux variation. The variations only retain within these quarters themselves with no gradual transition from nearby quarters. We remove these quarters from the light curve. . . . . . . . . . . . . . . . . . . . . . 20

3.7 A section of normalized light curve from KIC 8349582 (top panel) and phase folded light curve at the planetary orbital period $P_{orb}$ from KIC 8349582 (bottom panel). The red triangles point at the transit dips in the light curve. In the phase folded light curve, the red bars mark the regions of transit dips and possible eclipse dips. We removed these regions from the light curve. . . . . . . . . . . 21

3.8 Examples of power spectra computed using differently padded light curve for KIC 10963065 (subplot (a) and (c))and KIC 4141376 (subplot (b) and (d)). The upper panel of each subplot shows the padded light curve and the bottom panel shows the power spectrum (LS periodogram) computed from the light curve. LS periodogram is one of the methods we applied to extract rotation period which will be introduced in the following section. Power spectra of differently padded light curve show high resemblance. KIC 4141376 represents an extreme case found in only 2 of our targets, where the highest peak (choice of rotation period) in the power spectra differs for differently padded light curve. 89 out of 91 targets shows consistent estimations of period within the error using different padding schemes as KIC 10963065. . . . . . . . . . . . . . . . . . . . . . . . 22

3.9 Flow diagram of light curve preparation. . . . . . . . . . . . . . . . . . . . . . . 23

3.10 Examples of original (upper panel) and smoothed (bottom panel) ACF (KIC8292840). This example illustrates the aliases which are most likely caused by three active regions with near uniform distribution along longitude on the stellar surface. In the upper panel, the peak of actual period $P$ is modulated by a higher frequency signal with $P/3$, leading to three additional small peaks around each the of period $P$. The red arrows marked the three aliasing peaks. After applying the smoothing function (bottom panel), the influence of aliases on ACF is removed. 25

3.11 An example of smoothed ACF (KIC 7296438) which does not have clear repetitive maxima. . . . . . . . . . . . . . . . . . . . . . . . . . . . . . . . . . . . 25

3.12 Examples of three Morlet wavelets with scale s = 10, 5 and 1 days respectively from top to bottom panels. Scale s corresponds to the period of variation in the Morlet wavelet. . . . . . . . . . . . . . . . . . . . . . . . . . . . . . . . . . . 26

3.13 Power spectra given by wavelet analysis of KIC 3425851. The left panel is the wavelet power spectrum. The vertical axis is period. The horizontal axis is time. The shaded region near the bottom edge of the waver power spectrum is the cone of influence within which power is less reliable. In the right panel, blue curve is the global wave power spectrum (GWPS) and the gray curve shows the Fourier power spectrum of the light curve. . . . . . . . . . . . . . . . . . . . . . . . . . 28

3.14 Comparison of LS method (15 targets). The x-axis is our LS estimation and the y-axis is the LS results from the other two literatures. . . . . . . . . . . . . . . 29

3.15 Lomb-Scargle periodogram of KIC 9139151. The highest peak at $P = 6.3\,\text{days}$ selected by our method is marked by the blue vertical line. The period selected by Karoff et al. (2013) is marked by red bar around $P = 10.4\,\text{days}$. This is an example of inconsistent estimations for LS method. . . . . . . . . . . . . . . . . 30

3.16 Comparison of ACF method (21 targets). The x-axis is our ACF estimation and the y-axis is the ACF results from the other two literatures. . . . . . . . . . . 30

3.17 Comparison of rotation period between our work and previous literature for 41 targets. In plot(a), we use our ACF results for comparison. In plot (b), we use our wavelet results for comparison. In all plots, our estimations are plotted in x-axis. . . . . . . . . . . . . . . . . . . . . . . . . . . . . . . . . . . 31

3.18 Comparison of estimations from different photometric method. Y-axis is the ratio of period from each method to period of wavelet. X-axis is the periods from wavelet method . . . . . . . . . . . . . . . . . . . . . . . . . . . . . 33

3.19 Global wavelet power spectrum, LS periodogram, ACF spectrum of KIC 3425851. The power spectra are dominated by one significant peak, which indicates that the light curve contains a rather homogeneous periodic signal. Estimations from three photometric analyses agree well within uncertainty. . . . . . . . . . . . . 33

3.20 Global wavelet power spectrum, LS periodogram, ACF spectrum of KIC 10068307. There are multiple significant peaks at the same location in the power spectra of all photometric methods. LS and ACF method choose the peak at smaller period while wavelet method chooses the peak at larger period. . . . . . . . . . 34

3.21 Plot of projected rotational velocity $v \sin i$ from spectroscopic analysis against rotational velocity $v$ computed using $P$ from three photometric analyses. $v_* \sin i_*$ measurements come from California-Kepler Survey (CKS:$california - planet - search.github.io/cks - website$). The shaded region is the non-physical region where $\sin i_* > 1$. Corresponding $P_{photo}$ for targets in shaded region should not be trusted. . . . . . . . . . . . . . . . . . . . . . . . . . . . . . . . . . . 36

3.22 Comparison of rotation period for targets with reliable $P_{\text{astero}}$ and $P_{\text{photo}}$. X-axis is the index assigned to each target. In table in Appendix A.2, we can locate each target with this index. Y-axis is the ratio of period $P_{\text{method}}/\left\langle P_{\text{wavelet}}\right\rangle$. For these 10 targets, all but one show good consistency within $1\sigma$ uncertainty between photometric methods and asteroseismic analysis. . . . . . . . . . . . . . . . . . 37

3.23 Power spectra of photometric analyses (KIC 5773345). $P_{\text{photo}} \approx 11\,\text{days}$ while $P_{\text{astero}} = 5.43\,\text{days}$. . . . . . . . . . . . . . . . . . . . . . . . . . . . 38

3.24 Image of KIC 5773345 and its surrounding field of radius $r \sim 30$ arcsec from DDS2 (Digitized Sky Survey - STScI/NASA). The blue box mark the target identified in Gaia EDR3 (Brown et al., 2020). The central star is KIC 5773345. . 39

3.25 Comparison of rotation period from photometric analysis and asteroseismic analysis. X-axis is the index assigned to each target. In table in Appendix A.2, we can locate each target with this index. Y-axis is the ratio of period $P_{\text{method}}/\left\langle P_{\text{wavelet}}\right\rangle$. The overall comparison between asteroseismic estimations and photometric results (from at least one method) shows more than 80% consistency within $1\sigma$ uncertainty. . . . . . . . . . . . . . . . . . . . . . . . . . . . . . . . . . . . . . 40

3.26 Asteroseismic results of KIC 12258514. Top left, bottom left and bottom right panels give posterior distribution of $\delta\nu$, $\delta\nu \sin i_*$ and $i_*$ respectively. The green solid line marks the median of each distribution and the dashed lines indicate the $1\sigma$ confidence interval. Top right panel is the correlation plot of $\delta\nu$ and $i_*$. We can see the correlation between $P$ and $i_*$ in the correlation plot. The red line marks the rotational frequency indicated by photometric analysis. A prior from photometric analysis could largely improve the precision of $i_*$ measurement. Data adopted from Kamiaka et al. (2018). . . . . . . . . . . . . . . . . . . . . . 42

4.1 Asteroseismic results of KIC 8077173. Top left, bottom left and bottom right plots give posterior distribution of $\delta\nu$, $\delta\nu \sin i_*$ and $i_*$ respectively. Top right is the correlation plot of $\delta\nu$ and $i_*$. The green solid line marks the median of each distribution and the dashed lines indicate the $1\sigma$ confidence interval. Data adopted from Kamiaka et al. (2018). . . . . . . . . . . . . . . . . . . . . . . . . . 46

4.2 Power spectrum of KIC 12069424. Black and Grey curve are power spectra smoothed with Gaussian filters of width $0.25\Delta \approx 25.5\mu Hz$ and $0.05\Delta \approx 5.2\mu Hz$ respectively. Red curve is the ground level and blue curve is the fitted power spectrum. Plot is adopted from Kamiaka et al. (2018). . . . . . . . . . . . . . 48

4.3 Schematic illustration of power spectrum of $l = 1$ mode. Rotation splits the $l = 1$ mode into 3 different $m$ modes. Blue dotted line represents $m = 0$ mode and red dotted lines show $m = 1/-1$ peaks. $\delta\nu$ is the splitting between different $m$ modes and $\Gamma$ represents the width of peaks (Kamiaka et al., 2018). . . . . . . 50

4.4 Schematic illustration of 1-level Bayesian model(left) and 2-level hierarchical Bayesian model(right). . . . . . . . . . . . . . . . . . . . . . . . . . . . . . . . . . 52

4.5 Measurements of inclination angle $i_*$ plotted against input value $i_*$ using global fitting (orange) and HBI (green). . . . . . . . . . . . . . . . . . . . . . . . . . 57

4.6 Estimations of $\delta\nu_*/\Gamma$ and stellar inclination angle $cosi_*$. The red line is given by our fitting of height method and the black line is from Kamiaka et al. (2018) using the global fitting. . . . . . . . . . . . . . . . . . . . . . . . . . . . . . 58

# Chapter 1

# Introduction

Determining the stellar rotation period is important for various fields such as stellar evolution, stellar dynamo, and the formation and evolution of exoplanetary system. We are particularly interested in its contribution to determine of spin-orbit angles of exoplanetary systems. In the following paragraphs, we will start by giving a brief review of current exoplanet detection. Then we discuss about why the determination of spin-orbit angles is important in exoplanetary science. Finally we talk about how the accurate measurement of stellar rotation period contributes to the estimation of spin-orbit angles.

In 1995, Mayor & Queloz (1995) detected the first exoplanet around a solar type star via spectroscopic observation of stellar radial velocity. Since then, more attentions were drawn to exoplanetary science and the number of exoplanets discovered increased in a steady pace. At that time, the major technique to detect planets was the radial velocity of stars (spectroscopy). After the Launch of the Kepler telescope (Borucki et al., 2010) in 2009, high quality photometric data for more than 500,000 stars become available. Regular dips are found in the light curve (photometric data) of some stars. These dips are considered as the signatures of planets which occur as the planet move in front of its host star and block a part of the stellar flux. Transiting signal of planets has since become a powerful indicator of exoplanetary systems. With the help of this transit method, the number of exoplanets detected starts to soar. Figure 1.1 shows the cumulative number of planet detection from the late 20th century to now. Nowadays, there are more than 4000 confirmed exoplanets[1], most of which have been discovered by transit method. The ongoing space mission, TESS (Ricker et al., 2015), has continuously provided us with new photometric data. We are now in the golden age of exoplanet exploration.

An intriguing discovery that caught our attention is the significant misalignment between the stellar rotational spin and the planetary orbital axis found in some exoplanetary systems, which is very different from our solar system. In our solar system, the orbits of planets are nearly coplaner, and the angles between orbital axes and the solar rotation spin (spin-orbit angles $\psi$) are less then 7°. One might easily expect to see such good alignments for all exoplanetary systems. However, a spectroscopic phenomenon called the Rossiter-McLaughlin effect (Rossiter, 1924; McLaughlin, 1924) reveals a different picture. As a star rotates, half of its light is blue shifted and half is red-shifted. However, when a planet transits its host stars, it blocks the light from different regions of the apparent disk of the star during its passage. Such blocking breaks the

---

[1] NASA Exoplanet Archive: `https://exoplanetarchive.ipac.caltech.edu`. Accessed date:Dec 2020

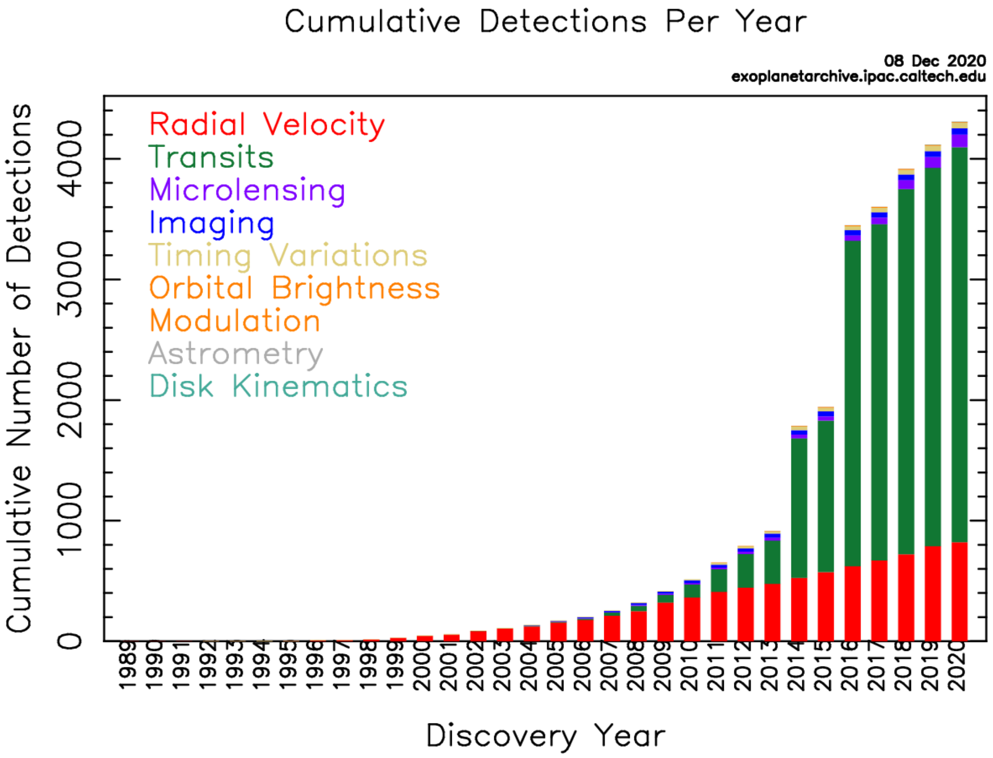

Figure 1.1: Cumulative histogram for number of planets detected. Figure credits to NASA[1].

symmetry and causes a pseudo-shift of the spectral line. This spectroscopic phenomenon is named the Rossiter-McLaughlin effect.

The Rossiter-McLaughlin effect contains the information of the sky projected spin-orbit angle $\lambda$. By modeling this effect, a wide range of projected spin-orbit angles are reported, with some systems exhibiting very significant misalignments. Two extreme examples are WASP-7 and WASP-17: the former system has $\lambda \sim 90°$, while the latter system has $\lambda > 90°$, meaning the planet is in retrograde orbit. However, the application of the Rossiter-McLaughlin effect has its own limitation. Since the Rossiter-McLaughlin effect is just a mild anomaly, it can only be resolved by high resolution spectrographs. In addition, since the amplitude of such effect is positively related to the transit depth of the planet, this method has a strong selection bias towards systems with giant planets in close orbits. Indeed, most systems with reported $\lambda$ measurements are hot Jupiter systems which perfectly fit the requirement for the Rossiter-McLaughlin effect. An important question then follows: is the misalignment confined to a specific type of exoplanetary systems? To get the answer, we need to examine more exoplanetary systems, meaning that we have to rely on alternative methods to measure the misalignment.

After the advent of space missions (e.g. Kepler and TESS) at the beginning of this century, the photometric and asteroseismic analyses become increasingly popular. Reliable estimation of stellar parameters such as the rotational period and the inclination angle $i_*$ relative to our line of sight become possible for a large group of stars. With the additional information, the spin-orbit angle $\psi$ can then be constrained from a new perspective. For a transiting planet, we can assume that planetary orbital axis is nearly perpendicular to our line of sight. With estimation of stellar inclination angle $i_*$, we can set a lower limit for the spin-orbit angle $\psi$.

There are two methods to measure the stellar inclination angle $i_*$. The first one is a composite method of photometric analysis and spectroscopic analysis. The photometric analysis estimates the stellar rotation period P by studying the periodic variation of stellar flux caused by the rotations of active region on the stellar surface. Then with the help of rotational velocity $v \sin i_*$ from spectroscopic analysis as well as stellar radius $R$ from the stellar evolution model, we can obtain the stellar inclination angle from $i_* = \sin^{-1}\left(\frac{v_* \sin i_* P_{\mathrm{rot}}}{2\pi R_*}\right)$ (e.g. Hirano et al., 2012, 2014; Kovacs, Geza, 2018).

The second approach is the asteroseismic analysis. Asteroseismology studies the pulsations of stars induced by the interplay between gravity and pressure within the star. These stellar oscillations show regular patterns in the power spectrum. The information of the stellar inclination angle $i_*$ and stellar rotation period $P$ is encoded in these patterns. Hence, by modeling the oscillation patterns, we can obtain both parameters. One problem that asteroseismic analysis faces is a coupling between $P$ and $i_*$ in the fitting of pulsation model which leads to a possible bias in the estimation of both parameters. Another problem is the low precision of estimation when signal to noise ratio is relatively low (see e.g. Kamiaka et al., 2018). A possible solution to these problems is to provide a reliable prior knowledge of the rotation period $P$ to the fitting. Photometric analysis of rotation period could potentially be a good candidate for this purpose, the suitability of which will be discussed in this thesis.

In both methods, the photometric analysis of rotation period $P$ plays an important part. Hence, in our project, we explore the reliability of photometric analyses by examining the three widely used photometric methods: Lomb-Scargle periodogram (LS) (Lomb, 1976; Scargle, 1982), Autocorrelation function (ACF) (see e.g. McQuillan et al., 2014), and wavelet analysis (see e.g. Torrence & Compo, 1998; García et al., 2014). Then, we discuss the suitability of using the photometric period $P$ as the prior in asteroseismic analysis. Finally, we introduce some other ongoing attempts that we made to improve the asteroseismic estimation of stellar inclination angle $i_*$.

This thesis is organized as follows. In Chapter 2, we first discuss about several proposed theories on the origin of misalignment between stellar spin and planetary orbital axis. Then, we give a more detail account of the methods to constrain the spin-orbit angle. Finally, we introduce the current updates in the measurement of spin-orbit angle and our motivation. In Chapter 3, we estimate the stellar rotation period of 91 solar-type stars with three photometric methods. Then we examine the reliability of photometric estimations by comparing them with the spectroscopic and asteroseismic measurements. Finally, we discuss about the suitability of using the photometric period $P$ as a prior to improve the asteroseismic analysis of stellar inclination $i_*$. In Chapter 4, we introduce some other ongoing attempts to improve asteroseismic analysis. In Chapter 5, we summarize the findings of this thesis and discuss future perspectives of our study.

# Chapter 2

# Spin-orbit Angles of Exoplanetary Systems

## 2.1 On The Origin of Spin-Orbit Misalignment

The misalignment between the stellar spin and the planetary orbital axis has been one of the most intriguing discoveries from the exploration of exoplanetary systems. In our solar system, the solar rotation spin and the planetary orbital axis is nearly aligned, with the spin-orbit angle $\psi \approx 7^\circ$. The measurement of sky projected spin-orbit angles $\lambda$ by the Rossiter-McLaughlin effect indicates that in exoplanetary systems, the spin-orbit angles $\psi$ are diverse. Examples include WASP-7 which has $\lambda \approx 90^\circ$ (Albrecht et al., 2011) and HAT-P-7 with $\lambda$ even larger than 90° (Winn et al., 2009).

As most of the discovered misaligned systems are hot Jupiter systems, the origin of misalignments has been linked with the formation mechanism of hot Jupiter. The two most well known scenarios are the Lidov-Kozai mechanism and the planet-planet scattering. The Lidov-Kozai mechanism (Lidov, 1962; Kozai, 1962) states that for a hierarchical triple system where a near-circular orbit of the inner binary system is perturbed by a distant third body, there will be a periodic exchange between eccentricity and inclination of the orbit if the initial mutual inclination between the inner and outer orbits is within the range $i_{\text{mut}} \in [i_{\text{crit}}, 180^\circ - i_{\text{crit}}]$ with:

$$i_{\text{crit}} = \arccos(\sqrt{\frac{3}{5}}) \approx 39.2^\circ. \tag{2.1}$$

This scenario applies to systems with an orbiting planet and a distant perturber. As the planet orbits around its host stars, the distant perturber excites the oscillations of orbital inclination and eccentricity. The periapsis of the planetary orbit moves closer to the star as the orbit becomes more eccentric. The host star then gradually circularizes the planetary orbit through their tidal interaction, while leaving the inclination of orbital plane intact. Accordingly, the planet settles in a close orbit around the star with a large spin-orbit angle (Fabrycky & Tremaine, 2007; Naoz et al., 2011).

The second scenario is the planet-planet scattering mechanism proposed by Chatterjee et al. (2008). In a planetary system where multiple giant planets are formed, there are mutual gravitational interactions among planets. The perturbations increase the orbital eccentricity to an extent that planetary orbits overlap (Lin & Ida, 1997). The close encounters of the planets randomize the eccentricity and inclination of their orbits, and consequently tilt the planetary orbital axes relative to the stellar rotation spin of the central star. The subsequent circularization combined with occasional large eccentricity could move the giant misaligned planet to a close-in orbit. As a result, the hot Jupiter system with a spin-orbit misalignment forms.

Some other theories suggested that the misalignment is not confined to hot Jupiter systems and could have existed even before planets form. Batygin (2012) proposed that the spin-orbit misalignment may be a typical outcome of disk migration in binary systems. At the initial state of the exoplanetary system when planets are not yet formed, the central star of the system is surrounded by a proto-planetary disk. If the star happens to be in a binary system, its distant companion could cause a precession of the proto-planetary disk with respect to the stellar binary orbital axis. Such precession then excites the misalignment between the stellar spin and the rotation spin of the disk which is later inherited by the planet (see also e.g. Lai et al., 2011).

Bate et al. (2010) alternatively suggested that the misalignment could come from the turbulent molecular cloud where star and planetary disc form. They proposed that if the planetary disc is truncated by dynamical encounters, its spin could be tilted relative to the stellar spin. Consequently, the planet formed from the disc will have a misaligned orbital axis relative to the rotation spin of its host star. However, this theory is challenged by Takaishi et al. (2020) who found that the angle between the rotation spins of star and disc always converges to a value smaller than 20°, regardless of the initial value.

Observations of projected spin-orbit angle $\lambda$ reveal an interesting pattern that systems with hot stars ($T > 6100\,\mathrm{K}$) tend to have a wider range of spin-orbit angles $\psi$ than those with cold stars (see Figure 2.1).

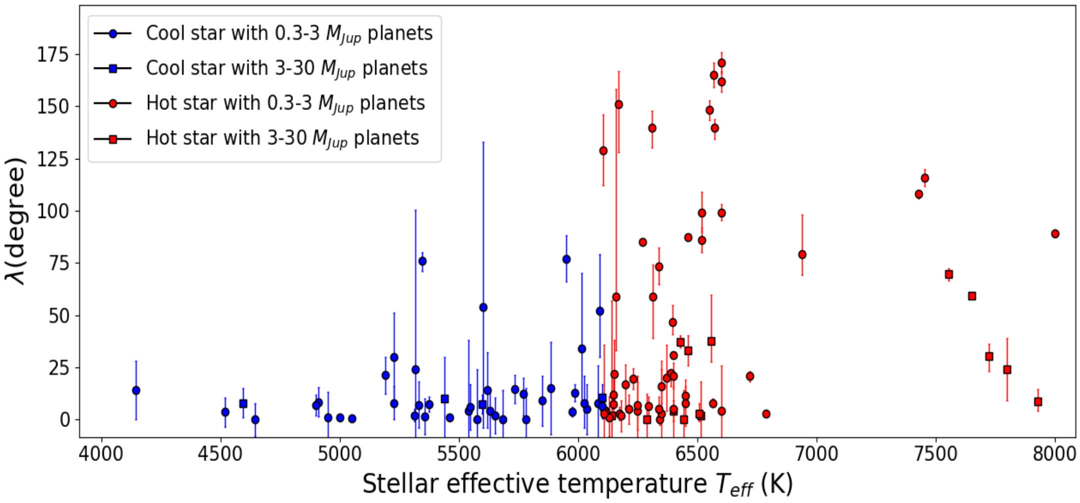

Figure 2.1: Sky-projected spin-orbit angle as a function of the stellar effective temperature for 110 transiting hot Jupiter systems. We define stars with temperature $T < 6100K$ as cool star and those with $T > 6100K$ as hot star (see e.g. Kraft, 1967). Large spin-orbit misalignments are observed in systems with hot stars. (Data from TEPCat, Southworth, 2011)

Winn et al. (2010) explained this obliquity pattern using realignment mechanism of cool stars.

They suggested that hot Jupiter systems begin with a broad range of spin-orbit angles. Cool stars realign the stellar spins with planetary orbital axes through tidal dissipation in their convective zone. Hot stars with thin convective zone retain their original tilt relative to planetary orbital spin.

Alternatively, Rogers et al. (2012) proposed a theory using the effect of internal gravity waves. Rogers et al. (2012) assumed that the stellar rotation spin and planetary orbital axis are relatively aligned initially. Internal gravity waves, which are generated at the layer between the core and radiative envelope of star, transport the angular momentum outwards. The angular momentum will eventually dissipate near the stellar surface and change the rotation configurations such as the rotational spin of the star. Such mechanism only applies to hot stars with mostly radiative envelope, so that only the stellar spin of hot stars could be tilted relative to planetary orbital axis.

Spalding & Batygin (2015) further elaborated the disc precession scenario brought up by Batygin (2012). They state that the planetary orbit inherited from the proto-planetary disc could be tilted relative to the rotational axis of their host star under the influence of a distant companion. However, the strong magnetic field of low mass stars, which are usually cool stars (Gregory et al., 2012; Alecian et al., 2013), realigns the stellar spin and disk. Consequently, large spin-orbit misalignments are mostly found in systems with hot stars.

The origin of spin-orbit misalignment remains as one of the most intriguing mysteries in exoplanetary science. More observational data, especially for other types of systems, are urged for further clarification. In the following section, we introduce mostly used methods to constrain the spin-orbit angle.

## 2.2 Methods to Constrain The Spin-Orbit Angle $\psi$

The spin-orbit angle $\psi$ can not be directly measured. Instead, it is constrained by three observables, the projected spin-orbit angle $\lambda$, the stellar inclination angle $i_*$, and the planetary orbital inclination angle, $i_{\mathrm{orb}}$. Figure 2.2 illustrates the geometry of the spin orbit angle $\psi$. Z-axis is the line of sight. The stellar spin vector $\boldsymbol{s}$ and planetary orbital spin vector $\boldsymbol{l}$ are expressed as

$$\boldsymbol{s} = \begin{pmatrix} 0 \\ \sin i_* \\ \cos i_* \end{pmatrix}, \boldsymbol{l} = \begin{pmatrix} \sin i_{\mathrm{orb}} \sin\lambda \\ \sin i_{\mathrm{orb}} \cos\lambda \\ \cos i_{\mathrm{orb}}. \end{pmatrix} \tag{2.2}$$

The dot product of the two vectors

$$\cos\psi = \boldsymbol{s}\cdot\boldsymbol{l} = \sin i_* \sin i_{\mathrm{orb}} \cos\lambda + \cos i_* \cos i_{\mathrm{orb}}, \tag{2.3}$$

shows the relation between the spin-orbit angle, $\psi$, and three other parameters.

In the following subsections, we discuss about the current approaches to measure the projected spin-orbit angle $\lambda$, the stellar inclination angle, $i_*$ and the planetary orbital inclination angle, $i_{\mathrm{orb}}$ respectively.

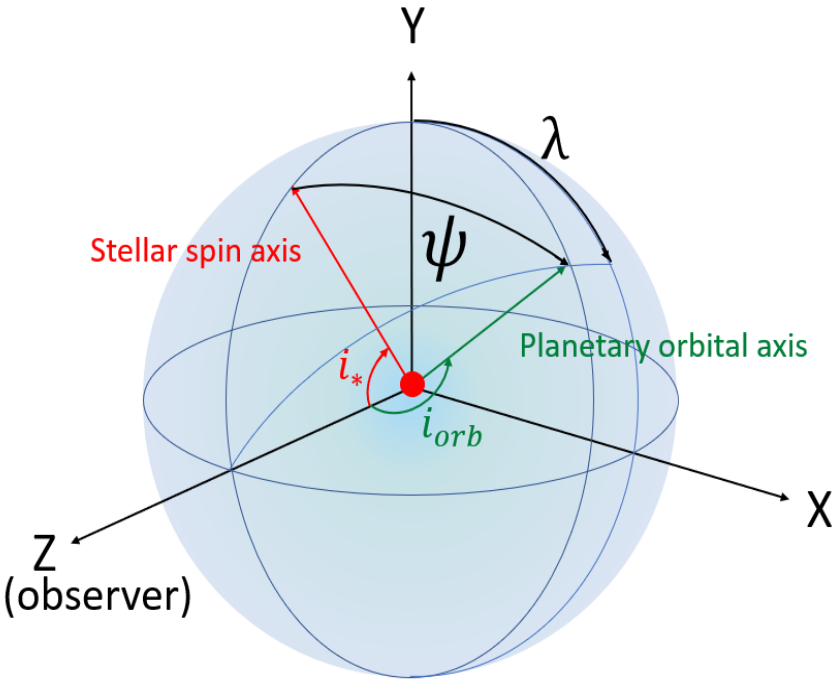

Figure 2.2: Schematic illustration of the geometry of star-planet system. The coordinate system is centered on the star with $+Z$ axis pointing towards observer and $+Y$ axis in the direction of sky projected stellar spin.The red dot represents the host star of the exoplanetary system. The red arrow is the stellar rotational spin and the green arrow is the planetary orbital axis.

### 2.2.1 The Projected Spin-orbit Angle $\lambda$

Before the launch of Kepler telescope, modeling the Rossiter-McLaughlin (RM) effect (Rossiter, 1924; McLaughlin, 1924) is the major technique to study the alignment between the stellar spin and the planetary orbital axis. This method estimates the projected spin-orbit angle $\lambda$. The Rossiter-McLaughlin (RM) effect describes a spectroscopic distortion when a planet transits its host star. As a star rotates, one of its hemisphere is blue-shifted and the other red-shifted in the light spectrum. The resulting spectral line is broadened symmetrically. If there is an orbiting planet, the star wobbles around their common center of mass. The movement causes a periodic shift of the entire spectral line, the rate of which corresponds to the radial velocity of the star.

If the orbiting planet happens to transit the star, it will then block part of the stellar flux as it moves across the apparent stellar disk. If the light from the red shifted region is blocked, the spectral line will further blue shifted and vice versa. Figure 2.3 illustrates the blocking of the blue and red shifted light respectively as a planet transits its host star. Such blocking of light causes an additional pseudo shift of the spectral line. This pseudo shift caused by the transit of a planet is called the the Rossiter-McLaughlin effect and it appears as a small anomaly on the radial velocity curve. Figure 2.4 shows the schematic illustration of the radial velocity curve when a planet transits its host star. The shape of anomalies induced by transits varies as the projected spin-orbit angles, $\lambda$.

By modeling the Rossiter-McLaughlin effect(see e.g. Ohta et al., 2005; Hirano et al., 2011; Boué et al., 2013), we can then estimate the projected spin-orbit angle $\lambda$. However, since the

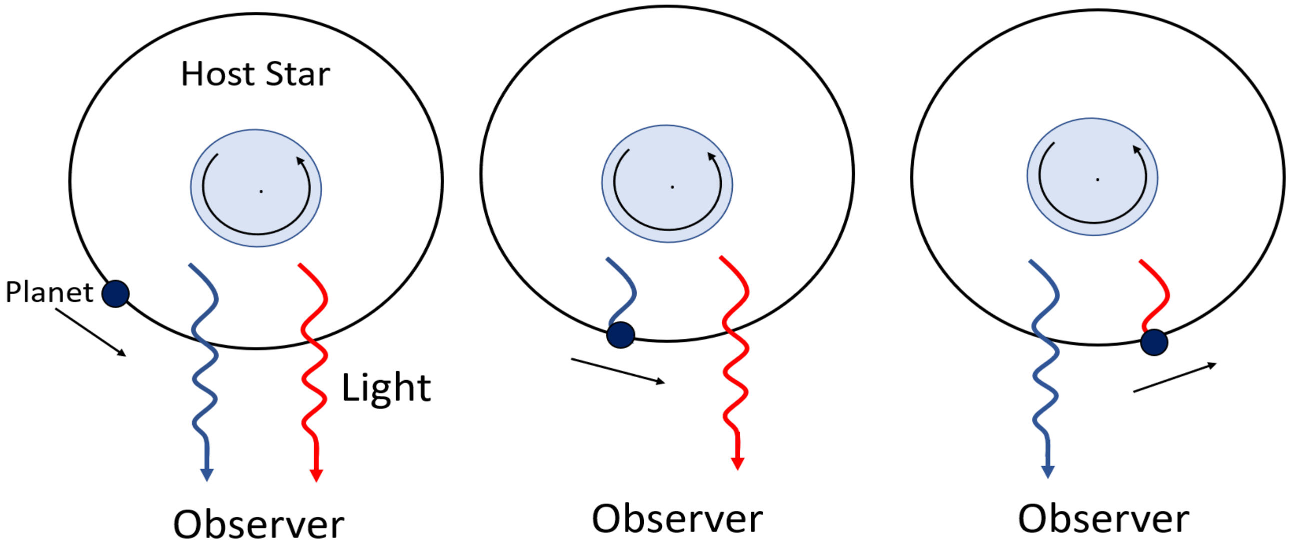

Figure 2.3: Pole on views of an exoplanetary system which illustrates of the configuration which causes the Rossiter-McLaughlin effect. The black circle is the orbit of a planet. In this plot, an aligned stellar rotation spin and planetary orbital axis is assumed. The stellar inclination relative to the line of sight is 90°. As the planet move in front of its host star with respect to the observer, it blocks a part of light from the star.

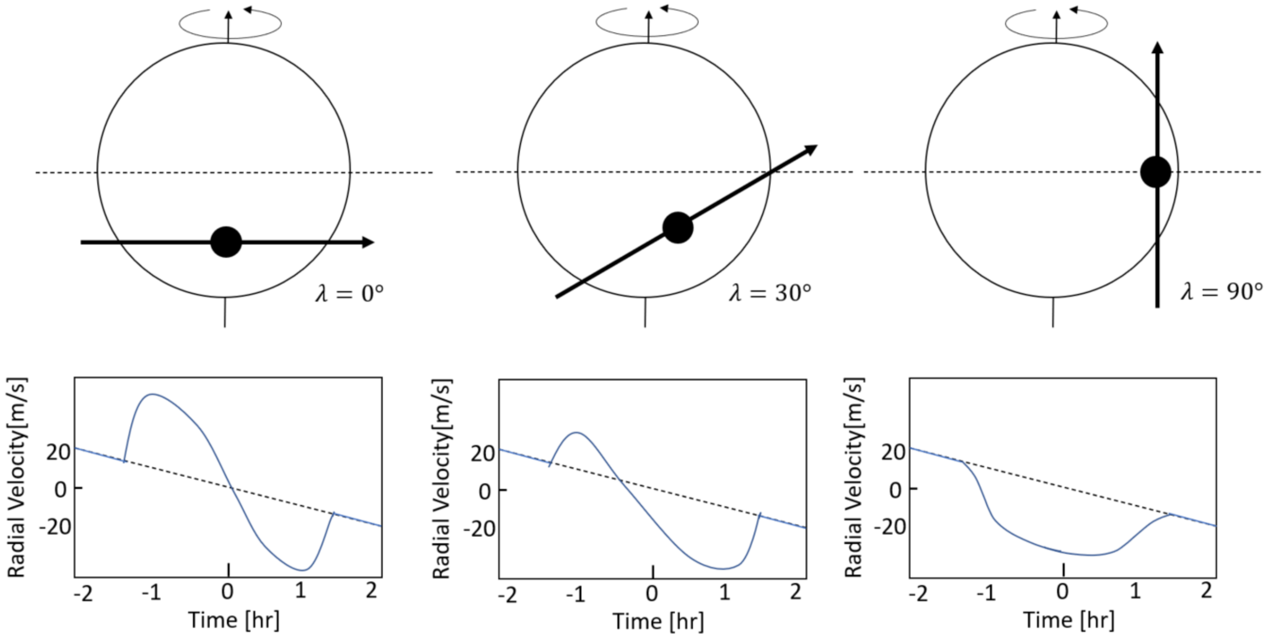

Figure 2.4: Schematic illustration of radial velocity anomaly due to the Rossiter-McLaughlin effect for different values of projected spin-orbit angle $\lambda$. $\lambda = 0°$ represents an aligned system. The blue curve is the radial velocity curve when the planet transits and the dotted line shows the curve when the planet does not. Figure adapted from Gaudi & Winn (2007).

Rossiter-McLaughlin effect is a mild phenomenon, the detection of it requires high resolution spectrograph. In addition, since the amplitude of the Rossiter-McLaughlin effect is positively correlated to the transit depth, this method prefers system with large planets and close in orbits. Consequently, most estimations of $\lambda$ are for hot Jupiter systems.

With the photometric data from Kepler, another way to constrain the projected spin orbit angle is proposed, which is the modeling of planet's transit across star spots. In the photometric data from Kepler, regular dips are observed for some stars. These dips are considered as the signatures of a planet as it moves across (transits) the apparent disk of its host star. When the planet happens to transit above a star spot (spot-crossing event), the integrated flux will slightly increase which cause a small anomaly in the transit dip. By modeling the transit dipping, the projected spin-orbit angle $\lambda$ can be obtained (see e.g. Sanchis-Ojeda et al., 2011). However, since this method only applies when successive spot crossing events are observed, it has a small applicable range.

### 2.2.2 The Stellar Inclination Angles $i_*$

With the launch of Kepler and TESS, photometric data with high precision becomes available for a large number of stars, which provides the opportunity for a better estimation of the stellar inclination angles. There are in general two methods to determine the inclination angle $i_*$. The first one is a composite method which requires both photometric and spectroscopic analysis of the star. The second one is the asteroseismic analysis which estimates $i_*$ by modeling the oscillation patterns of the pulsating stars.

#### Composite Method

The composite method requires three parameters, the stellar rotation period $P$, the projected stellar rotational velocity $v \sin i_*$ and the stellar radius $R_*$, from independent measurements. The derivation of $i_*$ is given by (see e.g. Winn et al., 2007; Hirano et al., 2014; Kovacs, Geza, 2018)

$$i_* = \sin^{-1}\left(\frac{v_* \sin i_*}{2\pi R_*/P_{\mathrm{rot}}}\right), \tag{2.4}$$

where $R_*$ is the stellar radius from the stellar evolution model, $P_{\mathrm{rot}}$ is the stellar rotation period from photometric analysis and $v_* \sin i_*$ is the projected rotational velocity from spectroscopic analysis. Photometric analysis of stellar rotation period $P$ studies the variation of light curve caused by active features on the stellar surface. As a star rotates, the active regions like star spots on its surface also rotate with it, causing a regular variation of flux with period associated to the stellar rotation period $P$. There are three major photometric methods which can extract the period of such variations, which are the Lomb-Scargle periodogram (e.g. Lomb, 1976; Scargle, 1982; Nielsen et al., 2013), the Auto-correlation function (e.g. McQuillan et al., 2013a) and the wavelet analysis (e.g. García et al., 2014). These methods have been applied to a large number of stars in the past literature. For example, McQuillan et al. (2014) measure stellar rotation period of 34,030 Kepler main-sequence stars using ACF method and Nielsen et al. (2013) apply LS method to 12,000 Kepler main-sequence stars. The estimation of $P_{\mathrm{rot}}$ using photometric methods is the main part of this thesis which will be discussed extensively in Chapter 3.

The projected stellar rotational velocity $v \sin i_*$ is determined from the rotational broadening of the spectral line. To extract the $v \sin i_*$ value, one approach is to study the Fourier transform of the observed spectrum(see e.g. Carroll, 1928, 1933). There will be consecutive zeros at frequencies inversely proportional to the rotational velocity $v \sin i_*$ in the Fourier spectrum. By measuring these frequencies, $v \sin i_*$ can be deduced. However, this method only works well for fast rotators (e.g. $v \sin i_* > 30kms^{-1}$) (Bouvier, 2013). Other more common approaches include the direct measurement of the line broadening, and the cross-correlation of the observed spectral line with a template spectrum from a model star with similar effective temperatures but no rotation. For the spectroscopic analysis, caution needs to be taken to discern the rotational broadening from other contributions like the velocity field of granules.

This composite method has a large applicable range. However, since this method includes inputs from three independent approaches, the uncertainty for measured $i_*$ could be large.

### Asteroseismology

The second method to measure stellar inclination angle is asteroseismic analysis, which is believed to give a potentially more precise estimation. Asteroseismology studies the oscillations of pulsating stars which are caused by the interplay between gravity and pressure within the stars. It is a powerful tool to probe the inner part of stars, which first proves itself in its application to the Sun (Helioseismology). The first observation of solar oscillations is made by Leighton et al. (1962) which was later identified as trapped standing acoustic waves by Ulrich (1970). By studying these pulsations, one gets to know properties of the Sun like its density profile (e.g. Basu et al., 2009) and rotation profile (Thompson et al., 1996). With the launch of space telescopes like CoRoT and Kepler, a large amount of high quality photometric data become available for asteroseismic study (see e.g. Huber et al., 2011; Chaplin et al., 2011).

The pulsations of stars cause regular variation of flux in time series, which appears in the power spectrum as regular patterns of modes (peaks). The power spectrum of oscillations is approximated as (see e.g. Anderson et al., 1990; Gizon & Solanki, 2003)

$$P(\nu) = \sum_{n=n_{\min}}^{n_{\max}} \sum_{l=0}^{l_{\max}} \sum_{m=-l}^{+l} \frac{H(n,l,m,i_*)}{1 + 4[\nu - \nu(n,l,m)]^2/\Gamma^2(n,l,m)} + N(\nu), \tag{2.5}$$

where $N(\nu)$ is a background noise. $\Gamma(n,l,m)$ is the width of the each mode and $\nu(n,l,m)$ is the central frequency of mode. Since solar type stars have mild rotation, it is reasonable to assume that they are spherically symmetric. Hence, the stellar pulsation can be described by spherical harmonics which are characterized by radial order $n$, angular order $l$, and azimuthal order $m$.

The rotation of stars plays a part in splitting each degenerate mode(peak) centered at $\nu(n,l,m)$ into $2l+1$ equally spaced m modes, which can be approximated as

$$\nu(n,l,m) = \nu(n,l) + m\delta\nu \tag{2.6}$$

The $\delta\nu_*$ is the splitting between successive $m$ modes. The inverse of $\delta\nu_*$ is the stellar rotation period $P$ averaged over regions on stellar surface defined by modes$(n,l,m)$ fitted.

$H(n,l,m,i_*)$ is the mode height described by $H(n,l,m,i_*) = \mathscr{E}(l,m,i_*)H(n,l)$ (Gizon & Solanki, 2003), with

$$\mathscr{E}(l,m,i_*) = \frac{(l-|m|)!}{(l+|m|)!} \left[P_l^{|m|}(\cos i_*)\right]^2, \tag{2.7}$$

where $i_*$ is the inclination angle of star. The information of stellar inclination is contained in the height ratio of different $m$ peaks splitted from an angular l *mode*.

By fitting the observed power spectrum with this model, we can extract both the stellar inclination $i_*$ and the stellar rotation period $P$ of stars (e.g. Benomar et al., 2009; Kamiaka et al., 2018).

Asteroseismic analysis has an advantage that its measurements of stellar inclination angle and rotation period are less affected by the complex configuration on the stellar surface. However, this technique has a very strict requirement on the signal to noise ratio of the time series. The current available asteroseismic analysis for solar type stars is only around tens to hundreds.

In addition, asteroseismic analysis behaves poorly for stars with stellar inclination angle larger than 80° or smaller than 20° Kamiaka et al. (2018) as well as for slow rotators even with high signal to noise ratio. There is also a correlation between the stellar inclination and stellar rotation period in the fitting of asteroseismic model. Hence, in the region where either $i_*$ or $P$ can not be properly measured, the other parameter is also biased (e.g. Ballot et al., 2006; Ballot et al., 2008; Kamiaka et al., 2018). A possible solution is to provide a prior knowledge of stellar rotation period to the fitting of model. The rotation period obtained from photometric analyses is potentially a good candidate. In this thesis, we will discuss about this possibility in the last part of Chapter 3, after we examine the three widely used photometric methods.

### 2.2.3 The planetary orbital inclination $i_{\rm orb}$

Despite that $i_{\rm orb} \approx 90°$ is a good approximation for transiting stars, a more accurate estimation of $i_{\rm orb}$ can be obtained by modeling the transiting dip in the light curve. Our introduction to the estimation of the planetary orbital inclination $i_{\rm orb}$ follows Winn (2010).

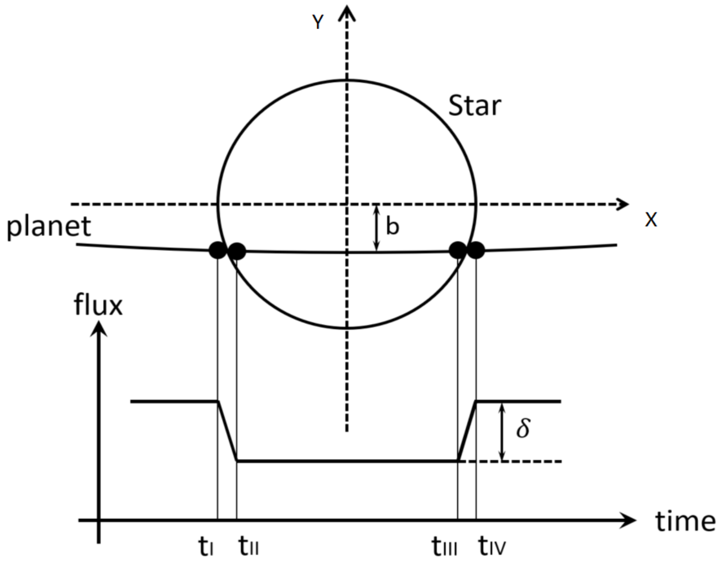

Figure 2.5: Schematic illustration of planetary transit with impact parameter b. Transit of planet causes a dipping with flux variation $\delta$. Figure adapted from Winn (2010).

Transit is the eclipse of part of the star by an orbiting planet. It usually refers to non-grazing eclipse where the full disk of planet passes within that of star. Figure 2.5 illustrates the transit in a reference frame with Z-axis pointing towards the observer, projected sky in X-Y plane and X = 0 at the center of conjunction. During the ingress and egress of the planet, there are four contact points at which planetary disk is tangent to stellar disk, $t_{\rm I} - t_{\rm IV}$. Total duration $T_{\rm tot}$ and full duration $T_{\rm full}$ of transit are approximated as

$$T_{\rm tot} \equiv t_{\rm IV} - t_{\rm I} = \frac{P}{\pi} \sin^{-1}\left[\frac{R_*}{a}\frac{\sqrt{(1+k)^2 - b^2}}{\sin i_{\rm orb}}\right]\left(\frac{\sqrt{1-e^2}}{1+e\sin\omega}\right), \tag{2.8}$$

$$T_{\rm full} \equiv t_{\rm III} - t_{\rm II} = \frac{P}{\pi} \sin^{-1}\left[\frac{R_*}{a}\frac{\sqrt{(1-k)^2 - b^2}}{\sin i_{\rm orb}}\right]\left(\frac{\sqrt{1-e^2}}{1+e\sin\omega}\right), \tag{2.9}$$

where $k = R_p/R_*$ is the ratio between the radius of planet, $R_p$, and that of the star, $R_*$, $a$ is the semi-major axis, $\omega$ is the argument of pericentre, $P$ is the orbital period, and $b$ is the impact parameter, which is defined as the sky-projected distance at X = 0:

$$b = \frac{a\cos i_{\rm orb}}{R_*}\left(\frac{1-e^2}{1+e\sin\omega}\right) \tag{2.10}$$

The orbital inclination $i_{\rm orb}$ may be obtained by fitting the transiting light curve with the model given by equation (2.8), (2.9) and (2.10)

## 2.3 Constraints on Spin-orbit Angle From Stellar Inclination

With the high quality photometric data from space mission like Kepler and TESS, we are now ready to collect more information about spin-orbit angle from the side of stellar inclination angle $i_*$. Hirano et al. (2012) applied the combined analysis of photometric and spectroscopic measurements (see Section 2.2.2) to obtain the stellar inclination $i_*$ for 15 exoplanetary systems with detected planets. They report a possible misaligned system KOI-261. Hirano et al. (2014) used the same technique on 25 systems and detected three possible misaligned multi-planet systems (KOI-304, 988, 2261). Based on the same method, Winn et al. (2017) measured $i_*$ for 156 planets and discovered three systems with possible large spin-orbit angles.

Huber et al. (2013) used asteroseismic analysis to measure the stellar inclination angle $i_*$ and detected a misaligned system, Kepler-56, with $i = 43^\circ \pm 4^\circ$. Kamiaka et al. (2019) discovered a system, Kepler-408, with high obliquity of $i_* = 42^{+5}_{-4}$ through asteroseismic analysis. So far, Kepler-408b is the smallest planet (Earth-sized) discovered to have large spin-orbit misalignment. These results of stellar inclination angle $i_*$ suggest that the spin-orbit misalignment is not confined to hot Jupiter systems.

Now that stellar inclination angle $i_*$ could potentially become the major approach to constrain the spin-orbit angle $\psi$, the accuracy of measured $i_*$ needs to be studied as well as improved. Our study of photometric analysis contributes to this purpose. In Chapter 3 of this thesis, we examine the three widely used photometric methods to determine the stellar rotation period on 91 solar-type stars. We aim to understand the reliability of photometric methods and the suitability of using the photometric periods as priors for asteroseismic analysis. In Chapter 4, we discuss about the bias found in asteroseismic estimation of stellar inclination angle $i_*$ and introduce some ongoing attempts to reduce the bias.

Last but not least, thanks to the great effort of various groups working on the determination of the 3D spin-orbit angle $\psi$, there are so far estimates of $\psi$ for 20 exoplanetary systems. We summarize these systems in table 2.1.

| System | $\psi(deg)$ | Reference | Method |
|---|---|---|---|
| HAT-P-36 | $0.00^{+63.00}_{-0.00}$ | Mancini et al. (2015) | the RM effect/Composite method |
| Kepler-17 | $0.00^{+15.00}_{-15.00}$ | Désert et al. (2011) | Spot crossing/Composite method |
| WASP-43 | $0.00^{+20.00}_{-0.00}$ | Esposito et al. (2017) | the RM effect/Composite method |
| HD 189733 | $7.00^{+12.00}_{-4.00}$ | Cegla et al. (2016) | the RM effect/Transit modeling |
| WASP-84 | $17.30^{+7.70}_{-7.70}$ | Anderson et al. (2015) | the RM effect/Composite method |
| CoRoT-18 | $20.00^{+20.00}_{-20.00}$ | Hébrard et al. (2011) | the RM effect/Composite method |
| HAT-P-22 | $24.00^{+18.00}_{-18.00}$ | Mancini, L. et al. (2018) | the RM effect/Composite method |
| Kepler-25c | $26.90^{+7.00}_{-9.20}$ | Benomar et al. (2014) | the RM effect/Asteroseismology |
| XO-2 | $27.00^{+12.00}_{-27.00}$ | Damasso et al. (2015) | the RM effect/Composite method |
| HAT-P-20 | $36.00^{+10.00}_{-12.00}$ | Esposito et al. (2017) | the RM effect/Composite method |
| Kepler-13 | $60.25^{+0.05}_{-0.05}$ | Howarth & Morello (2017) | Gravity darkening |
| WASP-117 | $69.50^{+3.60}_{-3.10}$ | Lendl et al. (2014) | the RM effect/Composite method |
| GJ 436 | $80.00^{+21.00}_{-18.00}$ | Bourrier et al. (2018) | the RM effect/Composite method |
| WASP-121 | $88.10^{+0.25}_{-0.25}$ | Bourrier, V. et al. (2020) | the RM effect/Composite method |
| WASP-107 | $90.00^{+50.00}_{-50.00}$ | Dai & Winn (2017) | Spot crossing/Composite method |
| WASP-189 | $90.00^{+5.89}_{-5.80}$ | Anderson et al. (2018) | the RM effect/Composite method |
| MASCARA-4 | $104.00^{+7.00}_{-13.00}$ | Ahlers et al. (2020) | Gravity darkening |
| HAT-P-7 | $115.00^{+19.00}_{-16.00}$ | Benomar et al. (2014) | the RM effect/Asteroseismology |
| KELT-17 | $116.00^{+4.00}_{-4.00}$ | Zhou et al. (2016) | Doppler tomography |
| Kepler-63 | $145.00^{+9.00}_{-14.00}$ | Sanchis-Ojeda et al. (2013) | the RM effect/Spot crossing |

Table 2.1: Summary of exoplanetary systems with spin-orbit angle $\psi$ measured.

# Chapter 3

# Stellar Rotation Period

## 3.1 Introduction

In this chapter, we examined the reliability of three photometric methods (LS periodogram, ACF, and wavelet analysis) in determining the stellar rotation periods on 91 Kepler solar-type stars. Photometric analysis measures the rotation period by studying the variation of light curve caused by active features on the stellar surface. Before jumping into the detail of data analysis, we would like to briefly introduce the surface rotation profile of solar-type stars, focusing on our Sun as a well studied example, and discuss about the behavior of active features (star spots) on the stellar surface.

Solar-type stars are similar to the Sun in their effective temperatures. The rotation periods of these stars usually lie within 1 to 50 days. The well studied solar-type star, the Sun, shows a non-uniform surface rotation with the fastest rotation rate near the equator ($P \approx 25\,\mathrm{days}$) and a gradual decrease in rate towards the pole ($P \approx 35\,\mathrm{days}$). Its surface rotation rate is later generalized as (Howard & Harvey, 1970)

$$\frac{\Omega(\theta)}{2\pi} = A + B\sin^2\theta + C\sin^4\theta, \tag{3.1}$$

where $\theta$ refers to the latitude, A is the rotation rate at the equator, while B and C describe the decrease of rotation rate along the latitude. Differential rotations are also observed in other solar-type stars (see e.g. Benomar et al., 2018). In some extreme cases, the rotational rates around the equator are more than twice of those near the mid-latitudes. Due to the differential rotation on the stellar surface, we might detect multiple periodic signals for a single star, depending on the number of active regions and their latitudes on the stellar surface.

The most common active feature on the stellar surface is the star spot. Star spots (Figure 3.1) are dark regions on the stellar surface. In these regions, the concentrated magnetic field flux limits the heat transport by convection, which in turn causes a decrease in temperature.

A star spot is composed of a central region called umbra and a peripheral region called penumbra. The temperature decrease in umbra is larger than that in penumbra. In the case of the Sun, the temperature decrease, $\Delta T$, in umbra is around 1700 K, while that in penumbra is around 700 K. Current observations suggest that the temperature difference between spotted

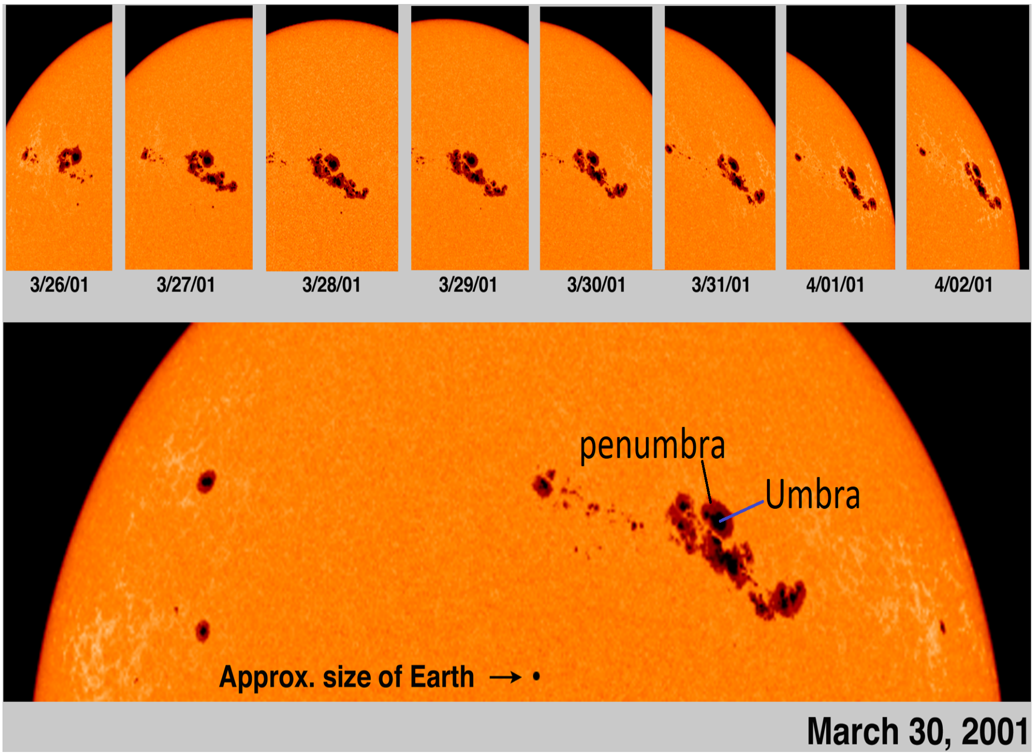

Figure 3.1: Figure of sunspots on solar surface. The upper panel shows a series of shots for one spotted region as it rotates with the Sun. The bottom panel shows a enlarged version of the region. The darkest part in the center of spot is the umbra and the slightly brighter region in peripheral is the penumbra. Credit to NASA/SOHO `https://sohowww.nascom.nasa.gov/home.html`.

regions and photosphere ranges from around 200 to 2000 K for M-G stars. In addition, this difference increases with temperature (Berdyugina, 2005). This trend could indicate that for stars like M dwarfs, the size of spots is relatively small. For small spots, the penumbra dominates so that the temperature decrease in this region is relatively small.

The size of spotted regions on the Sun ranges from around 16 to 160.000 km while for other observed stars, the spot coverage is in general much larger. An extreme example could be HD 12545 which is an active K0 giant with spotted regions covering around 40% of the apparent stellar disk (Strassmeier, 1999). Hall & Henry (1994) suggested that, for relatively small spots like those on the Sun, their lifetimes are proportional of to their size. For large spots, the shear of latitudinal differential rotation could be the key factor which determines how long they live (Berdyugina, 2005). Small spots usually last for days to months while large spots could last for years.

During their lifetimes, spots move either towards the equator (e.g.the Sun) or towards the pole (e.g.HR 1099, Vogt et al., 1999; Strassmeier & Bartus, 2000) with a time scale of years. Furthermore, the place where spotted areas emerge also migrates. The famous butterfly diagram for sunspots illustrates the migration of spotted areas within a 11-year activity cycle (Figure 3.2). At the beginning of a cycle, sun spots normally form near the intermediate latitude while at the end of a cycle, they merge around the equatorial region.

Usually there are multiple spotted regions evolving and migrating on the stellar surface, which lead to complex configurations on the stellar surface. One of the interesting patterns observed

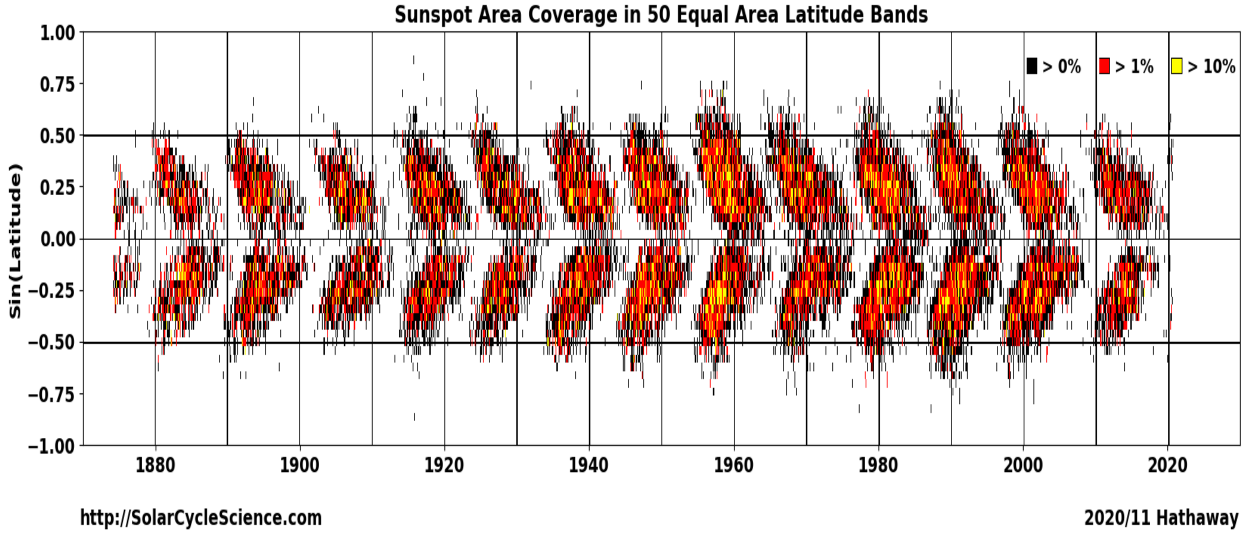

Figure 3.2: Butterfly diagram of the Sunspot. Y-axis is the latitude. X-axis is the Date. This plot illustrates the change of spot distribution over the 11-year solar cycle. The color mark indicates the % of band area covered by spots. Credit to Hathaway at NASA Marshall Space Flight Center `http://SolarCycleScience.com`.

for sunspots is the existence of two active longitudes separated by 180°. Between these two regions, there is a periodic exchange of activity strength, which is named the flip-flop cycle.

The complex configuration of star spots on the stellar surface have pros and cons. If the spotted regions locate at different latitude, we are likely to detect multiple periodic signals, each corresponding to the an actual rotation period at a certain latitude of the stellar surface. We could utilize this information to obtain an averaged surface rotation which is best suited for a combined analysis with spectroscopy and asteroseismology. On the other hand, when the active regions distributed with equal spacing in longitude like the flip-flop case, we are likely to detect a significant peak (aliases) at period $P/n$ in the power spectrum of photometric analysis, depending on the number $n$ of active regions. This brings us a risk to underestimate the rotation period by an integer factor of $n$.

With the advent of Kepler space telescope, photometric data of more than 100,000 stars in the field of Cygnus and Lyra constellations (Figure 3.3) become available, which benefits the photometric analysis of stellar rotation period to a large extent. Kepler contains a Schmidt camera whose focal plane is made out of 42 CCDs ($50 \times 25\,$mm), possessing a total resolution of 94.6 megapixels. There are two types of time series data which Kepler provides: One is the short-cadence data with 58.89 seconds-interval, and the other is the long-cadence data with 29.4 minutes-interval. The long-cadence data usually lasts around 4 years which is much longer than the typical rotation period of solar type stars ($\sim 1-50\,$days), and hence is ideal for photometric analysis.

There are three widely used methods for photometric analysis which are Lomb-Scargle Periodogram (LS periodogram, Lomb, 1976; Scargle, 1982), Auto-correlation Function (ACF), and wavelet analysis (e.g. a good practical guide, Torrence & Compo, 1998). Examples of applications include Nielsen et al. (2013) in which LS periodogram has been applied to infer the stellar rotation period for 12,000 main-sequence Kepler stars, McQuillan et al. (2014) in which ACF has been used to estimate the rotation period for 34,030 main-sequence Kepler stars, and

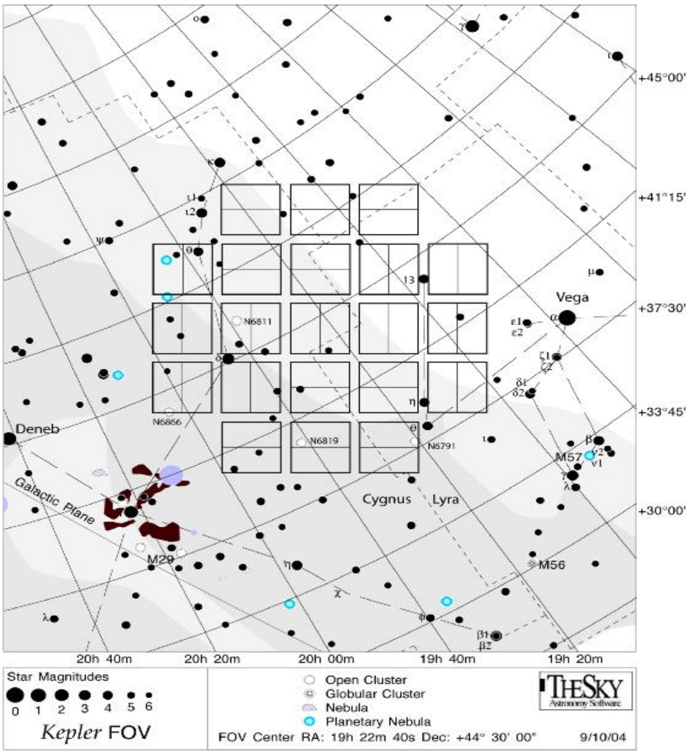
+45°00'
+41°15'
+37°30'
+33°45'
+30°00'
Vega
Deneb
Galactic Plane
Cygnus
Lyra
M57
M56
M29
N6811
N6866
N6819
N6791
20h 40m
20h 20m
20h 00m
19h 40m
19h 20m
Star Magnitudes
0 1 2 3 4 5 6
Kepler FOV
Open Cluster
Globular Cluster
Nebula
Planetary Nebula
THESKY Astronomy Software
FOV Center RA: 19h 22m 40s Dec: +44° 30' 00"
9/10/04

Figure 3.3: A depiction of Kepler's field of view. Each square represents the view of a CCD module composed of 2 CCDs. Credit to NASA `www.nasa.gov/mission_pages/kepler/multimedia/images/fov-kepler-drawing.html`.

García et al. (2014) in which both Wavelet analysis and ACF have been utilized to obtain the rotation period for 310 solar-type Kepler stars.

Due to the likely differential rotation on the stellar surface, the rotation periods at different latitudes could vary. Photometric analysis measures the rotation period at the latitude where active features show asymmetric distribution. Since the Kepler telescope has a limited spatial resolution, it does not provide the information on the latitude of active features. As a result, the rotation period detected by the photometric analysis refers to a period within the range of differential rotation on the stellar surface. This nature of photometric analysis leads to possible discrepancy of measurement from spectroscopic and asteroseismic analysis which estimate an averaged surface rotation period. For the Sun, such discrepancy stays within $\sim 40\%$. Hence, the similar situation is expected for most of the other solar-type stars.

In the following sections, we examine these three photometric methods on 91 solar-type stars and discuss about the suitability of using photometric period as a prior for asteroseismic inference of stellar inclination angle $i_*$.

## 3.2 Target Selection

We first adopted the same group of targets as Kamiaka et al. (2018) (see Figure 3.4), which include 94 solar-type Kepler stars. This group contains the entire LEGACY sample (Lund et al., 2017) which are 66 Kepler solar-like stars with clear pulsation patterns. The LEGACY sample are chosen from 500 Kepler main-sequences and sub-giant candidates with observed stellar oscillations (Chaplin et al., 2011). The selection criteria is based on the data quality for conducting reliable asteroseismic analysis (Aguirre et al., 2017; Lund et al., 2017). Since the LEGACY sample contains only 5 stars with reported planet candidates (Kepler object of interest, KOI stars), Kamiaka et al. (2018) included additional 28 solar-type stars with planet detections and observable oscillation patterns for comparison purpose. We performed a preliminary check for light curves of these 94 stars and removed 3 targets with either reported contamination from other light source or significant missing of long-cadence data.

As a result, our final sample contains 91 solar-type Kepler stars,with 60 stars having no planet detection and 31 KOI stars.

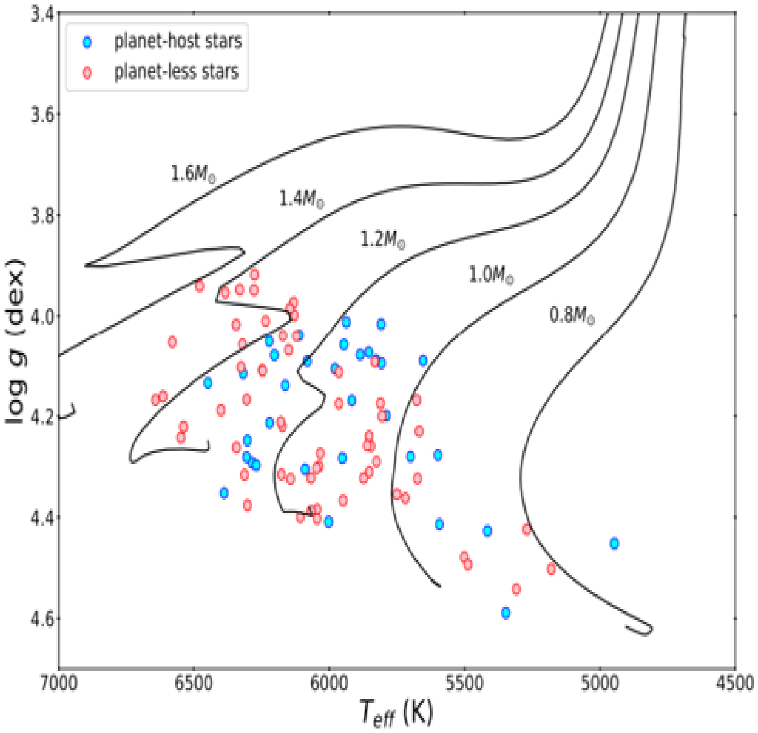

Figure 3.4: HR diagram in the form of surface gravity vs effective temperature. The 94 solar-type stars in the sample of Kamiaka et al. (2018) is plotted. The blue circles represent the planet host stars (KOI stars) and the red circle represent the planet less stars. Plot adopted from the doctoral thesis of Shoya Kamiaka.

## 3.3 Preparation of Light Curves

In this subsection, we discuss about the preparation of light curve for later photometric analysis. The CCDs on Kepler telescope provide pixel data every few seconds (∼ 6.5 seconds). A standard pixel mask (aperture) is assigned to each target, which determines the pixels that is related to this target. These pixels are then summed over a fixed time duration (cadence) to create the 1-D light curve of this target. Kepler provides both the short-cadence data which is summed over every 58.89 seconds and the long cadence data which is summed over each 29.4 minutes. Since Kepler adjusts its orientation every 90 days to keep the solar panel in the direction of the

Sun, the Kepler data is further divided into quarters with 90-day duration,except for quarter 0 (Q0) with 10-day duration and quarter 1 (Q1) with 34-day duration.

The Kepler science team provides two type of light curve. The SAP light curve is the raw light curve obtained from background corrected pixels. The PDC light curve undergoes further preliminary correction to remove signatures of instrumental perturbations like pointing drift. We used the PDC light curve (PDC-msMAP, see Stumpe et al., 2014) for analysis.

To start with, we downloaded quarter-2 to quarter-14 of the Kepler long-cadence PDC light curve (Data Release 25) from Mikulski Archive for Space Telescope (MAST), upon availability. For some of our targets, there is missing of several quarters. To remove any remaining systematic trends in the time series $y(t)_{initial}$ of each quarter, we first fitted a 4-th order polynomial $p(t)$ to the data. Then we normalized the light curve with the fitted polynomials as $y(t) = y(t)_{initial}/p(t) - 1$. Then, we concatenated all quarters into a single array of time series while preserving gaps between quarters. The starting time of this series is set to be 0. Figure 3.5 gives an example of normalized and concatenated light curve.

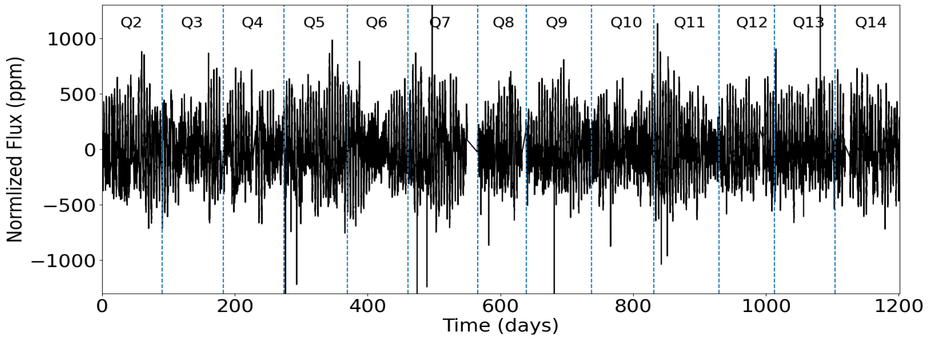

Figure 3.5: Normalized Q2-Q14 light curve from KIC 7206837, which is one of our target with no reported planet detection. The normalized flux is in the unit of parts per million (ppm). The black dotted lines mark the boundary between quarters.

In the light curve of some targets, we find abrupt increases in flux variation in some quarters. Such increases are limited to single quarters with no sign of gradual emergence and decay nearby (e.g. Figure3.6). We suspect that these variations might be due to unknown contamination or instrumental perturbation. Hence, we compute the median absolute magnitude of flux for each quarter. If the median value of a quarter is more than three times larger than the median values of its nearby quarters, we removed that quarter from the light curve. Such quarters are found in KIC 4141376, 6521045, 9955598, 11904151, 8694723 and 10730618.

Next, we removed signatures of planets. As a planet transits its host star, it causes regular dips in the light curve (see the upper panel of Figure 3.7). To mitigate the influence of these regular modulations, we fold the light curve using the orbital period of each planet candidate and removed the part of transit dip. In addition, when a planet moves to the back of its host star, the reflected light of the planet is blocked. Such secondary eclipse induces eclipse dips in the light curve, at a phase lag of 0.5 relative to the transit dips (see the bottom panel of Figure 3.7). Despite that the eclipse dips are minor effects which are visible in only a few of our targets, we removed the eclipse dip for all of our targets as a precautionary measure. The typical time scale of transit and eclipse duration is hours, while the time scale of planetary

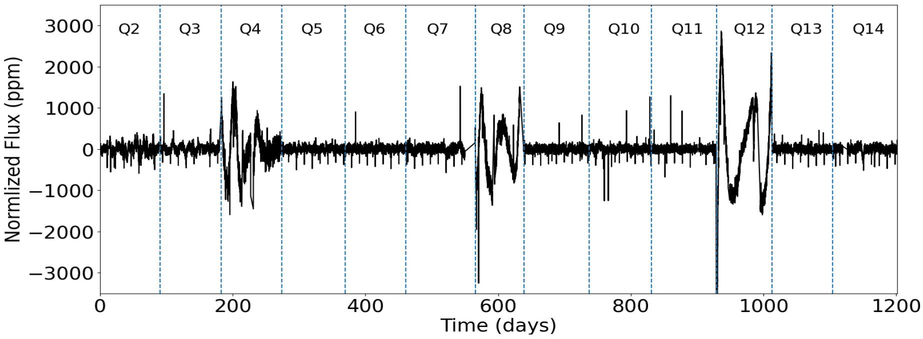

Figure 3.6: An example of light curve with sudden increase in flux variation within single quarters. Normalized Q2-Q14 light curve from KIC 4141376. Q4, Q8, and Q12 shows the sudden increase in flux variation. The variations only retain within these quarters themselves with no gradual transition from nearby quarters. We remove these quarters from the light curve.

orbital period is days. Therefore, the removed intervals are small enough not to influence the determination of stellar rotation period.

For practical reason, we only removed transit and eclipse dip caused by planets with orbital period smaller than 100 days. We failed to locate the transit dip for two planets by phase folding, which are KOI 5.02 orbiting around KIC 8554498 and Kepler-37 b around KIC 8478994. However, as the magnitudes of these transit dips are smaller than 20 ppm, they have negligible influence on the determination of stellar rotation period (Barclay et al., 2013; Burke et al., 2014).

Then, we removed outliers which are data points being $5\sigma$ away from the median of the light curve. As each quarter of light curve is of 90-day duration, any signal with longer period would be unreliable. We suppressed long-period signals by high-pass filtering the light curve with a box-car function of a 50-day width. Since Kepler data is nearly evenly sampled, we mapped the light curve to a uniformly sampled grid with interval of $\delta t = 29.4$ minutes. Finally, we padded the light curve. We attempted two padding schemes which are Gaussian noise padding and zero padding. For the Gaussian noise padding, $\mathcal{N}(0,\, \sigma^2_{noise})$, we define $\sigma_{noise}$ as $1\sigma$ deviation from the median of the flux value in the light curve.

By comparing the power spectra that we used to determine the stellar rotation, we noted that two padding schemes shows negligible difference in the determination of stellar rotation period. Figure 3.8 shows the power spectra (LS periodogram) of two targets computed using zero-padded and noise-padded light curves respectively. In each subplot, the upper panel is the padded light curve and the lower panel is the power spectrum computed from the light curve. We present two targets with relative large gaps in their light curve. As we can see, the power spectra of differently padded light curve looks very similar. In the case of KIC 10963065, the choice padding scheme does not affect the measurement of stellar rotation period. For 4141376, however, since there are two peaks with similar height in each power spectrum, the tiny difference in relative peak height leads to different choice of the highest peak, and hence stellar rotation period. The extreme case as KIC 4141376 is found in only two of our targets (KIC 4141376 and 9812850). Hence, the padding scheme does not affect the estimation of period significantly. We therefore only discuss the results from the noise-padded light curve in

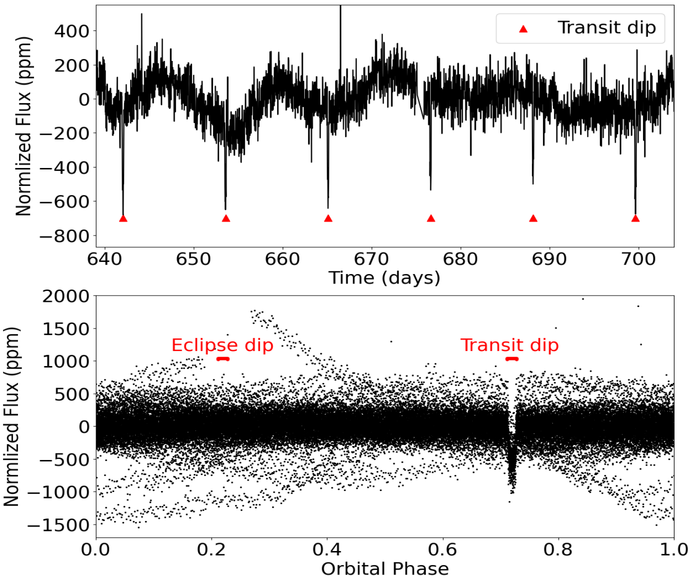

Figure 3.7: A section of normalized light curve from KIC 8349582 (top panel) and phase folded light curve at the planetary orbital period $P_{orb}$ from KIC 8349582 (bottom panel). The red triangles point at the transit dips in the light curve. In the phase folded light curve, the red bars mark the regions of transit dips and possible eclipse dips. We removed these regions from the light curve.

the following sections.

The entire procedure for preparation of light curve in summarized in a flow diagram in Figure 3.9.

## 3.4 Method

In this section, we introduce the three photometric methods we applied to extract the stellar rotation period, which are the Lomb-Scargle periodogram, the auto-correlation function and the wavelet analysis.

### 3.4.1 The Lomb-Scargle Periodogram

The Lomb-Scargle periodogram Lomb (1976); Scargle (1982) is the least-square-based estimator of the power spectrum. The model is a sinusoidal function

$$y(t) = a \cos \omega t + b \sin \omega t, \tag{3.2}$$

with candidate frequency $\omega$. We adopt a slightly modified model which adds an additional offset term c to $y(t)$ introduced by Zechmeister & Kürster (2009). This modified model is

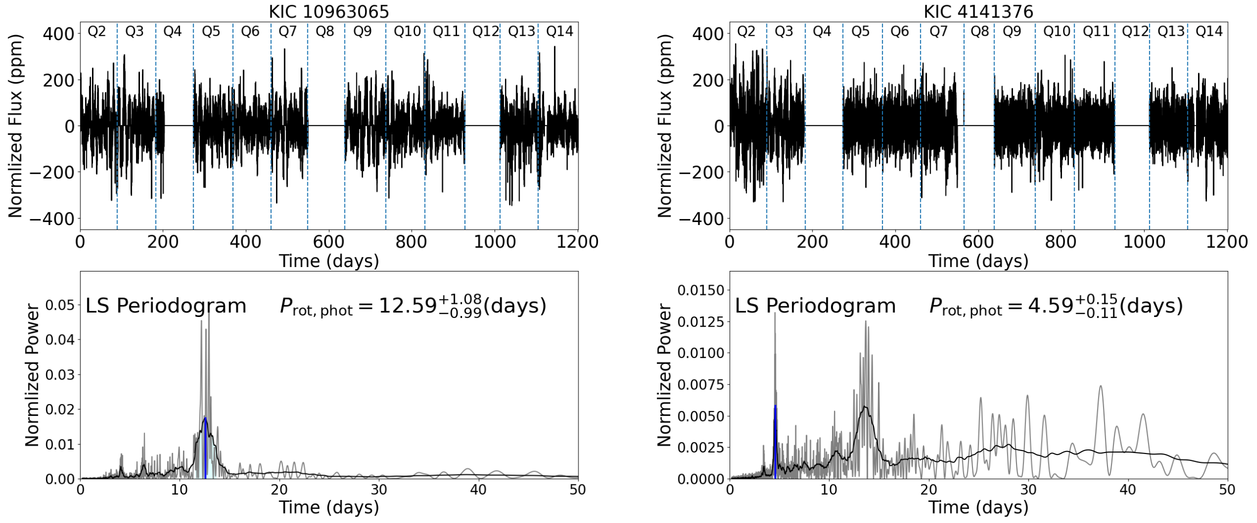

(a) KIC 10963065 with zero-padded light curve. (b) KIC 4141376 with zero-padded light curve.

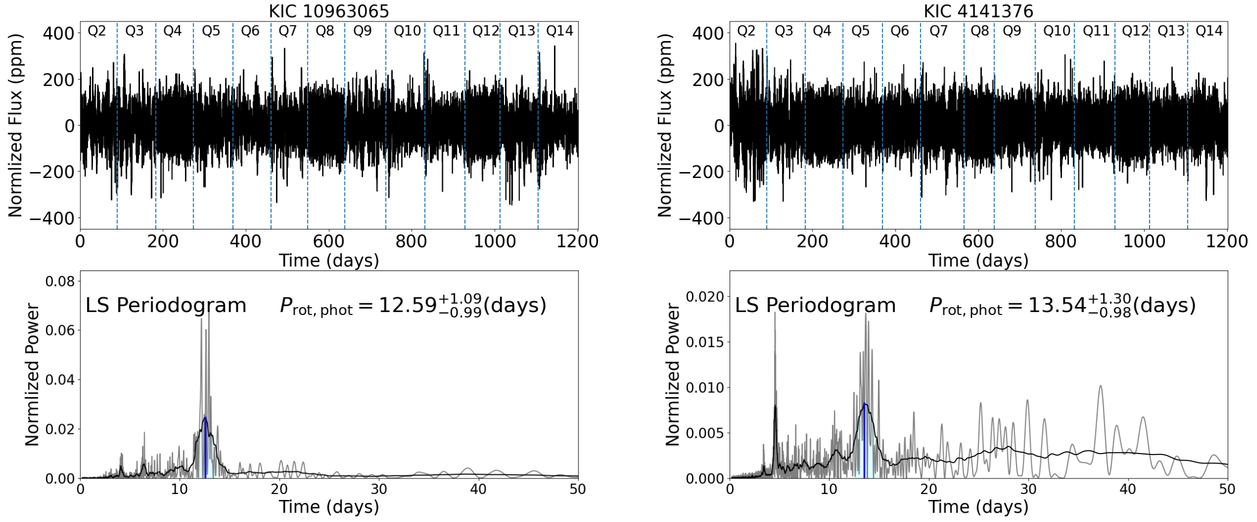

(c) KIC 10963065 with noise-padded light curve. (d) KIC 4141376 with noise-padded light curve.

Figure 3.8: Examples of power spectra computed using differently padded light curve for KIC 10963065 (subplot (a) and (c))and KIC 4141376 (subplot (b) and (d)). The upper panel of each subplot shows the padded light curve and the bottom panel shows the power spectrum (LS periodogram) computed from the light curve. LS periodogram is one of the methods we applied to extract rotation period which will be introduced in the following section. Power spectra of differently padded light curve show high resemblance. KIC 4141376 represents an extreme case found in only 2 of our targets, where the highest peak (choice of rotation period) in the power spectra differs for differently padded light curve. 89 out of 91 targets shows consistent estimations of period within the error using different padding schemes as KIC 10963065.

named generalized Lomb-Scargle periodogram. We normalize the periodogram to unity so that

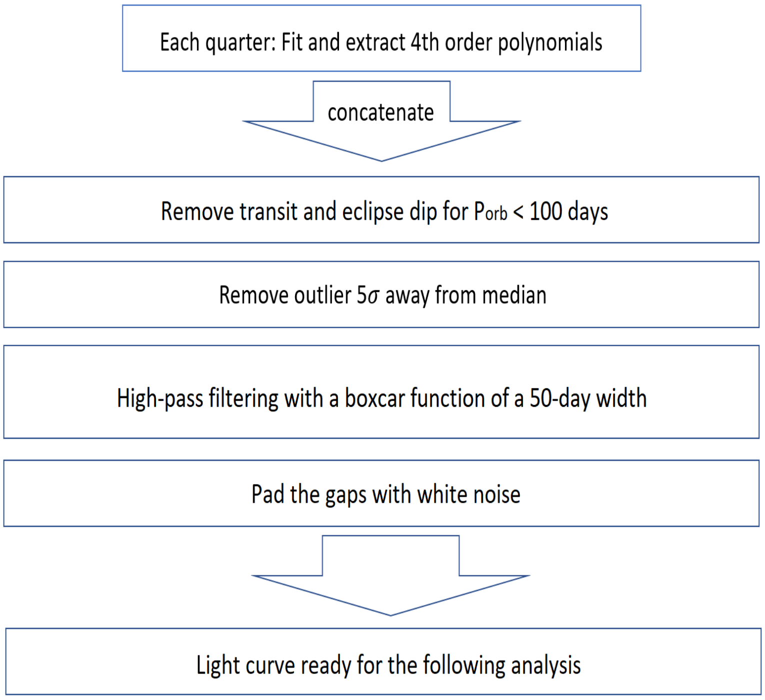
Each quarter: Fit and extract 4th order polynomials
concatenate
Remove transit and eclipse dip for Porb < 100 days
Remove outlier 5σ away from median
High-pass filtering with a boxcar function of a 50-day width
Pad the gaps with white noise
Light curve ready for the following analysis

Figure 3.9: Flow diagram of light curve preparation.

the power P($\omega$) will lie within the range [0,1]. The normalized periodogram takes the form

$$P(\omega) = \frac{\chi_0^2 - \chi^2(\omega)}{\chi_0^2}, \tag{3.3}$$

where $\chi(\omega)^2$ is the minimized squared difference between the time series $y_i$ and the sinusoidal model $y(t_i)$ for each frequency $\omega$ as

$$\chi(\omega)^2 = \sum_{i=1}^{N} \left[y_i - y(t_i)\right]^2, \tag{3.4}$$

and $\chi_0^2$ is a non-varying reference model given by

$$\chi_0^2 = \sum_{i=1}^{N} y_i^2. \tag{3.5}$$

For evenly sampled time series, the Lomb-Scargle periodogram can be reduced to the classical periodogram which is described by

$$\begin{aligned} P_{\text{classical}}(\omega) &= \frac{1}{N}\left|\sum_{n=1}^{N} y_n e^{-\omega t_n}\right|^2 \\ &= \frac{1}{N}\left[\left(\sum_n y_n \cos(\omega t_n)\right)^2 + \left(\sum_n y_n \sin(\omega t_n)\right)^2\right], \end{aligned} \tag{3.6}$$

We computed the LS periodogram using `astropy` package (Vanderplas & Ivezić, 2015; VanderPlas et al., 2012). We chose a linear frequency grid with $f \in [0.014\,\mathrm{d}^{-1}, 4\,\mathrm{d}^{-1}]$ and interval $\Delta f = 1/(nT)$. T is the span of the time series and $n$ is the oversampling factor. The oversampling factor $n$ determines the frequency resolution of the periodogram. Normally, $n \geq 5$ is chosen (VanderPlas, 2018). We used $n = 20$. Then, we smoothed the periodogram with a $0.1\,\mu$Hz box car window to reduce the influence of any spurious peaks.

The height of peaks in the periodogram is associated with the goodness of fit. The highest peak usually corresponds to the most significant periodic signal in the data. Hence, we chose the period associated to the highest peak in the LS periodogram as the stellar rotation period and the full width half maximum (FWHM) of this peak as the $1\sigma$ uncertainty of our measurement. To differentiate peaks caused by real signal from those caused by noise, we computed the false-alarm probability (FAP) of the peaks we chose, which estimates the probability of detecting a peak caused by noise (Baluev, 2008) and set a detection threshold of 0.01%.

The Lomb-Scargle periodogram is an effective tool to extract the rotation frequency from a time series especially when the data contains multiple periodic signals with various amplitude and phase. However, VanderPlas (2018) pointed out that the major concern for LS periodogram is not the imprecision of the period detected but rather the inaccuracy caused by false peaks and aliases. For Kepler light curve, false peaks in periodogram may come from the residuals of instrumental perturbation like the monthly Earth-pointing events. As for aliases, they usually occur at $P/n$ in the periodogram, where n is an integer number (Reinhold & Reiners, 2013). One cause of such aliases could be the presence of n active features on the stellar surface distributed near-uniformly in longitude. Another cause is the fitting of a non-sinusoidal wave with a sinusoidal model. The shape of variation in the light curve modulated by an active feature falls between a sine wave and a square wave. As a result, aliases appear at harmonics ($P/2$, $P/3$, ..., $P/n$), often with a decrease in peak height as n increases.

### 3.4.2 The Auto-correlation Function

Auto-correlation function (ACF) measures the correlation between the data itself and a delayed copy of it. For a uniform time series with time interval $\delta t$, the correlation coefficient $r_k$ is given by

$$r_k = \frac{\sum_{i=1}^{N-k}(y_i - \bar{y})(y_{i+k} - \bar{y})}{\sum_{i=1}^{N}(y_i - \bar{y})^2}, \tag{3.7}$$

where the lag $k$ describes the extent of delay, $\bar{y} = \sum_i^N y_i$ is the average of time series, $y_i$ is the data, $i$ is the time index of the data, and $N$ is the total number of data point. The correlation coefficient $r_k$ lies between $-1$ to 1. The sign of the coefficient represents the sign of correlation. The larger the $|r_k|$ is, the stronger the correlation. For example, $r_k = +1$ stands for a perfect positive correlation while $r_k = -1$ represents a perfect anti-correlation. For our Kepler light curve with time span $T$ and $\delta t = 29.4\,$minutes, we computed the correlation coefficients from 0 to a lag of $k_{max}\delta t = T/2$. In the correlation series, aliases caused by multiple active features on the stellar surfaces also occur. The aliases appear as small fluctuations along the peak of actual period. The top panel of Figure 3.10 gives an example of aliases most likely caused by the presence of three active regions on the stellar surface. To mitigate the influence of aliases, we smoothed all the correlation series with a Gaussian smoother (`scipy`, Virtanen et al., 2020) with a $\sigma = 50\,\delta$t width.

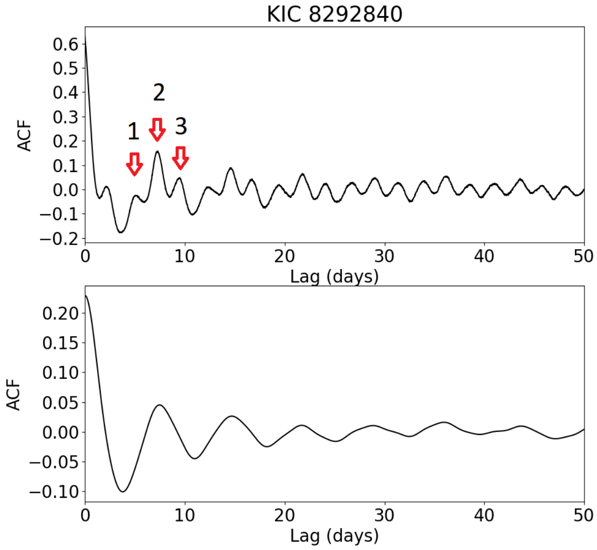

Figure 3.10: Examples of original (upper panel) and smoothed (bottom panel) ACF (KIC8292840). This example illustrates the aliases which are most likely caused by three active regions with near uniform distribution along longitude on the stellar surface. In the upper panel, the peak of actual period $P$ is modulated by a higher frequency signal with $P/3$, leading to three additional small peaks around each the of period $P$. The red arrows marked the three aliasing peaks. After applying the smoothing function (bottom panel), the influence of aliases on ACF is removed.

To extract the stellar rotation period from ACF, there are overall two strategies in the past literatures. The first one is to adopt the lag value at the first maxima as the rotation period $P$ (e.g. García et al., 2014). The second one is to note down the lag values of successive maxima and apply a linear fit to them with respect to the number of maxima. The gradient of the linear fit is chosen as the rotation period $P$(e.g. McQuillan et al., 2014). Considering that coefficient series of our sample do not always give clear repetitive maxima, we instead computed the LS periodogram of the coefficient series. The frequency grid and smoothing window follows the last subsection. We selected the highest peak in the power spectra as the rotation period $P$ and the FWHM of this peak as the uncertainty.

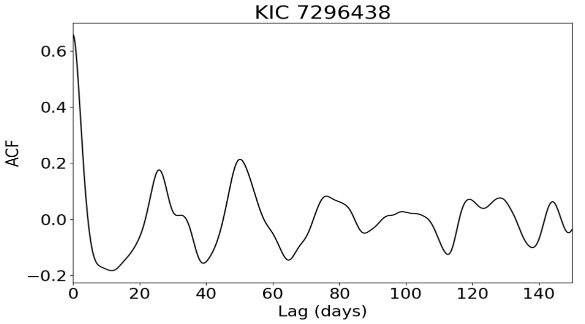

Figure 3.11: An example of smoothed ACF (KIC 7296438) which does not have clear repetitive maxima.

### 3.4.3 Wavelet Analysis

The third method is the wavelet analysis or more specifically the continuous wavelet transform. Wavelet transform decomposes data $x_n$ into a set of basis wavelet functions. Fourier transform is one type of wavelet transform which decomposes data into a set of sinusoidal wave functions. The mathematical definition of continuous wavelet transform is given by (see e.g. Torrence & Compo, 1998).

$$W_n(s) = \sum_{n'=0}^{N-1} x_{n'} \psi^* [\frac{(n'-n)\delta t}{s}], \tag{3.8}$$

where $*$ is the notation for the complex conjugate, $n$ is the localized time index, $\psi$ is the wavelet function of choice and $s$ is the scale of the wavelet function which will be discussed in the following part. $n$ indicates that the center of the wavelet function locates at $n\delta t$ of the time series during the transformation.

There are a variety of wavelet functions designed for different purposes like Meyer wavelet, Mexican hat wavelet and Haar wavelet. One of the most widely used wavelet function in astrophysics and geophysics is the Morlet wavelet (e.g. García et al., 2014; Ceillier et al., 2016), which has the form of a plane wave modulated by a Gaussian:

$$\psi_0(t/s) = \pi^{-1/4} e^{i\omega_0 t/s} e^{-(t/s)^2/2}, \tag{3.9}$$

where $t$ is the time parameter, $\omega_0$ is the dimensionless frequency and $s$ is the scale of wavelet. Morlet wavelet is a sinusoidal like variation with emergence and decay which is well suited for describing the behavior of active features on the stellar surface. $\omega_0$ is chosen to be $\omega_0 \approx 6$ such that the wavelet function can be averaged to around 0 (see e.g. Torrence & Compo, 1998; Farge, 1992). The scale $s$ is associated to the period of variation of the wavelet function. Figure 3.12 gives several examples of the Morlet wavelet functions with scale $s = 1$, 5 and 10 days respectively. If we choose a small scale the wavelet will be more compact while if we select a large scale, the wavelet will be more stretched in time axis.

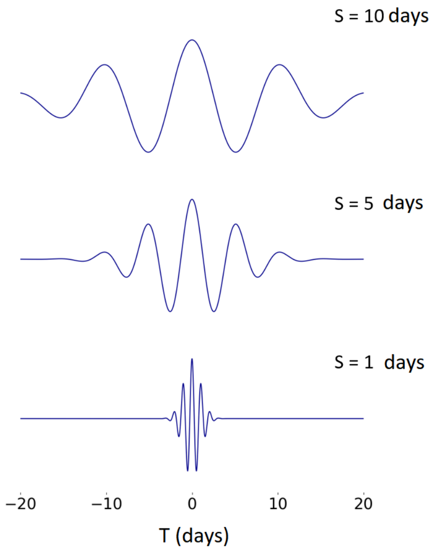

Figure 3.12: Examples of three Morlet wavelets with scale s = 10, 5 and 1 days respectively from top to bottom panels. Scale s corresponds to the period of variation in the Morlet wavelet.

Wavelet analysis provides two powerful tools to study the periodic signals in times series. The first one is the wavelet power spectrum which is a time localized power spectrum. The second one is the global wavelet power spectrum (GWSP) which is an average of power over all localized time for each scale $s$. We compute both wavelet spectra using `waipy` package (Mabelcalim, 2014).

The wavelet power spectrum is defined as $|W_n(s)|^2$. We first computed a series of $W_n(s_0)$ as we slid the wavelet function of scale $s_0$ through the time axis. Then we repeated the same procedure for a group of scales $s_0, s_1, ...s_m$ of our choice. We chose a linear scale for s with a range of $s \in [0, 65]$ and a spacing of 0.01. With the $n \times m$ values of $W_n(s)$, we then computed the wavelet power spectrum $|W_n(s)|^2$. The left panel of Figure 3.13 shows an example of wavelet power spectrum for KIC 3425851. The great advantage of the wavelet power spectrum is its ability to visualize the change of periodic signal along time. In this example, the periodic signal has a period around $P = 8\,$days and lasts during the entire 4-year observation. We can utilize the wavelet power spectrum to trace the duration of a signal and its location in the time axis. One thing to note is that due to the finite length of time series, errors of transformation will appear at the start and end of the power spectrum. The region is defined as the cone of influence and is shaded in black in our wavelet spectrum. An example of the cone of influence can be seen in the bottom left corner and the bottom right corner in Figure 3.13.

The global wavelet power spectrum (GWPS) is defined as

$$\bar{W}^2(s) = \frac{1}{N} \sum_{n=0}^{N-1} |W_n(s)|^2. \tag{3.10}$$

which is an average of power over the time span. The blue curve in the right panel of Figure 3.13 gives an example of GWPS. GWPS behaves like a smoothed spectra which combines a range of close peaks in the Fourier spectrum (gray curve) into one single peak. García et al. (2014) describes such behavior as a degraded resolution of GWPS. On the other hand, Mathur et al. (2010) suggested the width of peak in GWPS takes into account the differential rotation which shows up as close peaks in Fourier spectrum so that GWPS gives a more complete picture of rotation on stellar surface. The GWPS is the major tool in the wavelet analysis which we use to extract the stellar rotation period. We chose the period corresponding to the highest peak as the stellar rotation period $P$ and use the FWHM of the peak as the $1\sigma$ uncertainty of the measurement. In the example given in Figure 3.13, we chose the the highest peak located at $P \approx 8\,$days as the stellar rotation period for this target.

Liu et al. (2007) pointed out that this widely used global wavelet spectrum (Torrence & Compo, 1998) is biased in that when there are multiple periodic signals in a time series, the global wavelet spectrum assigns higher power to the low frequency signal. However, we consider this bias as an advantage of GWPS. The major aliases in the determination of stellar rotation period are the high frequency peaks at $P/2, P/3, ..., etc.$ caused by the presence of multiple active regions on the stellar surface. In GWPS, the high frequency aliases is suppressed which benefits the extraction of actual period $P$.

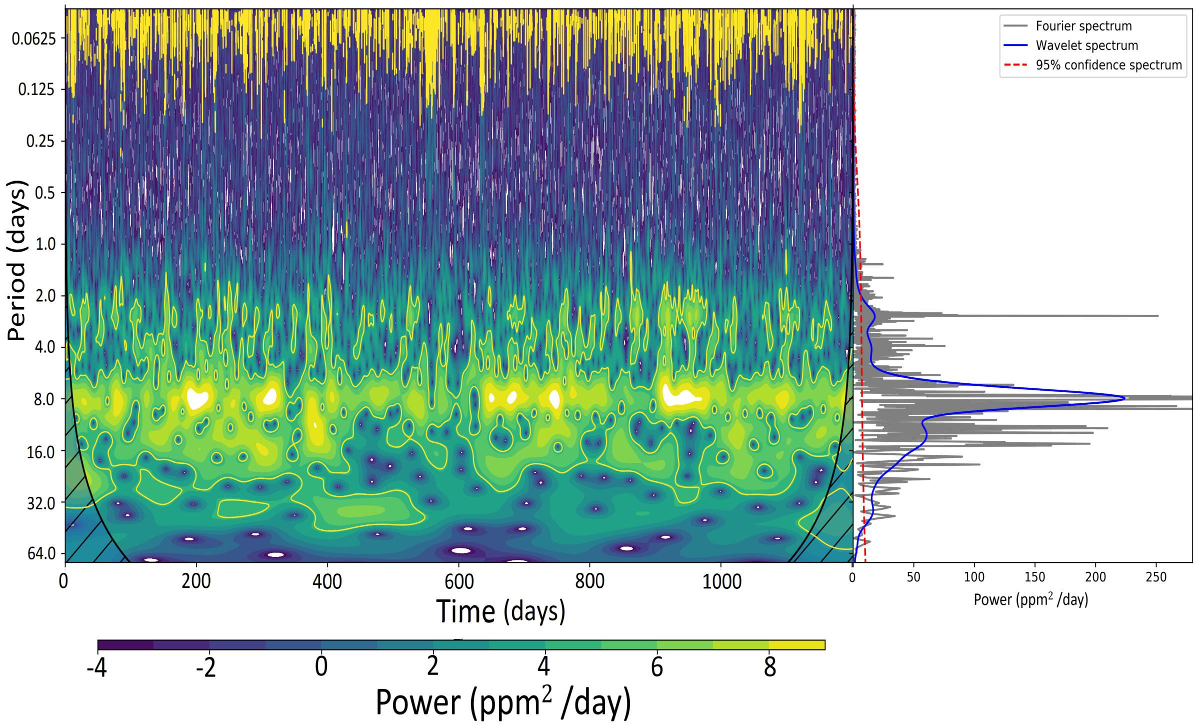

Figure 3.13: Power spectra given by wavelet analysis of KIC 3425851. The left panel is the wavelet power spectrum. The vertical axis is period. The horizontal axis is time. The shaded region near the bottom edge of the waver power spectrum is the cone of influence within which power is less reliable. In the right panel, blue curve is the global wave power spectrum (GWPS) and the gray curve shows the Fourier power spectrum of the light curve.

## 3.5 Results and Discussion: Stellar Rotation Period

In this section, we first examine our photometric estimations by comparison with previous works on photometric analysis and comparison among our different methods. Next, we design a set of criteria to select reliable photometric period estimations $P_{photo}$. We then investigate the reliability of our estimation, especially for reliable $P_{photo}$, with spectroscopic analysis (CKS, Petigura et al., 2017)) and asteroseismic analysis (Kamiaka et al., 2018). Finally we discuss about the suitability of using $P_{photo}$ as a prior for asteroseismic analysis.

### 3.5.1 Comparison with Previous Photometric Analysis

**Comparison with Nielsen et al. (2013) and Karoff et al. (2013)**

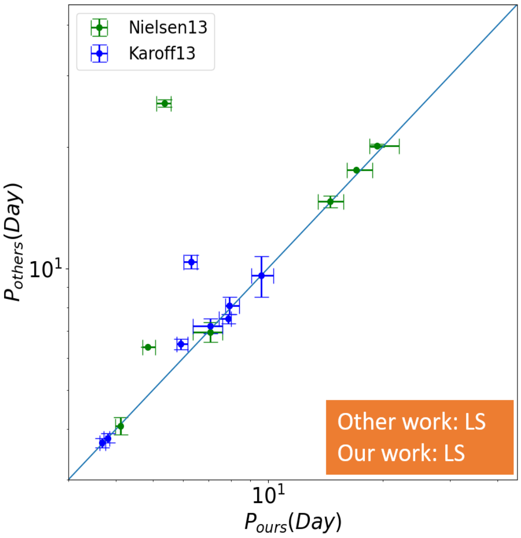

Figure 3.14: Comparison of LS method (15 targets). The x-axis is our LS estimation and the y-axis is the LS results from the other two literatures.

In Figure 3.14, we compare our LS results with those from Nielsen et al. (2013) and Karoff et al. (2013) for 15 targets. Most estimations show reasonably good consistency. We examine the periodogram for cases of disagreement. We noticed that the periods reported by other works are also detected in our periodogram, while the peaks corresponding to those periods are not the most significant one(see e.g. Figure 3.15). Such difference in relative peak height occurs, though rare, when the processing of light curve differs. In addition, a difference in peak selection could happen when visual inspection is involved.

The multiple detected signals in a power spectrum could be the actual signals of rotation (e.g. in the case of differential rotation), or false peaks and aliases. A fair judgement requires additional information. KIC 9139151 and KIC 9139163, which have inconsistent period estimations, are two reported binary systems [1]. Hence, for these two targets, it is likely that multiple periodic signals in the periodogram comes from different stars.

---

[1] Refer to Kepler EB catelog `http://keplerebs.villanova.edu/`

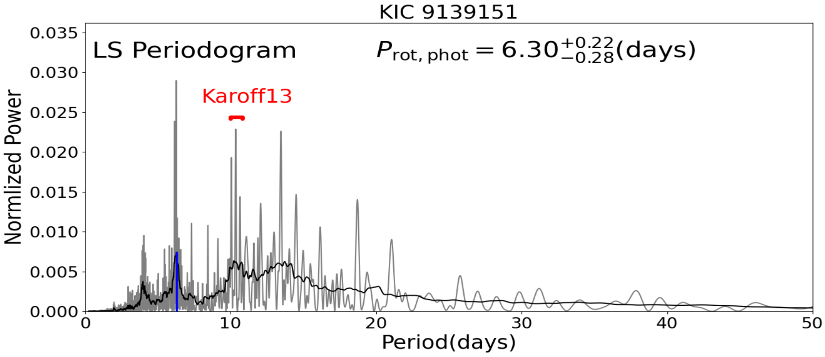

Figure 3.15: Lomb-Scargle periodogram of KIC 9139151. The highest peak at $P = 6.3$ days selected by our method is marked by the blue vertical line. The period selected by Karoff et al. (2013) is marked by red bar around $P = 10.4$ days. This is an example of inconsistent estimations for LS method.

### Comparison with McQuillan et al. (2013b) and McQuillan et al. (2014)

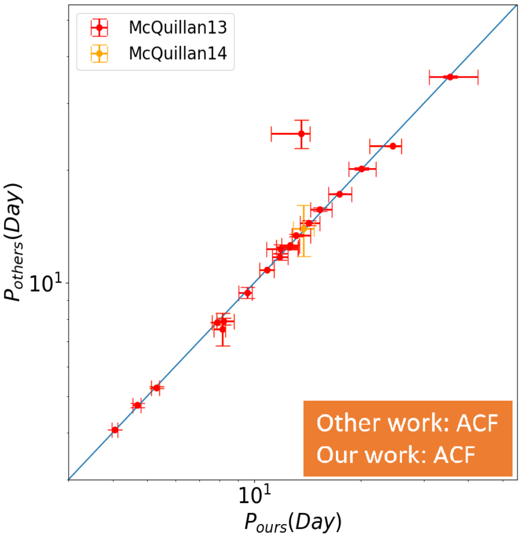

Figure 3.16: Comparison of ACF method (21 targets). The x-axis is our ACF estimation and the y-axis is the ACF results from the other two literatures.

In Figure 3.16, comparison of ACF estimations for 21 targets is plotted. All but one target (KIC 6521045) show good agreement within $1\sigma$ uncertainty. KIC 6521045 is the target with sudden increase in flux variation in one quarter (see Section 3.3). In our preparation of light curve, we delete the strange quarter. We suspect that this processing cause the difference between our measurement and others'. We apply the ACF method again on the light curve without quarter deletion and get the same result as McQuillan et al. (2013b). Hence, there are two periodic components with different period in the light curve of KIC 6521045, a strong one in a single quarter and a mild in the remaining quarters.

If the strong modulation in the strange quarter is caused by a large active region, the lifetime of the signal is expected to be longer than the mild signal, as the lifetime of features like star spots scales with their size. Hence, it is possible that the variation comes from an apparent binary of this system or other systematic perturbation.

### Comparison with Ceillier et al. (2016) and García et al. (2014)

In the work of Ceillier et al. (2016) and García et al. (2014), multiple photometric analyses have been applied to give one best estimation. Ceillier et al. (2016) apply three methods respectively: ACF, wavelet and a so-called Composite spectrum which is the product of ACF coefficients and normalized global wavelet power spectrum (GWPS). They use a different pipeline of light curve (KADACS) from us. They retain all signals with period shorter than 55 days. García et al. (2014) apply both ACF and wavelet methods on two pipelines of light curve (PDC and KADACS) respectively and selected the result having at least partial agreement between different types of light curve. We compare our ACF and wavelet results respectively with their estimations for 41 targets. Since we do not know whether their result comes from ACF or wavelet method, we consider the agreement between their result and one of our ACF and wavelet estimations as a good enough consistency.

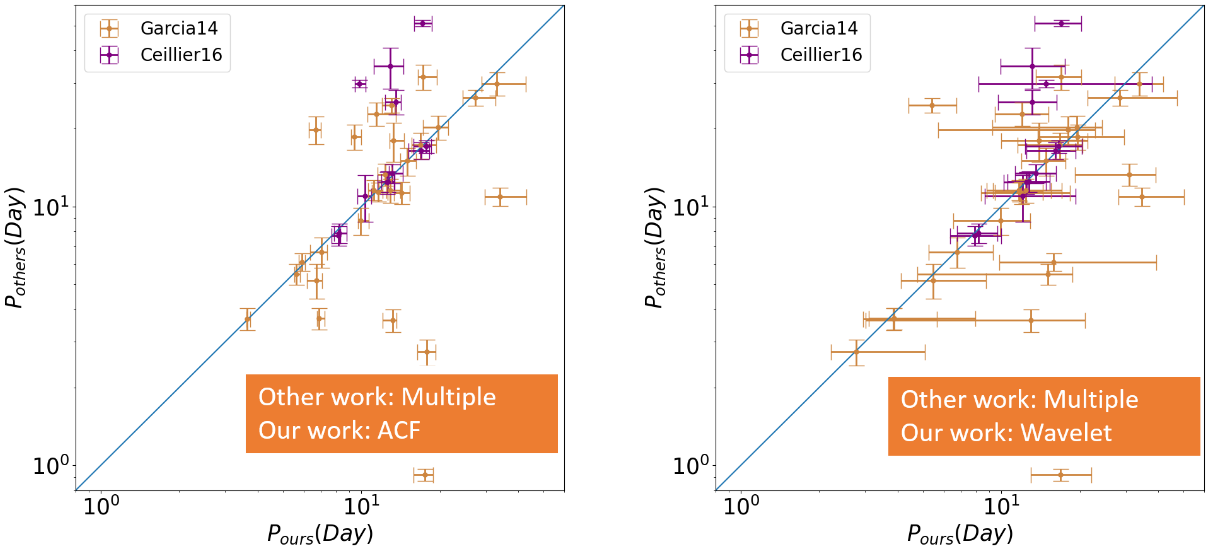

(a) (b)

Figure 3.17: Comparison of rotation period between our work and previous literature for 41 targets. In plot(a), we use our ACF results for comparison. In plot (b), we use our wavelet results for comparison. In all plots, our estimations are plotted in x-axis.

Overall, 10 targets shows complete inconsistency between us. We examined the power spectra of these 10 targets. There are in general three scenarios of discrepancy. The first case includes 6 targets (KIC 3656476, 8179536, 10644253, 12069127, 9025370, 9139163). For them, there are multiple significant peaks in the power spectra. We suspect that the discrepancy comes from the slight difference in relative peak heights between our analysis and theirs, which can be attributed to the difference in processing of light curve.

KIC 9025370 and 9139163 are reported binaries [2], so that the two periodic signals found in their power spectra could come from different stars. For the remaining four targets, additional evidence is required to tell whether the multiple peaks come from the surface rotation or contaminations.

The second case contains two targets (KIC 8349582 and 9410862). In our power spectra, we find barely any signal at the periods indicated by previous literatures. In this two cases, the periods measured by García et al. (2014) and Ceillier et al. (2016) are larger than our estimations, especially for KIC 8349582 where $P_{\rm others} > 50\,$days. Such disagreement could be caused by different high-pass filters applied. Any period $P_{\rm photo} > 50\,$days is not within our detectable region.

The third case includes 2 targets which are KIC 6521045 and 9955598. For these two targets, we deleted those strange quarters with sudden increase in variation during the processing of light curve, which causes the inconsistency in period measurement.

In conclusion, our comparison shows a reasonably good consistency (80%) with previous literature. When the light curve contains homogeneous periodic signal, photometric analyses conducted by different works show nearly perfect consistency. When there are multiple periodic signals (multiple peaks in the power spectrum), the processing of light curve, choice of pipeline and selection criteria of peaks in the power spectra lead to a small portion of different estimations for the same photometric analysis. The multiple peaks in the power spectra could either come from contaminations like binaries and instrumental perturbation (false peaks), or caused by the complex spot configuration on the stellar surface (aliases at $P/2, P/3, ..., etc.$) and surface differential rotations. Hence, the major concern of photometric methods is the inaccuracy in the selection of peak rather than the imprecision of estimations.

### 3.5.2 Comparison Among Three Photometric Method

In this subsection, we compare our period estimations from different photometric methods. In Figure 3.18, we plot the ratio $P_{\rm method}/\left\langle P_{\rm Wavelet}\right\rangle$ against $\left\langle P_{\rm Wavelet}\right\rangle$ for all three methods. The comparison shows a more than 80% of agreement among all methods within $1\sigma$ uncertainty. We then examine the case where discrepancy shows up.

We find that when the light curve contains only one dominant signal, three photometric analyses give perfect consistency within $1\sigma$ uncertainty (see e.g. Figure 3.19). When there are multiple periodic signals embedded in the light curve, power spectra shows multiple significant peaks. All photometric analyses captures the same group of peaks in their power spectra, while the power assigned to each peak is slightly different for each method.

Wavelet has a preference for low frequency signal which is due to an intrinsic bias of this method (see Liu et al., 2007). Such bias induces the discrepancy between wavelet analysis and the other two methods, when there are two or more significant peaks in the power spectrum. An example of such phenomenon is given in Figure 3.20 where LS and ACF methods select the high frequency peak as the period and wavelet method select the low frequency peak. The accumulation of points at $P_{method}/\left\langle P_{Wavelet}\right\rangle \leq 0.5$ further validates the existence of this bias. Mathur et al. (2010) suggested that this property of wavelet could be an advantage in

---

[2] Refer to Kepler EB catelog `http://keplerebs.villanova.edu/`

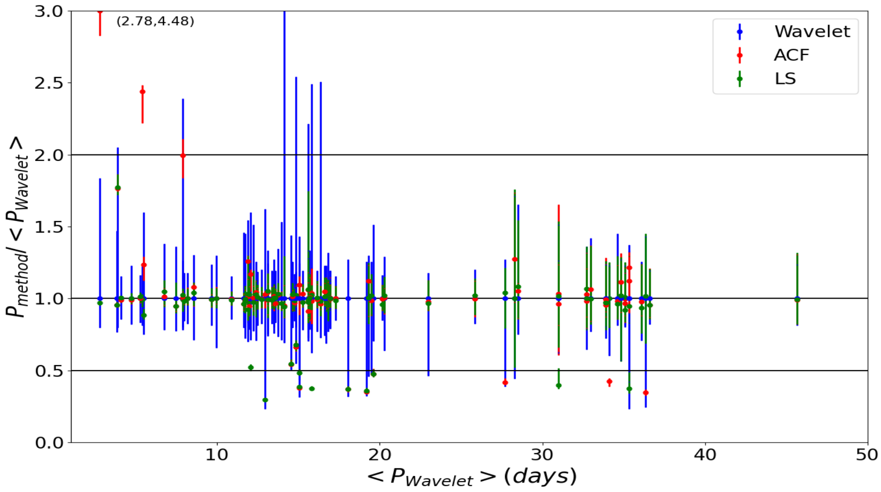

Figure 3.18: Comparison of estimations from different photometric method. Y-axis is the ratio of period from each method to period of wavelet. X-axis is the periods from wavelet method

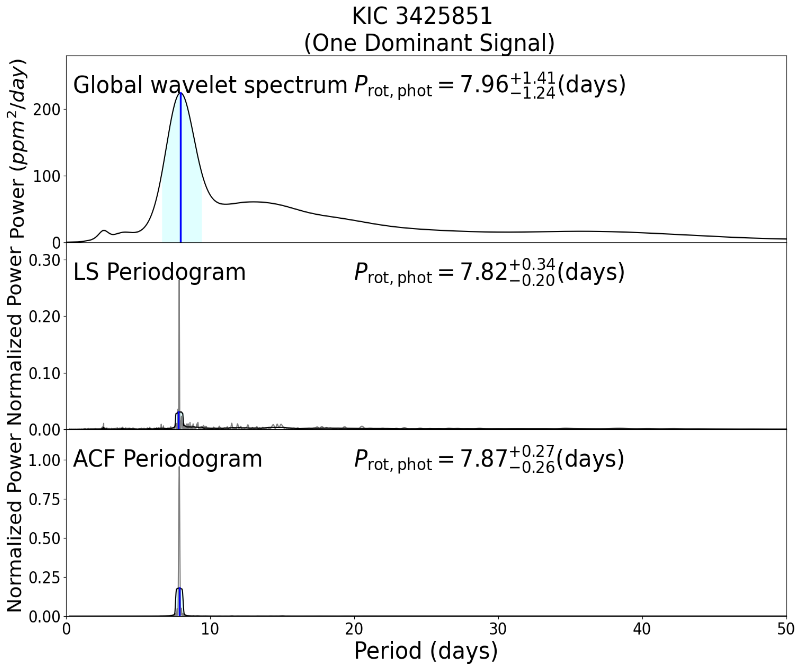

Figure 3.19: Global wavelet power spectrum, LS periodogram, ACF spectrum of KIC 3425851. The power spectra are dominated by one significant peak, which indicates that the light curve contains a rather homogeneous periodic signal. Estimations from three photometric analyses agree well within uncertainty.

that it suppresses the high frequency aliases (at $P/2, P/3, ..., etc$). High frequency aliases are caused by the presence of evenly distributed active regions along the longitudinal direction as well as the non-sinusoidal variation of light curve. On the solar surface, active regions with 180° separation in longitude is occasionally observed. In the case where multiple peaks comes from transient contamination, we can make a rudimentary judgement by checking the cycle of variations in the wavelet power spectrum and rule out the signals with extremely short life time. However, when the time spans are long for multiple signals, photometric analysis can not discern the rotation period from the other source. Such situation could occur when there is a close (apparent) binary around the target.

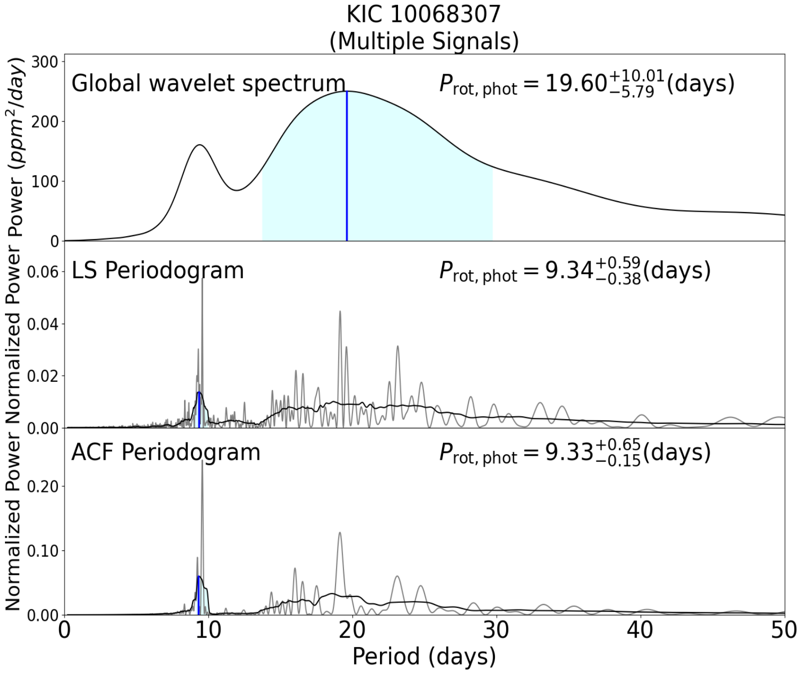

Figure 3.20: Global wavelet power spectrum, LS periodogram, ACF spectrum of KIC 10068307. There are multiple significant peaks at the same location in the power spectra of all photometric methods. LS and ACF method choose the peak at smaller period while wavelet method chooses the peak at larger period.

Another thing to note is that LS method has the best frequency resolution while wavelet has a most degraded resolution. Figure 3.20 serves as an example to illustrate this point. From top to bottom panels, we have the global wavelet power spectrum, LS periodogram and ACF periodogram of KIC 10068307. All spectra capture the same group of peaks. LS and ACF periodograms show much more features than the global wavelet spectrum. Consequently, the $1\sigma$ uncertainty range, which is defined as the FWHM of the selected peak, is largest for wavelet method. Mathur et al. (2010) argues that the uncertainty range of wavelet gives a more realistic account of surface rotation of stars. Since the small features in LS and ACF periodograms could indicate the signals of differential rotations, the uncertainty of wavelet, which covers the range of most features, better describes the surface rotation.

Lastly, we notice that there are two ACF results which are significantly larger than estimations from LS and wavelet analysis. This could happen when the periodic signal is weak and the ACF series is over-smoothed, so that small periodic features given captured by LS and wavelet method are missing in ACF spectrum. There are only two such cases in our sample so we consider our smoothing window for ACF method reasonable.

In conclusion, three widely used photometric methods show a reasonably good consistency in period estimation (> 80%). When the light curve contains homogeneous variation, all photometric analyses give perfect consistency. When there are multiple signals in the light curve, all three photometric methods capture the same group of periodic signal from the data, but assign different power to a same peak. Wavelet analysis tends to prefer low frequency signals. Photometric analyses can not distinguish between the actual rotation signal from other long lasting contamination. Therefore, we have a better chance to obtain a reliable $P_{photo}$ when there is only one dominant periodic signal in the light curve which also lasts for a long time.

### 3.5.3 Classification

In the next step, we would like to compare our results with spectroscopic and asteroseismic analyses. Before that, we classify our targets upon the reliability of their photometric estimations. First of all, we select targets with consistent measurement from all three photometric methods within $1\sigma$ uncertainty. For these targets, we set a few criteria for the next screening. As we mentioned in the previous discussion that contamination of light curve gives false signal which lasts for a short time, we design a rule for each photometric methods to choose the targets with persistent signals.

- **Lomb-Scargle Periodogram**: We introduce a concept called median absolute deviation ratio (MADR) which is adapted from the MAD value defined in Nielsen et al. (2013). We apply the Lomb-scargle periodogram to each quarter $i$ of the processed light curve and assign a period $P_i$ to it. Then we computed MADR values for each target as

  $$MADR = \frac{\langle |P_i - <P_i>| \rangle}{P}, \tag{3.11}$$

  where $P_i$ is the period measured for each quarter, P is the period estimated for the entire light curve, <> is the median operator. This MADR value evaluates the deviation of $P$ signal in each quarter. We set an upper limit of MADR to be 8% (heuristic choice).
- **ACF**: The ACF series of the target should have at least four clear successive maxima.
- **Wavelet**: The signal of estimated $P$ lasts for more than one year in the wavelet power spectrum of the target.

If a target with consistent period measurements satisfies all the above criteria and does not belong to a binary or multiple star system[3], we put it in reliable $P_{\text{photo}}$ group. For the remaining targets, we assign them to the less reliable $P_{\text{photo}}$ group. In total, there are 22 targets in reliable $P_{\text{photo}}$ group and 69 in less reliable $P_{\text{photo}}$ group. In the following subsections, we will examine the consistency of photometric analysis with spectroscopy and asteroseismology.

### 3.5.4 Comparison with Spectroscopic Analysis

We used the projected rotational velocity measurements from spectroscopic analysis and reliable rotation period measurement from asteroseismology Kamiaka et al. (2018) to further examine our photometric estimations. First of all, we computed three rotational velocities $v = \frac{2\pi R_*}{P}$ using three photometric periods for each target[4]. Then we choose the 25 spectroscopic $v \sin i_*$ estimations validated by asteroseismic analysis in Kamiaka et al. (2018) from CKS (Petigura et al., 2017). We compare $v \sin i_*$ values with out estimated rotational velocities $v$ in Figure 3.21.

---

[3] Refer to Kepler EB catelog `http://keplerebs.villanova.edu/`, Open Exoplanet Catelog `http://www.openexoplanetcatalogue.com/` and Table 4 of García et al. (2014).

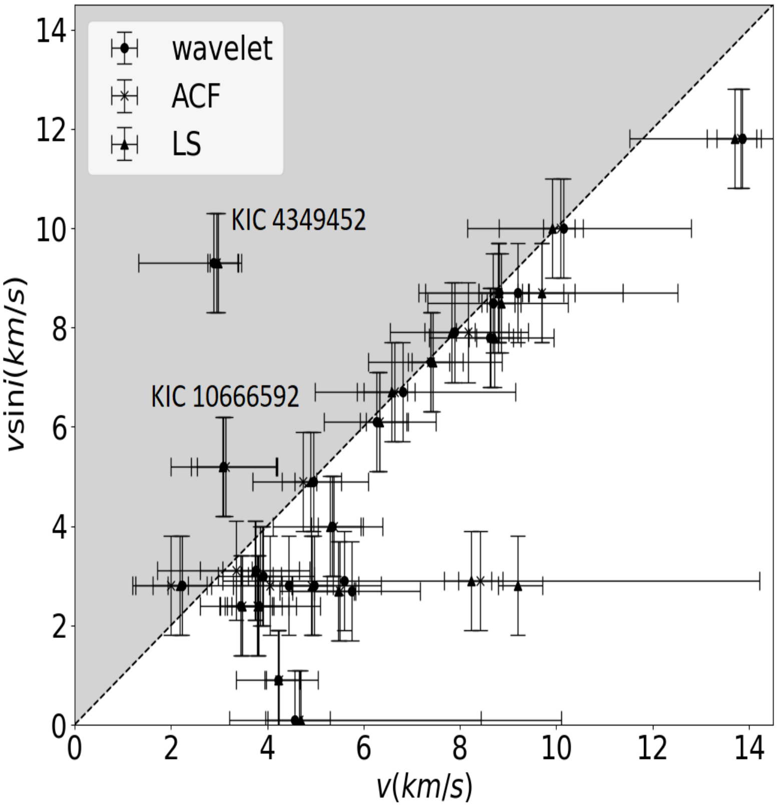

Figure 3.21: Plot of projected rotational velocity $v \sin i$ from spectroscopic analysis against rotational velocity $v$ computed using $P$ from three photometric analyses. $v_* \sin i_*$ measurements come from California-Kepler Survey (CKS:$california{-}planet{-}search.github.io/cks{-}website$). The shaded region is the non-physical region where $\sin i_* > 1$. Corresponding $P_{photo}$ for targets in shaded region should not be trusted.

In general, most of our results ($\sim 90\%$) lie in the physically meaningful region where $\sin i_* < 1$. We identify 2 targets (KIC 10666592 and KIC 4349452 from less reliable $P_{\text{photo}}$ group) in the non-physical region giving $\sin i_* > 1$, indicating that their $P_{photo}$ might be larger than the actual values. The light curve of KIC 10666592 is a too messy to detect a reliable rotation signal. In the power spectrum of KIC 4349452, we capture two significant peaks, one at our estimated period $P$ and the other at $P/2$. Spectroscopic analysis seems to support the period at $P/2$. This raises a caution that high frequency signals could be the actual signals of rotation but not just aliases of the actual low frequency signal. If the high frequency signal (at $P/2$) is an actual signal, then the low frequency signal could either indicates the presence of strong differential rotation or a contamination of light curve by other source.

---

[4] Radius from NASA Exoplanet Archive, Chaplin et al. (2014), Rowe et al. (2014), Stassun et al. (2017), Marcy et al. (2014), Borucki et al. (2010), Carter et al. (2012)

In conclusion, 90% of $P_{photo}$ lie in the reasonable range indicated by spectroscopic analysis. All estimations in reliable $P_{photo}$ group is included in this 90%.

### 3.5.5 Comparison with Asteroseismic Analysis

In this subsection, we compare photometric estimations with asteroseismic measurements. Kamiaka et al. (2018) give asteroseismic inferences of rotation period $P$ for all 91 targets in our sample. They empirically classify their targets into two groups: reliable $P_{\rm astero}$ and less reliable $P_{\rm astero}$. We first compare targets with reliable $P_{photo}$ and $P_{astero}$ to see whether a good photometric estimation also indicates a consistency between photometric and asteroseismic method. Next we compare the rest of stars to evaluate the percentage of overall consistency between these two analyses. Finally, we discuss whether reliable $P_{photo}$ can serve as a proper prior for asteroseismic inference of stellar inclination angle $i_*$. Since photometric methods show relatively good consistency among themselves, we heuristically choose the wavelet result as a fiducial base in our comparison.

#### Reliable $P_{\rm photo}$ Versus Reliable $P_{\rm astero}$

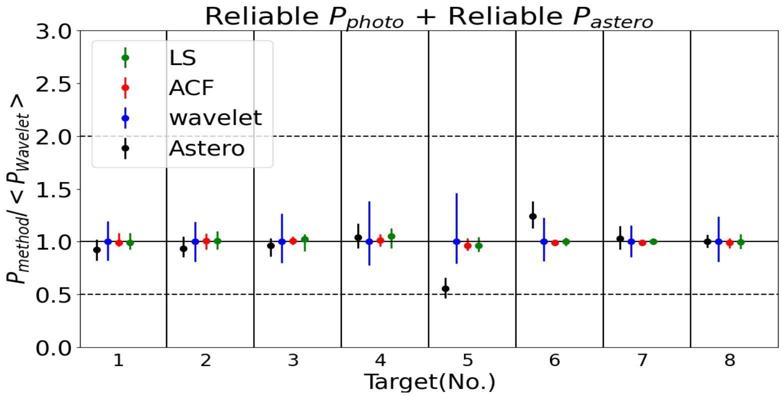

Figure 3.22: Comparison of rotation period for targets with reliable $P_{\rm astero}$ and $P_{\rm photo}$. X-axis is the index assigned to each target. In table in Appendix A.2, we can locate each target with this index. Y-axis is the ratio of period $P_{\rm method}/\langle P_{\rm wavelet}\rangle$. For these 10 targets, all but one show good consistency within $1\sigma$ uncertainty between photometric methods and asteroseismic analysis.

First we compare targets with reliable $P_{\rm photo}$ and $P_{\rm astero}$ (10 targets) in Figure 3.22. The comparison for targets with reliable $P_{\rm astero}$ and $P_{\rm photo}$ shows relatively good consistency within $1\sigma$ uncertainty between photometric methods and asteroseismic analysis. The only target showing discrepancy between two analyses, KIC 5773345 (No. 5), shows no significant peak at the period indicated by $P_{\rm astero}$ in the power spectra of photometric methods (Figure 3.23).

There are two main possible scenarios for this disagreement. Firstly, several possible scenarios for this disagreement. Firstly, despite that this target does not belong to a binary or multiple-star system, it could still have an apparent companion, which refers to the neighboring star along the sky projected view. Secondly, there could be differential rotation on the stellar surface. Since the asteroseismic analysis measures an averaged rotation period over the stellar

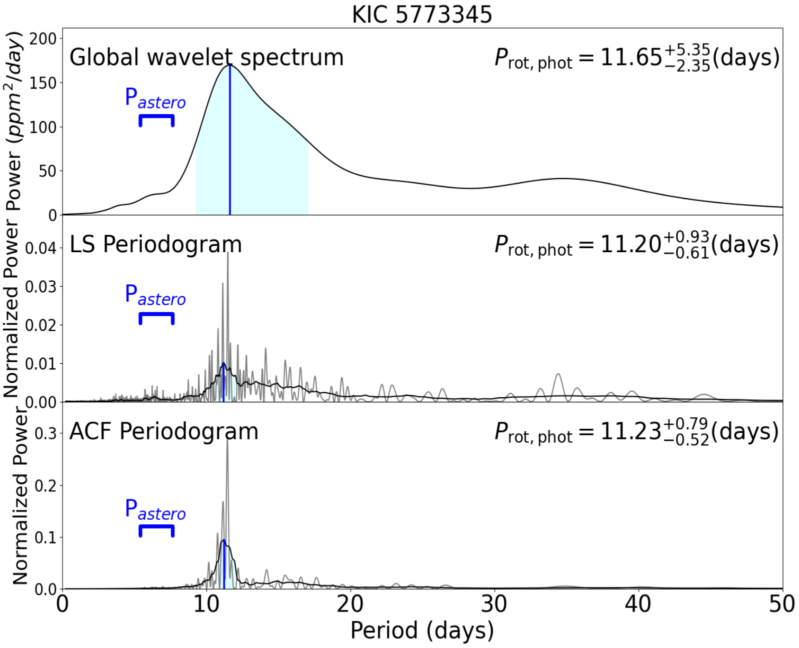

Figure 3.23: Power spectra of photometric analyses (KIC 5773345). $P_{\rm photo} \approx 11$ days while $P_{\rm astero} = 5.43$ days.

surface while photometric analysis probes the period at the latitude where active features locate, disagreement could occur from these two analyses.

We first try to see whether spectroscopic analysis of this target gives us a clue about the source of these two periods. There are two spectroscopic $v \sin i_*$ measurement of this targets, one is $6.6 \pm 1.46$ km/s from Bruntt et al. (2012) and the other is $3.4 \pm 1.1$ km/s from Molenda-Żakowicz et al. (2013). Kamiaka et al. (2018) point out that the spectroscopic measurements from Bruntt et al. (2012) are systematically larger than those from Molenda-Żakowicz et al. (2013). Hence, the discrepancy does not account for the two independent photometric period estimation for KIC 5773345. The rotational velocity of this star computed using $P_{photo}$ is around 9.3 km/s and that computed using $P_{astero}$ is about twice the value. Therefore, both period estimations lie in a physically reasonable range ($\sin i_* < 1$) when compared with spectroscopic $v \sin i_*$ measurements. We can not identify the actual source of two different periods by this comparison.

Next, we use the Gaia data to check for close companions. Gaia has a spatial resolution of 0.4 arcsec while Kepler telescope has 4 arcsec per pixel. Hence Gaia has a better chance to identify close companions. Figure 3.24 shows the image of KIC 5773345 and its surrounding field of radius $r \sim 30$ arcsec, taken by DDS2 [5]. The blue boxes mark the targets identified in Gaia EDR3 (Brown et al., 2020). At the center of image, Gaia only identifies one star which indicates that there is no overlapped targets which can be resolved by Gaia.

The central star is significantly brighter than the surrounding objects. Since the amplitude of observed stellar pulsation pattern scales with luminosity, the resulting asteroseismic estimation

---

[5] Digitized Sky Survey - STScI/NASA, Colored & Healpixed by CDS.

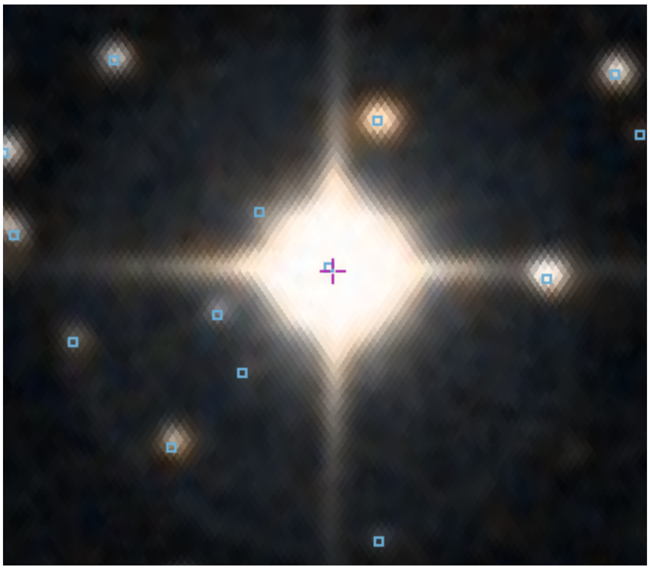

Figure 3.24: Image of KIC 5773345 and its surrounding field of radius $r \sim 30$ arcsec from DDS2 (Digitized Sky Survey - STScI/NASA). The blue box mark the target identified in Gaia EDR3 (Brown et al., 2020). The central star is KIC 5773345.

most likely describes the central star. The central star has a G-band mean flux of $\sim 4.32 \times 10^6 e^-/s$. Its closest companions (within 5 arcsec) has the mean flux of scale $\sim 10^2 e^-/s$. We notice that the variability of the light curve of KIC 5773345 is also of scale $\sim 10^2 e^-/s$. Hence, it is quite unlikely that the photometric variation of light curve comes from these closest companions, because it would require the presence of spots which cover a whole visible disk of the star. The brightest companion around 10 arcsec away from the central star has a mean flux of scale $\sim 10^3 e^-/s$. The photometric variation could possibly come from this star. A further examination of photometric data for this brightest star would give us stronger evidence on the source of discrepancy between period estimation.

Overall, there is a good consistency between reliable $P_{\text{astero}}$ and $P_{\text{photo}}$ (90%) which indicates that our classification for reliable $P_{\text{photo}}$ is also supported by asteroseismic analysis. Next, we compare the rest of our targets (Figure 3.25).

### Overall Comparison

We find 75/91 targets ($\sim$ 80%) show consistency between at least one photometric results (wavelet) and asteroseismic estimations. The 16 targets showing inconsistency can be generalized into 4 cases. The first case contains three reported binary systems (KIC 8379927, 7510397, 9139163). The photometric and asteroseismic analyses might capture the rotation signal from different stars.

The second case includes 6 targets (KIC 5773345, 6933899, 7970740,8006161, 10666592, 8349582). For them, there is no peak associated to $P_{\text{astero}}$ in the power spectra of photometric analyses. One target in this group has both reliable $P_{\text{photo}}$ and $P_{\text{astero}}$. KIC 8349582 has $P_{\text{astero}} > 50$ days which is not within our detectable region. Spectroscopic estimation of $v \sin i_*$ casts doubt on the reliability of $P_{\text{photo}}$ for KIC 10666592. The light curve of this target is relatively noisy with no persistent signal so we are not able to capture reliable rotational modulation. For the

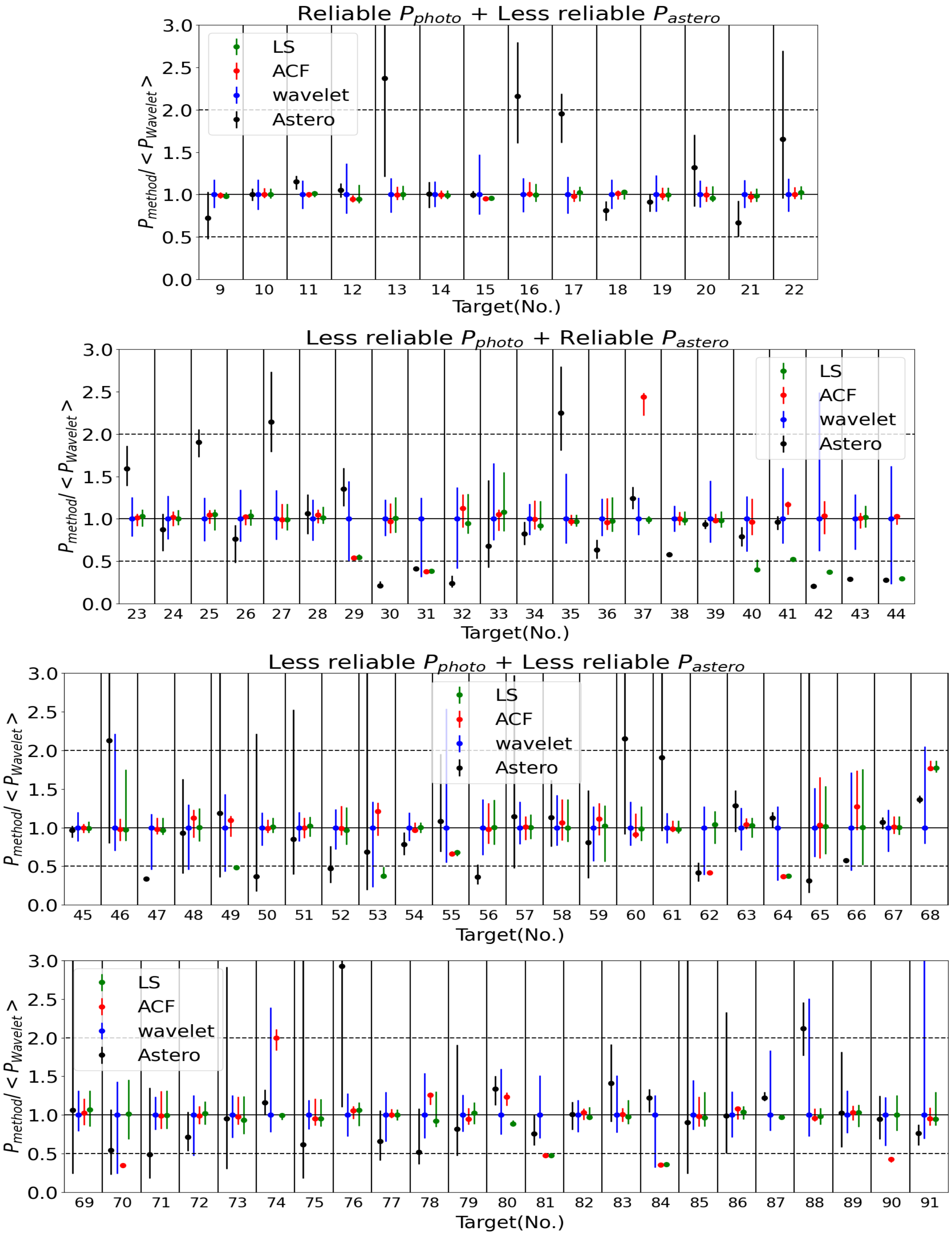

Figure 3.25: Comparison of rotation period from photometric analysis and asteroseismic analysis. X-axis is the index assigned to each target. In table in Appendix A.2, we can locate each target with this index. Y-axis is the ratio of period $P_{\mathrm{method}}/\langle P_{\mathrm{wavelet}}\rangle$. The overall comparison between asteroseismic estimations and photometric results (from at least one method) shows more than 80% consistency within $1\sigma$ uncertainty.

remaining targets, possible reason includes contamination of light curve by instrumental issue, apparent close companion and bias from asteroseismic analysis.

The third case includes 5 targets (KIC 3656476,3544595, 6225718, 9965715, 4349452). For these 5 targets, there are multiple peaks, significant or mild, in their power spectra of photometric analyses, one of which corresponds to $P_{\text{astero}}$. For these targets, some significant peaks could be false peaks caused by contamination from other source or high frequency aliases. $P_{\text{astero}}$ can be a reference for choosing a more reliable peak.

The fourth case is KIC 6521045, 9955598. We find sudden increase in variation in some isolated quarters of these two quarters. We remove this quarters in our analysis. It turns out that $P_{\text{astero}}$ corresponds to variations found in the those deleted quarters.

In general, photometric and asteroseismic analyses show a reasonably good consistency (80%) within $1\sigma$ uncertainty.

### Is $P_{\text{photo}}$ a proper prior for asteroseismic analysis?

Now we are ready to address the problem: Is $P_{\text{photo}}$ a proper prior for asteroseismic analysis? First of all, targets with light curve of consistent level of variation is better suited for this purpose. Next, photometric analyses provide precise estimations: the uncertainty of $P_{\text{photo}}$ is smaller than the less reliable $P_{astero}$ in most cases. However, the accuracy of photometric analyses is not ensured when there are multiple signals captured by the power spectra. Hence, for targets with multiple peaks in their power spectra (less reliable $P_{photo}$), it is not safe to use $P_{\text{photo}}$ as a prior for asteroseismic analysis.

Next we consider targets with relatively clean power spectra showing only one dominant peak (reliable $P_{photo}$). Among these targets, we also find 6 showing inconsistency between photometric and asteroseismic analysis, indicating certain occurrence rate of possible (apparent) binary or strong differential rotation. Hence, a preliminary result from asteroseismic analysis is required. According to the results, we can select targets with overlapped confidence region between photometric and asteroseismic estimations (see e.g. target No. 22 in Figure 3.25). Also, a further validation of $P_{\text{photo}}$ from spectroscopic side is preferred. However, we should bear in mind that the constraint given by spectroscopic analysis is not a strong one.

We find three targets which fit these requirement in our sample, which are KIC 3425851 (No. 9, verified with spectroscopic analysis), KIC 9098294 (No.20, no comparison with spectroscopic analysis) and KIC 12258514 (No.22, no comparison with spectroscopic analysis). Figure 3.26, for example, gives the asteroseismic result for KIC 12258514 from Kamiaka et al. (2018). The top right panel shows the correlation between rotational frequency and stellar inclination angle. The uncertainty range of $P_{\text{photo}}$ is much smaller than that of $P_{\text{astero}}$ (see top panel of Figure 3.25). With the input of $P_{\text{photo}}$ as prior, the tail of $i_*$ distribution towards 90° can be shorten and the precision of $i_*$ could be improved.

In conclusion, we think that reliable $P_{photo}$ selected by our criteria, with overlapped confidence region with $P_{astero}$ could be a reasonable prior for asteroseismic analysis. We find three targets, 1 KOI and 2 planet-less stars, that fit the criteria. However, there are around 7% of our targets having possible strong differential rotation and apparent companion, the signals of which are not captured by photometric analysis at all. In addition, the constraint from spectroscopic

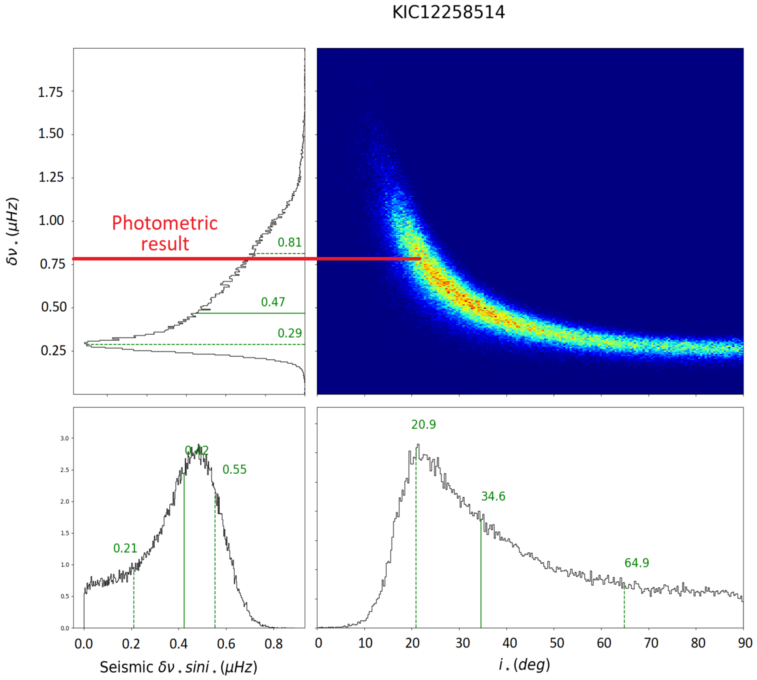

Figure 3.26: Asteroseismic results of KIC 12258514. Top left, bottom left and bottom right panels give posterior distribution of $\delta\nu$, $\delta\nu \sin i_*$ and $i_*$ respectively. The green solid line marks the median of each distribution and the dashed lines indicate the $1\sigma$ confidence interval. Top right panel is the correlation plot of $\delta\nu$ and $i_*$. We can see the correlation between $P$ and $i_*$ in the correlation plot. The red line marks the rotational frequency indicated by photometric analysis. A prior from photometric analysis could largely improve the precision of $i_*$ measurement. Data adopted from Kamiaka et al. (2018).

analysis is not a strong one. Hence, we need to be very cautious about this approach and the selection of suitable targets.

## 3.6 Conclusion and Future Perspective

In this Chapter, we examine the three widely used photometric analyses to extract stellar rotation period, which are LS periodogram, Auto-correlation function (ACF), and wavelet analysis, on 91 solar-type stars. We notice that for our sample there are in general two types of light curve. The first type contains only one dominant periodic signal. The power spectra of such light curve is relatively clean with only one significant peak associated to the period of variation. For targets in this group, all photometric analyses give consistent estimation of period within $1\sigma$ uncertainty. The second type contains multiple periodic signals with different periods. Power spectra of all photometric analyses capture the same groups of peaks. The multiple peaks in the power spectra could be caused by contamination from instrumental perturbation or close (apparent) companions. They could also be the high-frequency aliases of the actual periodic signal. The high-frequency aliases have significant power under a combination of two circumstances:when the variation of light curve is not perfectly sinusoidal and when multiple active regions on stellar surface distributed evenly along longitudinal direction.

When there are multiple peaks in the power spectra, the power assigned to each peak is different for each method. Wavelet analysis (Torrence & Compo, 1998) assigns relatively high powers to peaks at low frequency, which is due to an intrinsic bias of this method Liu et al. (2007). Mathur et al. (2010) consider this property of wavelet analysis as an advantage in that it suppresses the high frequency aliases. LS periodogram has the highest frequency resolution while wavelet analysis has the most degraded resolution. As a result, wavelet analysis tends to have a larger error bar. However, we notice that the major concern of photometric method is not the imprecision of estimation but rather the inaccuracy. Wavelet power spectrum can rule out the transient contamination by tracing the duration of a signal. However, when there are multiple long lasting periodic signals, photometric analysis by its own is not enough to discern the rotation period (e.g. differential rotations) from contamination of other light curve or high frequency aliases. In such case, validation from other approach like spectroscopic and asteroseismic analyses is needed.

Then, we design a set of criteria to select reliable photometric estimations $P_{\text{photo}}$, based on the persistence of the periodic signal and the homogenity of light curve variation. The reliable $P_{\text{photo}}$ group contains 22 targets. The less reliable $P_{\text{photo}}$ group contains 69 targets. We combine our $P_{\text{photo}}$ with stellar radius $R$ to give estimations of rotational velocities $v$. Then we compare our result with reliable spectroscopic estimations of $v \sin i_*$ for 25 targets, 9 from reliable $P_{\text{photo}}$ group and 16 from less reliable $P_{\text{photo}}$. All 9 targets in the reliable $P_{\text{photo}}$ group lie in the physically meaningful region ($\sin i_* < 1$).

Next, we compare our result $P_{\text{photo}}$ with asteroseismic estimations $P_{\text{astero}}$ from Kamiaka et al. (2018). A general comparison for all targets and find $\sim 80\%$ consistency, which indicates a reasonable reliability of photometric methods to extract stellar rotation period. Kamiaka et al. (2018) also divide their targets into reliable $P_{astero}$ group and less reliable $P_{\text{astero}}$ group. We compare the 8 targets with reliable $P_{\text{photo}}$ and $P_{\text{astero}}$. 7 out of 8 targets show good consistency within $1\sigma$ uncertainty. For the remaining one target (KIC 5773345), we examine their power spectra from photometric analyses. We found no peak that corresponds to $P_{\text{astero}}$.

One possible reason for such discrepancy is the presence of differential rotation on the stellar surface. Since the asteroseismic analysis measures an average rotation period on the stellar surface while the photometric analysis measures the period at the latitude where active features locate, discrepancy in estimation could occur when rotation period at the stellar surface varies along latitude. The second possibility is the presence of close (apparent) companions. We check the Gaia EDR3 (Brown et al., 2020). We identify two bright stars located about 10 arcsec away from KIC 5773345 which could be the source of flux variation. However, since both Kepler and TESS do not provide photometric data of these two stars, extra observation of them are required to verify the actual source of the two periodic signals revealed by different analysis.

Finally, we discuss about the suitability of using $P_{\text{photo}}$ as a prior to improve asteroseismic estimation of stellar inclination angle $i_*$. We think that $P_{\text{photo}}$ values are suitable choices for priors in asteroseismic analysis when they meet two criteria. Firstly, in the power spectra of photometric analysis of the target, there should be only one dominant peak, which is the case for targets in reliable $P_{\text{photo}}$ group. Secondly, $P_{\text{photo}}$ has overlapped $1\sigma$ confidence regions with $P_{\text{astero}}$. When the uncertainty range of $P_{\text{astero}}$ is much larger than $P_{\text{photo}}$, the improvement in $i_*$ will be significant. However, we should bear in mind that such approach has a high risk: More than 60% of stars are from binary or multiple star systems, the rotational modulation of light curve for which could be too weak to detect by photometric analysis. Under such circumstance, asteroseismic and photometric analyses are analyzing different stars so that $P_{\mathrm{photo}}$ will not be a proper prior. To conclude, reliable $P_{\mathrm{photo}}$ could potentially improve the asteroseismic inference of stellar inclination $i_*$ significantly. However, the selection of target should be very careful. From our sample, we find 3 targets which fit the requirement.

In the future, we first plan to implement our $P_{\mathrm{photo}}$ as priors for asteroseismic analysis for the three targets we identified. Next, we plan to apply star spot modeling to stars which show possible signs of differential rotation (e.g. KIC 5773345). Star spot modeling is a potentially powerful technique to trace the location of active features. Davenport et al. (2015) demonstrate its power to reveal the differential rotation and spot evolution on the stellar surface. They successfully detect a differential rotation rate of $\Delta\Omega = 0.012 \pm 0.002\,\mathrm{rad\,day^{-1}}$ on an active M4 dwarf. Furthermore, for systems with transiting planet, the modeling of transit over star spots is likely to provide further hint on the spot location as well as the configuration of exoplanetary system (Dai & Winn, 2017).

# Chapter 4

# Asteroseismic Analysis of Stellar Inclination Angle

## 4.1 Motivation

Asteroseismology has been an important independent approach to estimate stellar rotation period and inclination angle. However, it is pointed out by e.g. Ballot et al. (2006) and Kamiaka et al. (2018) that the estimation of stellar rotation period becomes more difficult and less reliable for a slow rotator which has a period of tens of days, especially when the signal to noise ratio is not high enough. In addition, Ballot et al. (2006) suggested that the rotational splitting $\delta\nu$ and the stellar inclination $i_*$ are correlated for slow rotators as $\delta\nu \sin i_* \approx$ constant, so that a bias in either the rotational splitting $\delta\nu$ or stellar inclination angle $i_*$ may have huge influence on the other. Kamiaka et al. (2018) noticed similar correlation, an example of which is illustrated in Figure 4.1. Furthermore, Kamiaka et al. (2018) found that even for stars with high SNR spectrum and for fast rotators, the accurate estimation of stellar inclination angle can only be done within the range $i_* \in [20°, 80°]$. New perspective is needed to improve the asteroseismic estimation of stellar inclination. In this Chapter, we first discuss about the past method to extract stellar parameters, and then introduce two ongoing attempts to improve asteroseismic analysis.

## 4.2 Model of Stellar Oscillation Spectrum

Solar-like stars have sub-surface convection zones. The turbulent motions in this zone stochastically excite and damp acoustic oscillations (pressure p modes) (e.g. Duvall Jr & Harvey, 1986; Goldreich & Kumar, 1988), which can be described by the simple oscillator equation with a damping term and a stochastic energy source term (see e.g. Anderson et al., 1990; Appourchaux, T. et al., 1998). Consequently, in the Fourier spectrum, these oscillation modes can be approximated as Lorentzian profiles:

$$L(A, \nu_0, \Gamma; \nu) = \frac{H}{1 + (\frac{\nu - \nu_0}{\Gamma/2})^2}, \tag{4.1}$$

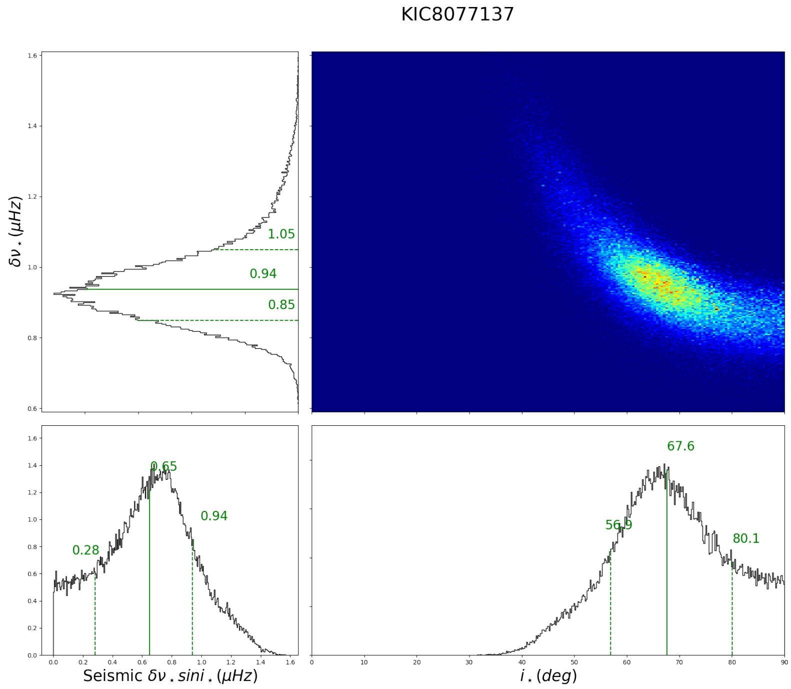

Figure 4.1: Asteroseismic results of KIC 8077173. Top left, bottom left and bottom right plots give posterior distribution of $\delta\nu$, $\delta\nu \sin i_*$ and $i_*$ respectively. Top right is the correlation plot of $\delta\nu$ and $i_*$. The green solid line marks the median of each distribution and the dashed lines indicate the $1\sigma$ confidence interval. Data adopted from Kamiaka et al. (2018).

where $H$ is the mode height, $\Gamma$ is the mode line width and $\nu_0$ is the mode frequency.

The rotation rate of the solar type stars is not too rapid to distort severely the spherical symmetry of the star. Therefore, the oscillation modes can be described by the spherical harmonics, characterized by three wave numbers $n$, $l$ and $m$. The modeled power spectrum is a superposition of all oscillation modes:

$$\begin{aligned} M(\nu,\theta) &= P(\nu) \\ &= \sum_{n=n_{\min}}^{n_{\max}} \sum_{l=0}^{l_{\max}} \sum_{m=-l}^{+l} \frac{H(n,l,m,i_*)}{1+4[\nu-\nu(n,l,m)]^2/\Gamma^2(n,l,m)} + N(\nu), \end{aligned} \tag{4.2}$$

with a background noise model $N(\nu)$. The main sources of noise are granules and spots on the stellar surface. Granules are convective structures with characteristic life times ranging from a few minutes to days. The stellar spots are dark region on the stellar surface caused by magnetic activity. They exist within a limited lifetime which is positively correlated with their size. Hence, the noise model can be well approximated by a generalized semi-Lorentzian which is a monotonically decreasing function of frequency with gentle slope, as well as a white noise:

$$N(\nu) = \sum_i \frac{A_i}{1 + (2\pi\tau_i\nu)^{p_i}} + N_0, \tag{4.3}$$

where $\tau$ is the characteristic lifetime, $A$ is the height and p is the slope of semi-Lorentzian.

In the real practice, the choice of background model depends on the number of mode included in the fitting. Usually if only one radial mode $(n_0, l, m)$ is fitted, the background is considered as flat (e.g. Kuszlewicz et al., 2018). As the noise background is a monotonic function which varies slowly with frequency, for the small range of frequency, the variation is negligible. If multiple radial modes are fitted, a combination of semi-Lorentzian functions and white noise is adopted. In Kamiaka et al. (2018), for example, the background is modeled as the sum of two semi-Lorentzian functions with white shot noise.

The height $H(n, l, m, i_*)$ of each mode in the power spectrum is expressed as $H(n, l, m, i_*) = \mathscr{E}(l, m, i_*)H(n, l)$ with

$$\mathscr{E}(l, m, i_*) = \frac{(l - |m|)!}{(l + |m|)!}[P_l^{|m|}(\cos i_*)]^2, \tag{4.4}$$

where $P_l^{|m|}$ is the associated Legendre polynomials with degree $l$ and order $m$ (Gizon & Solanki, 2003). The intrinsic height of the oscillation $H(n, l)$ is approximated as

$$H(n, l) = V_l^2 H(n, l = 0), \tag{4.5}$$

where $V_l$ is the mode visibility. The mode visibility is a geometric effect as a function of $l$ which is calculated by the integration of pulsations over the stellar disk, taking into account the limb darkening effect (Ballot, J. et al., 2011; Chaplin, W. J. et al., 2008).

$\Gamma(n, l, m)$ represents the peak width of each mode $(n, l, m)$. Since the dependence of $\Gamma$ on m is weak, it is usually reduced to $\Gamma(n, l)$ in the fitting of model. The central frequency $\nu(n, l, m)$ is given by

$$\nu(n, l, m) = \nu(n, l) + m\delta\nu_* \approx (n + \frac{l}{2} + \varepsilon_{n,l})\Delta\nu + m\delta\nu_*, \tag{4.6}$$

where $\Delta\nu$ is the frequency spacing between neighboring radial modes, $\epsilon_{n,l}$ is a small correction term (see Ledoux, 1951; Tassoul, 1980; Mosser, B. et al., 2013). The rotation of star breaks the degeneracy of $l$ mode and splits then into $(2l + 1)$ $m$ modes. $\delta\nu_*$ represents the splitting width between successive $m$ modes. The inverse of $\delta\nu_*$ is the averaged rotation period of a star.

## 4.3 Past Attempt to Extract Stellar Parameters

Stellar parameters like rotational frequency and inclination can be extracted by fitting the observed Fourier spectrum with its model. Bayesian statistics is a popular technique for the regression. First and most importantly, a likelihood function which contains the information of model need to be constructed. Assuming the noise in time series is Gaussian, the noise statistics of its power spectrum obeys $\chi^2$ distribution with two degrees of freedom (see e.g. Groth, 1975).

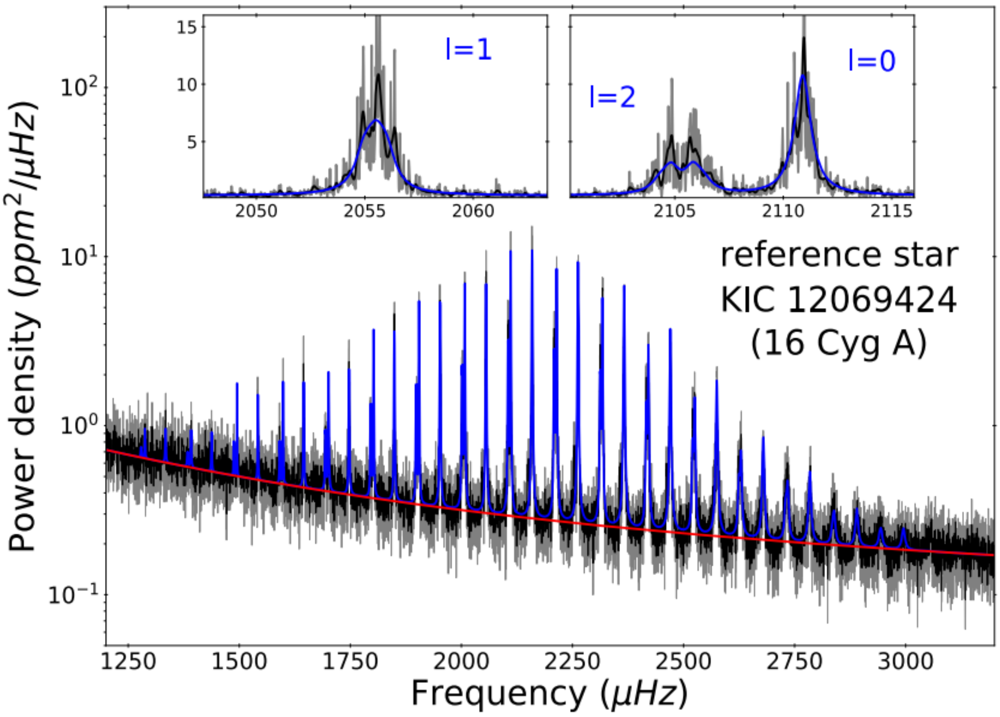

Figure 4.2: Power spectrum of KIC 12069424. Black and Grey curve are power spectra smoothed with Gaussian filters of width $0.25\Delta \approx 25.5\mu Hz$ and $0.05\Delta \approx 5.2\mu Hz$ respectively. Red curve is the ground level and blue curve is the fitted power spectrum. Plot is adopted from Kamiaka et al. (2018).

Hence, the probability density of power spectrum is given by (Duvall Jr & Harvey, 1986)

$$p(y|\theta, M) = \prod_{i=1}^{N} \frac{1}{M(\nu_i, \theta)} exp\left(\frac{-y_i}{M(\nu_i, \theta)}\right), \tag{4.7}$$

where i is the index for frequency, $\theta$ represents the parameters, $M$ is the modeled power spectrum and $y_i$ is the value of the observed power spectrum at frequency $\nu_i$. This probability density is the likelihood function which measures the goodness of fit of the modeled power spectrum to the observed data.

Next, there are two main approaches to do the regression. The first one is the maximum likelihood estimation which refers to a maximization of the likelihood function $p(y|\theta, M)$ in Equation (4.7)(e.g. Anderson et al., 1990; Gizon & Solanki, 2003; Ballot et al., 2006; Appourchaux, T. et al., 2008). The second one is the posterior sampling over a region of parameter space(Kamiaka et al., 2018).

Posterior sampling makes use of Bayes' theorem

$$p(\theta|y) = \frac{p(\theta)p(y|\theta)}{p(y)}, \tag{4.8}$$

which combines the prior knowledge of parameter $\theta$ into the fitting of model. $p(\theta)$ is the prior, $p(y|\theta)$ is the likelihood function and $p(\theta|y)$ is the posterior probability of of the fitted parameter.

Markov Chain Monte Carlo (MCMC) method is used to estimate the posterior distribution by random sampling in a probabilistic space. There are various strategies of MCMC method like Metropolis-Hasting algorithm (e.g. Benomar, 2008; Benomar et al., 2009) and Gibbs sampling. The choice of strategies vary among work.

Both attempts have been made for asteroseismic analysis. Maximum likelihood Estimation is faster to compute relative to posterior sampling. However, it has a higher chance to obtain a local maxima, instead of the actual one. The posterior sampling not only conducts a better exploration over the parameter space but also evaluates the uncertainty of inferences by giving a relatively continuous sampling of probability.

One thing that current asteroseismic studies found in common is the bias of $\delta\nu$ and $i_*$ measurements in certain parameter space (e.g. Ballot et al., 2006; Kamiaka et al., 2018). Ballot et al. (2006) attempt to study the source of bias. Firstly they simulate spectra of 150-day long CoRoT-type observations. Then, they use MLE method to fit their simulated spectra of several successive modes ($l$ = 0,1 and 2 ). During the fitting, they fix all the input parameters $\theta$ to their true values except for $i_*$ and $\delta\nu$. Also, instead of fitting $i_*$ and $\delta\nu$ as two separate parameters, they fit $\delta\nu \sin i_*$ and $i_*$.

In their results, bias in $\delta\nu \sin i_*$ measurements vanishes, while that in $i_*$ remains. This indicates that $\delta\nu$ and $i_*$ are strongly correlated. To illustrate the possible reason for such correlation, we plot a schematic illustration of modeled power spectra of a $l = 1$ mode, with different inclination angle $i_*$ and rotation rate in Figure 4.3. In this figure, the variation of rotation rate is represented by different splitting to width ratio $\delta\nu/\Gamma$. For slow rotators with small $\delta\nu/\Gamma$ (right column of Figure 4.3), the different $m$ modes are blended together so that it is difficult to distinguish between different inclination angle according to their total power spectrum (black line). In addition, if we look at power spectrum of $\delta\nu/\Gamma = 0.5$ and $i_* = 40$ and that of $\delta\nu/\Gamma = 0.3$ and $i_* = 60$, we will find that they are actually quite similar with only subtle difference. Hence, the similarity in the power spectra could lead to a strong degeneracy between $\delta\nu$ and $i_*$ values.

Kamiaka et al. (2018) use the Bayesian-MCMC sampling method (Benomar, 2008) to their simulated spectra of 1 year and 4 year kepler-type observations. Similarly, their results also show a bias in the estimation of $i_*$ and $\delta\nu$. Measurements of $i_*$ around the edge at 90° and 0° are shifted towards the middle values within the range $[0°, 90°]$. Only stars with $20° \lesssim i_* \lesssim 80°$, $\delta\nu/\Gamma \gtrsim 0.5$ with reasonably high SNR and long observations ($\sim 4\,$years) could obtain reasonably reliable results.

In the next session, we will introduce our attempts to tackle this biasing problem.

## 4.4 Method

In this section, we introduce two attempts to improve the biased measurement of $\delta\nu$ and $i_*$. The first attempt is a two-level hierarchical Bayesian model (HBM) introduced by Kuszlewicz et al. (2018). This model uses a hierarchical structure to analyze clusters of measurements. In the first level, the theoretical model is fitted for each cluster and a set of parameters is assigned. In the second level, a new distribution is constructed to describe the distribution of all sets of parameters from different clusters. This method allows us to evaluate uncertainty

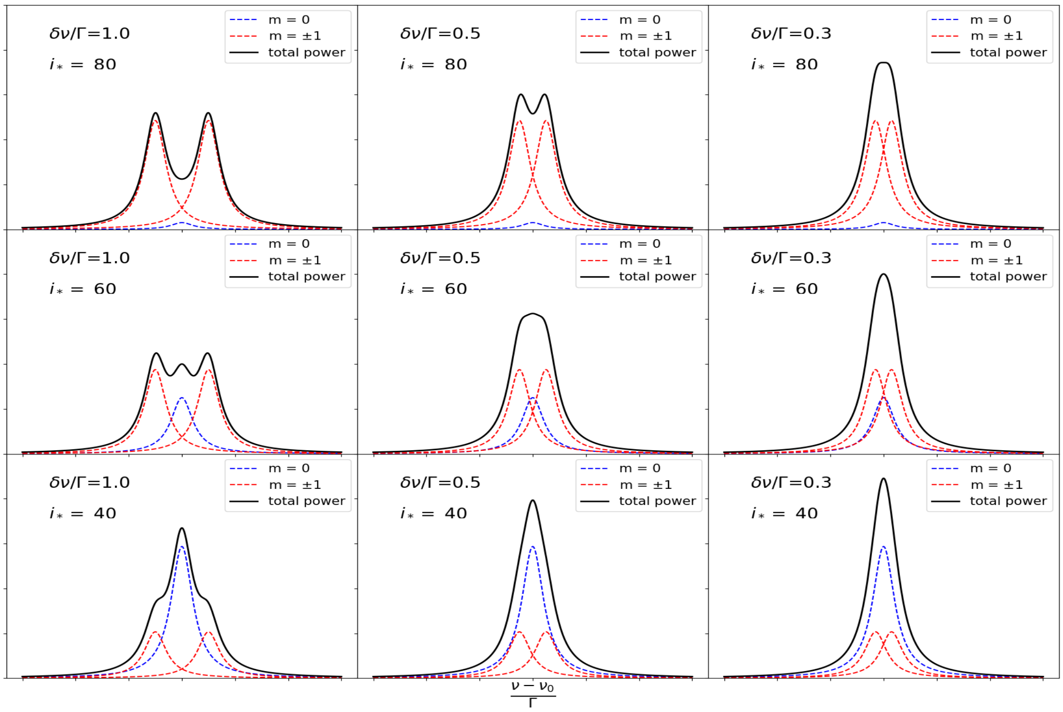

Figure 4.3: Schematic illustration of power spectrum of $l = 1$ mode. Rotation splits the $l = 1$ mode into 3 different $m$ modes. Blue dotted line represents $m = 0$ mode and red dotted lines show $m = 1/-1$ peaks. $\delta\nu$ is the splitting between different $m$ modes and $\Gamma$ represents the width of peaks (Kamiaka et al., 2018).

from each cluster properly so that it is likely to provide us with a more unbiased estimation. In previous attempts, the entire power spectrum are fitted at once without considering the fact that every mode $(n_0, l, m)$ in the spectrum has different signal to noise ratio which could lead to different uncertainty level of estimations. By using HBM, we can divide the spectrum into groups of multiplets $(n, l)$ and evaluate their uncertainty separately so that any bias from one group will not significantly influence the whole measurements. Kuszlewicz et al. (2018) report a successfully improvement of inclination estimation around $i_* < 20°$ and $i_* > 80°$ for red giant stars.

The second attempt that we made also divide the whole estimation process into two steps. In the first step, we do the fitting of the parameter $\mathscr{E}(l, m, i_*)$ from $H(n, l, m, i_*) = \mathscr{E}(l, m, i_*)H(n, l)$ instead of $i_*$ over the entire spectrum using MCMC package provided by Benomar et al. (2009). Then we compute a least square fitting of the posterior samples to the modeled $\mathscr{E}(l, m, i_*)$ and extract the $i_*$ value. The purpose of this process is to avoid the bias caused by complexity and degeneracy from the non-linear relation between $\delta\nu$ and $i_*$ given in Equation (4.4) and (4.6).

### Data

We use simulated 4-year Kepler type data from Kamiaka et al. (2018) to test our method. To simulate the data, Kamiaka et al. (2018) first carry out the asteroseismic analysis mentioned in previous section to their reference star KIC 12069424 (16Cyg A) and extract all parameters described in Equation (4.2). They fit 17 radial orders $(n)$ with their corresponding degrees $l$ =0, 1, and 2. To compute a variation of simulated power spectrum, they vary three parameters which are height $H(n, l = 0)$, $\delta\nu/\Gamma$ and $i_*$.

With the measurements of mode height $H(n, l = 0)$ and the white noise parameter, they generate grids of height $H(n, l = 0)$ values for simulated spectrum by

$$\begin{aligned} H_{\text{sim}}(n, l = 0) &= HBR_{\text{sim}}(n, l = 0)N_0 \\ &= \frac{HBR_{\text{max,sim}}}{HBR_{\text{max,ref}}} HBR_{\text{ref}}(n, l = 0)N_0, \end{aligned} \tag{4.9}$$

where $HBR_{\text{ref}}$ is the ratio between mode height $H(n, l = 0)$ and the white noise parameter $N_0$ measured by the asteroseismic analysis of the reference star and $HBR_{\text{max,ref}}$ is the maximum $HBR_{\text{ref}}$ among all radial order $n$. Figure 4.2 illustrates the $HBR$ values for different radial order. We can see that in the power spectrum, $HBR_{\text{ref}}$ reaches the maximum value $HBR_{\text{max,ref}}$ at around 2100 $\mu$Hz (approximately the highest peak) and decreases towards higher can lower frequencies. They fix the white noise parameter $N_0$ as the value from the reference star and vary the $HBR_{\text{max,sim}}$ in order to have different simulated height value $H_{\text{sim}}(n, l = 0)$.

Next, they generate a grids of $\delta\nu/\Gamma$ values. They fix the $\Gamma$ value to the maximum one $\Gamma_{\texttt{max,ref}}$ measured from the reference star and vary the $\delta\nu$ values. Finally, they also compute a grids of $i_*$ values for generating simulated power spectrum. They generate power spectrum using model 4.2. The grids of varying parameters are summarized in table 4.1 (Kamiaka et al., 2018).

| Parameter | value and range |
|---|---|
| $HBR_{\texttt{max,ref}}$ | [0, 1, ..., 29, 30] |
| $\delta\nu/\Gamma_{\texttt{max,ref}}$ | [0.1, 0.2,..., 0.9, 1.0] |
| $i_*$ | [0, 10, ..., 80, 90] |

Table 4.1: Grids of the control parameters for simulation of power spectra.

We test our method by comparing our measurements with the input parameters for simulating the spectrum.

### 4.4.1 Hierarchical Bayesian Model

#### Introduction

A hierarchical Bayesian model is a multi-level statistical model which estimates posterior distribution of parameters using the Bayesian method. When an analysis has been made to clusters within a population, individuals from the same cluster is likely to display more similarity. Therefore, observations may not be considered as independent in the population. In this case, statistical inferences within each cluster are preferred before cross-group analysis. Figure 4.4 illustrates the comparison between 1-level Bayesian model on the left and 2-level hierarchical Bayesian model on the right. $D_n$ represents the cluster of data with $D_n = y_1, y_2 ....y_{N_{D_n}}$, where $y_j$ represents the data point in cluster $n$ and $N_{D_n}$ gives the total number of data point in cluster $n$. In the 1-level Bayesian model, the inference of parameters $\theta$ is made over the entire population so that

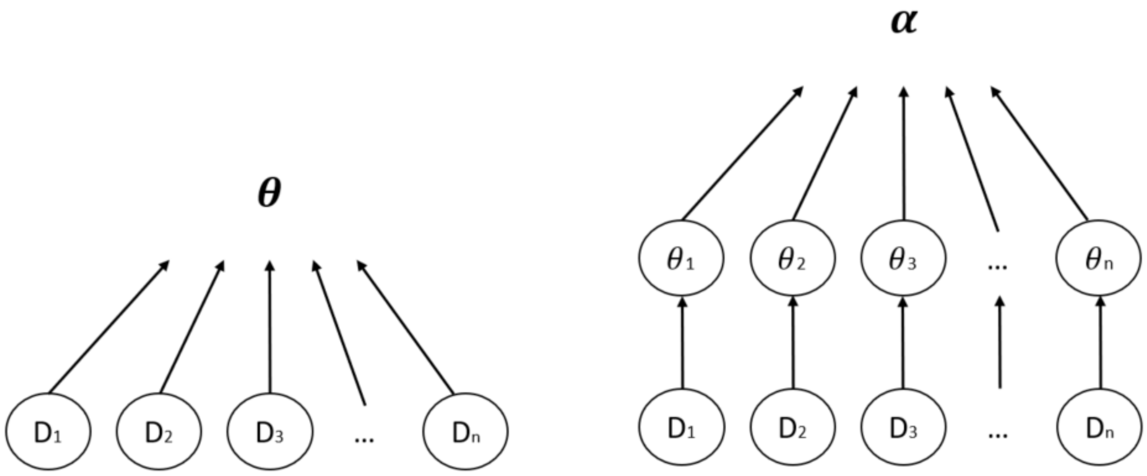

Figure 4.4: Schematic illustration of 1-level Bayesian model(left) and 2-level hierarchical Bayesian model(right).

$$p\left(\theta|y\right) \propto p\left(y|\theta\right) p(\theta), \tag{4.10}$$

where y represent the data from all clusters. With the 1-level Bayesian model, the variations of data distribution among different clusters might lead to large uncertainty in the model fitting. Therefore, an additional layer could be introduced to improve the estimation which is given by the 2-level hierarchical Bayesian model. In the base level, statistical inference of parameters was made for each cluster so that for data in cluster $D_n$

$$y_j \sim Q(\theta_n), \tag{4.11}$$

where $Q$ is some distribution with parameter $\theta_n$ which varies among cluster. In the upper level, it is assumed that all $\theta_n$s come from a common distribution $W$ with parameter $\alpha$ so that

$$\theta_n \sim W(\alpha). \tag{4.12}$$

$\alpha$ is also called hyperparameter. For the hierarchical Bayesian model, the posterior distribution is

$$p\left(\alpha, \theta|y\right) \propto p\left(y|\theta, \alpha\right) p\left(\theta|\alpha\right) p(\alpha). \tag{4.13}$$

Finally, we may only be interested in the marginal distribution of hyperparameter $\alpha$ which is

$$\begin{aligned} p\left(\alpha|y\right) &\propto \int p\left(y|\theta, \alpha\right) p\left(\theta|\alpha\right) p(\alpha) d\theta \\ &\propto L_\alpha p(\alpha) \end{aligned} \tag{4.14}$$

$$L_\alpha = \int p\left(y|\theta, \alpha\right) p\left(\theta|\alpha\right) d\theta, \tag{4.15}$$

where $L_\alpha$ is considered as the likelihood function of this Bayesian analysis. Hierarchical Bayesian model (HBM) evaluates the uncertainty due to the variations among different cluster of data by hyperparameter. As a result, HBM can be applied to study either the group distribution of a parameter measured from individuals, or the distribution of a parameter for an individual from different measurements. An example of the first type of application can be Hogg et al. (2010). Hogg et al. (2010) attempt to use HBM to study the eccentricity distribution of a group of exoplanets using their radial velocity data. In their model, the radial velocity measurements for each star $n$ can be viewed as the $D_n$. In the base level , the eccentricity $e_n$ value is measured for each star $n$. Then hyperparameter is introduced to describe the group distribution of all eccentricity values. An example of the second type of application can be Kuszlewicz et al. (2018) where they attempt to measure the stellar inclination $i_*$ of a star. In the base level of their model, they made several inferences of stellar inclination angle based on different groups of measurements. Then they introduce hyperparameter which describes the distribution of estimated stellar inclination angles from all group.

### Model

We use a two level hierarchical Bayesian model for our analysis. The measurements or data $D$ used for statistical analysis are stellar power spectrum. We adopt power spectra simulated with a reference star KIC 12069424 for a 4-year observation from Kamiaka et al. (2018). Firstly, we crop the slice of frequency covering $l = 1$ modes in the power spectrum out. An example of a slice of $l = 1$ mode is shown in the left embedded plot in Figure 4.2. Each $l = 1$ mode is considered as an individual cluster of measurements as suggested in Kuszlewicz et al. (2018). Then, we do the fitting of each slice of power spectrum using posterior sampling method (see Equation (4.8)) with modeled power spectrum given by 4.2. The summation of power $P(\nu)$ is made over $l = 1$ mode with only three folds $m = -1, 0$, and 1. Next, we embed the posterior samples of parameters from different clusters to our 2-level HBM to infer the stellar inclination angle $i_*$.

The spirit behind this approach is that since the signal to noise ratio is different for slices of $l = 1$ mode, HBM would enable us to better consider the uncertainty for each individual fitting and avoid large bias which are potentially occurring in the fitting of entire power spectrum. We are using the second type of application of HBM described in the last paragraph which is to infer a parameter from different groups of measurements hierarchically.

First, we start with fitting of $l = 1$ modes. Since only $l = 1$ mode is fitted, the number of parameters included in the fitting is smaller compared to the fitting of entire power spectrum in Kamiaka et al. (2018). The background model $N(\nu)$ is considered as flat with white noise $N_0$. The $\delta\nu$ and $i_*$ are fitted as $\delta\nu \sin i_*$ and $\delta\nu \cos i_*$. The power spectrum now takes the form of

$$P(\nu) = \sum_{m=-1}^{+1} \frac{H(n, 1, m, i_*)}{1 + 4[\nu - \nu(n, 1, m)]^2/\Gamma^2(n, 1, m)} + N_0. \tag{4.16}$$

The likelihood function is constructed as Equation (4.7). Table 4.2 lists all the parameters and their priors. We compute the posterior samples of parameters $p(\theta|y) = \frac{p(\theta)p(y|\theta)}{p(y)}$ for each $l = 1$ mode using MCMC code provided by Benomar et al. (2009).

Then, we start to embed our posterior samples from each $l = 1$ mode to the two level HBM described by Equation (4.14). It would be too computationally expensive to directly evaluate the marginalized likelihood $L_\alpha$, so we use a sampling approximation of K-element sampling

| Parameter | Prior |
|---|---|
| $\delta\nu \sin i_*$ | uniform |
| $\delta\nu \cos i_*$ | uniform |
| $\nu(n,l)$ | uniform |
| $N_0$ | uniform |
| $\Gamma$ | Jeffreys |
| $\pi\Gamma H(n,l=0)$ | Jeffreys |

Table 4.2: Parameters and priors for fitting of $l = 1$ mode of power spectrum

(Hogg et al., 2010) as suggested by Kuszlewicz et al. (2018)

$$\begin{aligned}\int f(x)p(x)dx &= \int \frac{f(x)p(x)}{q(x)}q(x)dx \\ &\approx \frac{1}{K}\sum_{k=1}^{K}\frac{f(x)^{(k)}p(x)^{(k)}}{q(x)^{(k)}},\end{aligned} \tag{4.17}$$

where $q(x)$ is the sampling distribution. In our analysis, we set the sampling distribution as the posterior distribution $q(x) = p(\theta|y) \propto p(\theta)p(y|\theta)$. Therefore, the posterior samples would become

$$\begin{aligned}p\left(\alpha|y\right) &\propto p(\alpha)\int p\left(y|\theta,\alpha\right)p\left(\theta|\alpha\right)d\theta \\ &\propto p(\alpha)\int \frac{p\left(y|\theta,\alpha\right)p\left(\theta|\alpha\right)}{p(\theta)p\left(y|\theta\right)}d\theta \\ &\propto p(\alpha)\frac{1}{K}\sum_{k=1}^{K}\frac{p\left(\theta|\alpha\right)^k}{p(\theta)^k}.\end{aligned} \tag{4.18}$$

Since the hyperparameter $\alpha$ we are about to introduce describe only the distribution of stellar inclinaton $i_*$ and we assume that probability distribution, we can assume that $p(\theta|\alpha) = p(\theta)$ for parameters apart from $i_*$. $p(\theta)$ is the prior used in the first fitting process (see table 4.2). In addition, we make an assumption that distributions of parameters are separable so that our hierarchical Bayesian model becomes

$$p\left(\alpha|y\right) \propto p(\alpha)\frac{1}{K}\sum_{k=1}^{K}\frac{p(i_*^k|\alpha)}{p(i_*^k)}, \tag{4.19}$$

where $p(i_*|\alpha)$ is the likelihood function. Then, extending the model to the full sample of $N$ $l = 1$ modes, we have the final form

$$p\left(\alpha|y\right) \propto p(\alpha)\prod_{n=1}^{N}\frac{1}{K}\sum_{k=1}^{K}\frac{p(i_*^{nk}|\alpha)}{p(i_*^{nk})}. \tag{4.20}$$

The input data $i_*^{nk}$ is the $k^{th}$ element of $i_*$ posterior samples that we computed in the first step for the $n^{th}$ $l = 1$ mode. The $p(i_*|\alpha)$ we use is a modified fisher distribution of $i_*$ introduced by Kuszlewicz et al. (2018)

$$p(i_*|\alpha(\mu,\kappa)) = exp[\kappa\cos(i-\mu)]\sin i, \tag{4.21}$$

where $\mu$ and $\kappa$ are the two hyperparameters for this model. $\mu$ is a location parameter that describes the value of stellar inclination $i_*$ and $\kappa$ is the concentration parameter of the posterior distribution. We adopt the same prior as Kuszlewicz et al. (2018) for $\mu$ and $\kappa$

$$p(\kappa|\gamma) = \frac{1}{\pi\gamma}\left(\frac{\gamma^2}{\kappa^2+\gamma^2}\right) for \kappa > 0. \tag{4.22}$$

$$p(\mu) = sin(\mu). \tag{4.23}$$

The prior of concentration parameter $\kappa$ is a Half-Cauchy prior with $\gamma = 50$. The prior of location parameter $i_*$ is an isotropic prior.

Finally, we compute the posterior sample of $p\,(\alpha|y)$ using MCMC sampling package *emcee* (Foreman-Mackey et al., 2013). We didn't use MCMC package provided by Benomar et al. (2009) in our hierarchical Bayesian analysis because this package is written in C++ and designed for fitting of power spectrum. The *emcee* is a python package which is more suitable for testing.

### 4.4.2 Fitting of Mode Height H

The second method is proposed based on the hypothesis that the correlation between $\delta\nu$ and $i_*$ bias the measurements of these two parameters (Ballot et al., 2006; Kamiaka et al., 2018). Parameter $\delta\nu$ appears in the relation between $\nu(n,l,m)$ and $\delta\nu$ given by Equation (4.6) and parameter $i_*$ comes from the function of Height $H(n,l,m,i_*) = \mathscr{E}(l,m,i_*)H(n,l)$ with $\mathscr{E}$ given by Equation (4.4). Hence, the relation between $i_*$ and $\delta\nu$ is non linear in the modeled power spectrum given by Equation (4.2). We suspect that if we fit the parameter $\delta\nu$ and $i_*$ directly as in Kamiaka et al. (2018), the complex relation mentioned above might lead to unknown bias and degeneracy.

In our attempt, we also do the posterior sampling by fitting over the entire power spectrum. However, we simplify the process by fitting $\mathscr{E}(l,m,i_*)$ and $\delta\nu$ instead of $\delta\nu$ and $i_*$ over the entire power spectrum. After collecting the posterior samples of $\mathscr{E}(l,m,i_*)$, we use a separate step to compute $i_*$. In the observed power spectrum, signal to noise ratio for $l = 3$ and above is usually too low. Therefore, we fit the $l = 1$ and $l = 2$ spectra. Since $\mathscr{E}(l,m,i_*)$ values don't vary with $n$, we will only have five values for all $l = 1$ and $l = 2$ modes in the spectrum

$$\mathscr{E}(1,0,i_*) = \cos^2 i_*, \tag{4.24}$$

$$\mathscr{E}(1,\pm1,i_*) = \frac{1}{2}\sin^2 i_*, \tag{4.25}$$

$$\mathscr{E}(2,0,i_*) = \frac{1}{4}(3\cos^2 i_* - 1)^2, \tag{4.26}$$

$$\mathscr{E}(2,\pm1,i_*) = \frac{3}{2}\cos^2 i_* \sin^2 i_*, \tag{4.27}$$

$$\mathscr{E}(2,\pm2,i_*) = \frac{3}{8}\sin^4 i_*. \tag{4.28}$$

$$\tag{4.29}$$

As we can see from the above equation, the values of $\mathscr{E}(l,m,i_*)$ sum up to 1 over all multiplets of each l mode. For example, $\mathscr{E}(1,0,i_*) + \mathscr{E}(1,1,i_*) + \mathscr{E}(1,-1,i_*) = 1$. This parameter $\mathscr{E}(l,m,i_*)$ gives an idea of relative height of multiplets in each l mode. Figure 4.3 gives an example which help us to picture the relative height of multiplets. In each box of this figure, multiplets of $l = 1$ mode is plotted. The two peaks marked by red dotted line and the one peak marked by the blue dotted line are the multiplets. We can see that their relative height changes with varying $\delta\nu/\Gamma$ and $i_*$. It is the relative height of these multiplets that we fit in our first step. The priors and model we used for the fitting of entire power spectrum all follows Kamiaka et al. (2018) except that we fit $\mathscr{E}(l, m, i_*)$ instead of $i_*$. We use Jeffreys prior for $\mathscr{E}(l, m, i_*)$. We use the MCMC package for posterior sampling provided by Benomar et al. (2009).

Next, we carry the five arrays of posterior samples of $\mathscr{E}(l, m, i_*)$ to our following analysis to extract $i_*$. As mentioned in the paragraph above, the sum of multiplets for each $l$ value is equal to 1. We compute two arrays of the normalization factor A($l = 1$) and A($l = 2$) for $l = 1$ and $l = 2$ cases respectively

$$A(l = 1) = \mathscr{E}(1, 0) + 2 * \mathscr{E}(1, \pm 1), \tag{4.30}$$

$$A(l = 2) = \mathscr{E}(2, 0) + 2 * \mathscr{E}(2, \pm 1) + 2 * \mathscr{E}(2, \pm 2), \tag{4.31}$$

and normalize the five $\mathscr{E}(l, m, i_*)$ arrays with the normalization factors so that the sum of $\mathscr{E}(l, m, i_*)$ of multiplets for each $l$ value is 1. Finally, we compute a least square fitting of posterior samples of $\mathscr{E}(l, m, i_*)$ using the model in Equation (4.24) over $i_*$ value to extract the $i_*$. By computing

$$\Delta^2_{i_*} = \sum_{l=1}^{l=2} \sum_{m=-l}^{+l} (\mathscr{E}(l, m, i_*) - \mathscr{E}(l, m, i_*)_{observed})^2, \tag{4.32}$$

over $i_* \in [0^\circ, 90^\circ]$ with a linear spacing of $0.1^\circ$, we select the $i_*$ from the minimum $\Delta^2_{i_*}$ as the stellar inclination angle.

## 4.5 Results

In this section, we summarize our results for the two attempts we made. For the test using HBM, we apply our method on the 11 most ideal simulated spectra with largest $HBR$ value and with the splitting to width ratio $\delta\nu_*/\Gamma = 1$. The only parameter that have different values for these 11 spectra is $i_*$. The case of $\delta\nu_*/\Gamma = 1$ is an ideal case for solar-type stars which rarely occurs. For solar type star the blending of multiplets are stronger, usually with $\delta\nu_*/\Gamma \approx 0.44$, so that the extraction of true $\delta\nu$ value is more challenging. Since we adopt the HBM from Kuszlewicz et al. (2018) in which they analysis red giant stars. Therefore, we choose the best $\delta\nu_*/\Gamma$ ratio in the simulated spectrum to make a comparably fair test of this method.

Figure 4.5 shows the measurements of $i_*$ using our HBM comparing with the input $i_*$ on the x-axis. We realize that the HBM method does not show obvious improvement over the past global fitting (Kamiaka et al., 2018), except for $i_* \sim 0^\circ$. We also notice that there is a severe underestimation around $i_* \in [20^\circ, 40^\circ]$. Despite that Kuszlewicz et al. (2018) also report such bias, it is less severe than us. We suspect that the modified fisher distribution is not a good approximation for $i_*$ distribution for $i_* \in [20^\circ, 40^\circ]$ where uncertainty of $i_*$ distribution is large.

To conclude, the behavior of HBM model has no clear advantage over the traditional fitting of entire spectrum (Kamiaka et al., 2018) for the most ideal group of spectrum. In addition, since our main goal for studying the stellar inclination angle is to find the portion of misaligned

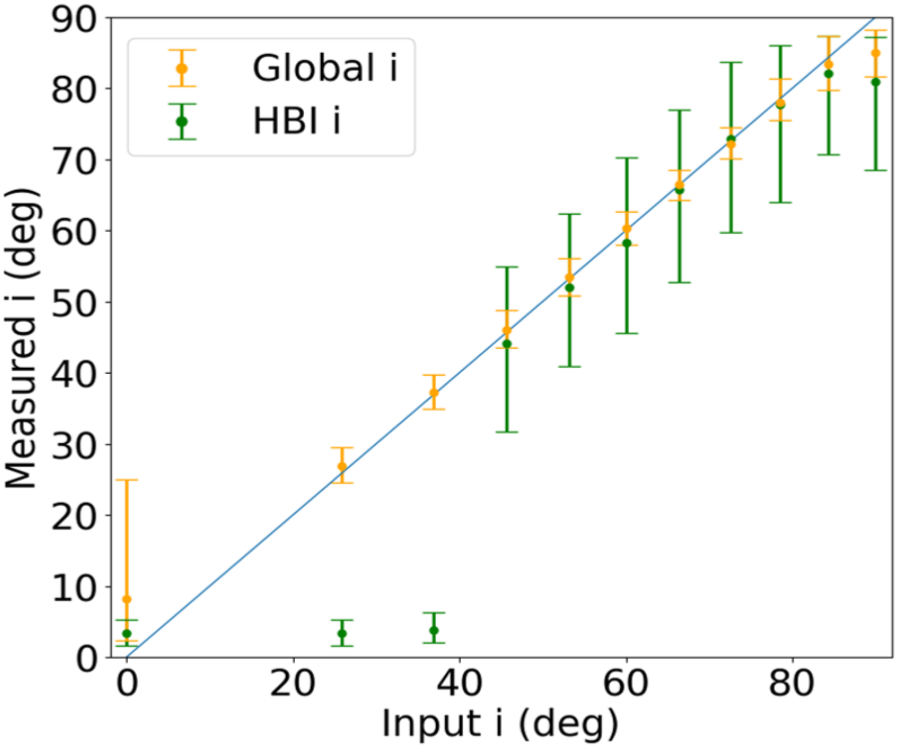

Figure 4.5: Measurements of inclination angle $i_*$ plotted against input value $i_*$ using global fitting (orange) and HBI (green).

system, the accurate measurement for $i_* \in [60°, 90°]$ is the most important. Given this perspective, the fitting of entire power spectrum seem to be a better method comparing with HBM.

Next, we perform the fitting of height method to 77 simulated spectra from Kamiaka et al. (2018) with varying $\delta/\Gamma$ and $i_*$. In Figure 4.6, we plot our measurements using red arrow in the grid space of $\delta/\Gamma$ (y-axis) and $\cos i_*$ (x-axis). The starting point of error is the true input value of these two parameters and the head of error point to the measured values. We also put the result from Kamiaka et al. (2018) for comparison. We find that our measurements better perform the estimation from Kamiaka et al. (2018) in the range of $\cos i_* \in [0.5, 0.9]$ and $\delta\nu/\Gamma \in [0.5, 1]$. However, since $\cos i_* \in [0.5, 1]$ corresponds to $i_* \in [25.8°, 60°]$, the range of improved measurements do not cover the range of $i_*$ that we are interested in.

To conclude, HBM and Fitting of height method improve the measurements near $i_* \approx 0°$ and in the range $i_* \in [25.8°, 60°]$ respectively. However, in the remaining range, these method gives poorer performance than global fitting method in Kamiaka et al. (2018). However, there is still huge space to explore for these two methods. For example, we only use slices of $l = 1$ mode in HBM which might not be enough for solar-type stars because of their more severe blending of multiplets. In addition, we could explore more distributions other than the modified Fisher distribution. Also, the least square fitting of $\mathscr{E}(l, m, i_*)$ is not the only approach to extract $i_*$ from posterior samples. We can even try to combine our two attempts. It is likely that one of these ideas could improve the measurements of $i_*$ in the range of $i_* \in [60°, 90°]$.

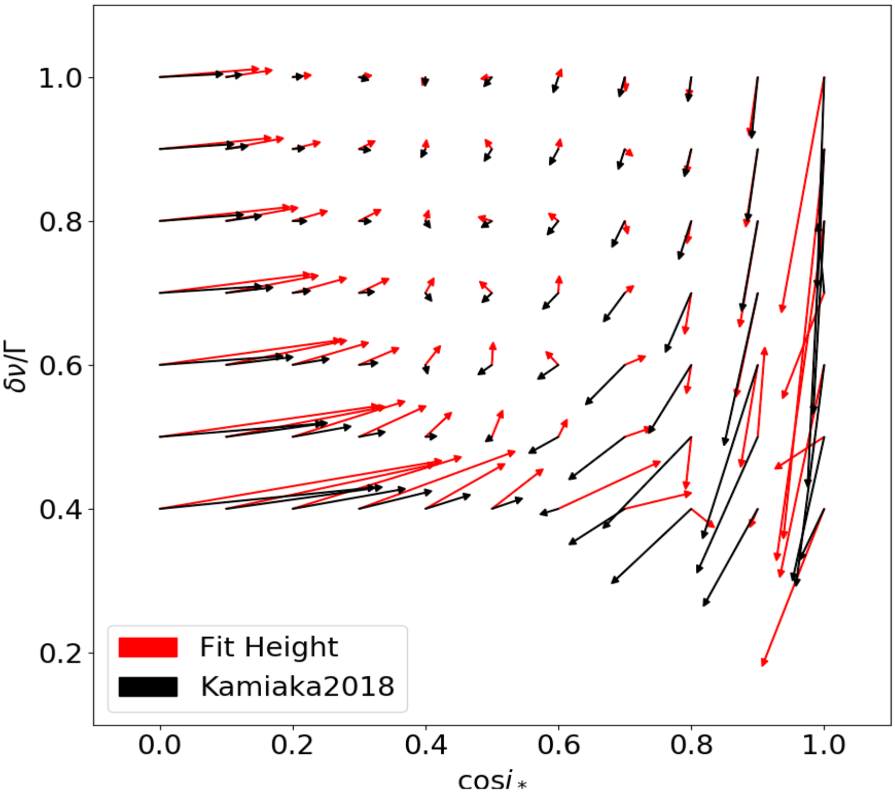

Figure 4.6: Estimations of $\delta\nu_*/\Gamma$ and stellar inclination angle $cosi_*$. The red line is given by our fitting of height method and the black line is from Kamiaka et al. (2018) using the global fitting.

# Chapter 5

# Conclusion and Future Work

There are two main parts in our work. In the first part of our thesis, we examine the three widely used photometric analyses of rotation period estimation on 91 Kepler solar-type stars (31 KOI stars and 60 non-KOI stars), which are LS periodogram, Auto-correlation function (ACF), and wavelet analysis. In general, more than 80% consistency within $1\sigma$ uncertainty is found between all three photometric methods. We noticed that when the light curve of a star contains a homogeneous variation, all photometric analyses give consistent estimation of period within $1\sigma$ uncertainty. On the other hand, when the light curve contains multiple signals, there will be multiple peaks in the power spectra. Despite three methods capture the same group of peaks, the power assigned to each peak varies among methods. Comparing with LS and ACF method, wavelet analysis (Torrence & Compo, 1998) assigns relatively higher powers to peaks at low frequency, which is due to an intrinsic bias of this method Liu et al. (2007). Mathur et al. (2010) consider this property of wavelet analysis as an advantage in that it suppresses the high frequency aliases. LS periodogram has the best frequency resolution while wavelet analysis has the most degraded resolution. As a result, wavelet analysis tends to have a larger error bar. However, we think that the major concern of photometric method is not the imprecision of estimation but rather the inaccuracy. Photometric analyses can not distinguish between signals of differential rotations and contamination from other light source. We found that more than 70% of our targets have multiple peaks in their power spectra.

We design a criteria for selecting a group of reliable $P_{photo}$. We have 22 targets in the group of reliable $P_{photo}$ and 69 targets in the group of less reliable $P_{photo}$. Then we compare our results with spectroscopic analysis. We then compare the rotational velocity $v$ computed by our photometric estimations with the reliable projected rotational velocity $v \sin i_*$ from spectroscopic analysis. 23 out of 25 targets lie in a physically meaningful region ($\sin i_* < 1$). All targets in our reliable $P_{photo}$ group are contained within the 23 targets.

Next, we compare our result $P_{photo}$ with asteroseismic estimations $P_{astero}$ from Kamiaka et al. (2018). Kamiaka et al. (2018) also divide their targets into reliable $P_{astero}$ group and less reliable $P_{astero}$ group. We first compare the 8 targets with reliable $P_{photo}$ and $P_{astero}$. 7 out of 8 targets show good consistency within $1\sigma$ uncertainty. Then we conduct a general comparison for all targets and find $\sim 80\%$ consistency. In general, photometric analyses produce reasonably reliable estimation of stellar rotation period.

Finally, we discuss about the suitability of using $P_{photo}$ as a prior to improve asteroseismic estimation of stellar inclination angle $i_*$. We suggest that reliable $P_{photo}$ are suitable choices for priors in asteroseismic analysis when they meet two criteria. Firstly, in the power spectra of the selected target, there should be only one dominant peak. Secondly, estimated $P_{photo}$ has overlapped $1\sigma$ confidence regions with $P_{astero}$. We find that the improvement in $i_*$ will be significant, as the uncertainty of less reliable $P_{astero}$ is much larger than $P_{photo}$. However, we should bear in mind that such approach has a high risk: More than 60% of stars are from binary or multiple star systems, the rotational modulation of light curve for which could be too weak to detect by photometric analysis. Under such circumstance, asteroseismic and photometric analyses are analyzing different stars so that $P_{photo}$ will not be a proper prior. To conclude, reliable $P_{photo}$ could potentially improve the asteroseismic inference of stellar inclination $i_*$ significantly. However, the selection of target should be very careful. We find 3 targets in our sample, KIC 3425851, KIC 9098294 and KIC 12258514, which could be suitable for this approach.

In the second part of our thesis, we attempt two methods to improve the results in the regime where the traditional asteroseismic analysis does not perform well. When the star rotation is slow, the traditional method of asteroseismic analysis becomes less reliable in terms of extracting stellar inclination angles and rotation periods (Ballot et al., 2006; Kamiaka et al., 2018). The previous solution is to fit the entire power spectrum of stellar oscillation modes (e.g. Gizon & Solanki, 2003). In our study, considering the global fitting can be oversensitive to any slight ill-fitting of parameters for single mode, we therefore fit all $l = 1$ modes of stellar oscillation individually to obtain posterior samples of parameters first, and then apply Hierarchical Bayesian Inference to average over all posterior samples of stellar inclination angle. Our second approach is to remove the influence of non-linear relation between the mode height and the stellar inclination from the global fitting. To achieve this, we perform the global fitting of power spectrum by fitting the mode Height H directly instead of stellar inclination. We then use the posterior sample of mode height H to further derive the inclination angle.

This project is still ongoing. We currently find that our new attempts do not improve much the measurements of $\sin i_*$ and $\delta\nu$. For Hierarchical Bayesian Inference, there is a severe underestimate in the range of $i \in [20°, 40°]$. In addition, the results of our second attempt suggests that the non-linear relation between the mode height H and stellar inclination angle $i_*$ is not largely responsible for the bias of $\sin i_*$ and $\delta\nu$ measurement.

In the future work, we would like to apply the spot modeling (e.g. Mosser et al., 2009) to our targets. Such modeling may better inform us about the latitude and configuration of star spots on the stellar surface, which possibly reveals a better picture of possible differential rotation on the stellar surface and accounts for the discrepancy between $P_{photo}$ and $P_{astero}$. We may also take the advantage of these additional constraints as a priori to improve the asteroseismic analysis. We also would like to examine the possibility of using machine learning to systematically evaluate the uncertainty of each parameters in asteroseismic analysis. We believe that such improvements of estimation of rotation periods and stellar inclination will update our current understanding of spin-orbit angle distribution measured from exoplanetary systems.

# Appendix A

# Appendix

## A.1 Modeled Power Spectrum of Asteroseismic Analysis

In this section, we summarize main steps for deriving power spectrum given in Gizon & Solanki (2003). Assuming that the intensity of fluctuation at the stellar surface is proportional to sum of scalar eigen-functions measured at the stellar surface, the brightness variations can be presented by

$$I(t,\theta,\phi) = \Re \sum_{nlmm'} f'_{nlm} Y_l^{m'}(\theta,\phi) r^{(l)}_{m'm}(i) e^{i\omega_{n,l,m}t}, \tag{A.1}$$

where $f'_{nlm}$ are the complex amplitudes, $\boldsymbol{r}^(l)$ is the rotation matrix which transform the original frame to an inertial frame with polar axis pointing toward the observer. Integrating over azimuthal and polar angle with limb-darkening function$W(\theta)$, the observed disk-integrated intensity signal,I(t) is given by:

$$I(t) = \Re \sum_{nlm} V_l f'_{nlm} r^{(l)}_{0m}(i) e^{i\omega_{nlm}t}, \tag{A.2}$$

, with the visibility factor $V_l$ given by

$$V_l = 2\pi \int_0^{\pi/2} Y_l^0(\theta) W(\theta) cos(\theta) sin(\theta) d\theta. \tag{A.3}$$

Since $Y_l^{m'}(\theta,\phi)$ is proportional to $exp(im'\phi)$, components with $m' \neq 0$ disappear after integration. Assuming equipartition of energy between modes with different azimuthal order, amplitude $f'_{nlm}$ is written as

$$f'_{nlm} = |f'nl| e^{i\phi_{nlm}}, \tag{A.4}$$

Using Matrix elements $r^{(l)}_{0m}$ given by Messiah (1959), the dependence of mode power on azimuthal order m is

$$\mathscr{E}_{lm}(i) = [r^{(l)}_{0m}(i)]^2 = \frac{(l-|m|)!}{(l+|m|)!} \left[ P_l^{|m|}(cosi) \right]^2 \tag{A.5}$$

The brightness variations can hence be approximated by

$$I(t) = \sum_{m=-l}^{l} \sqrt{\mathscr{E}(i)} cos[(\omega_{nl} + m\Omega)t + \phi_m]. \tag{A.6}$$

where the $\phi_{nlm}$ is an arbitrary phase.

The model of power spectrum can then be given by Fourier transform of $I(t)$

$$I(\omega_j) = \mathscr{F}(I(t)) \tag{A.7}$$

where $\omega_j = 2\pi j/T$ and T is the length of observation interval. Since stellar oscillations are excited stochastically by near-surface turbulent convection, followed by an exponential decay, Anderson et al. (1990) proposed that a Lorentzian line profile could be used to describe them:

$$L_{nl}(\omega) = [1 + (\frac{\omega - \omega_{nl}}{\Gamma/2})^2]^{-1}, \tag{A.8}$$

where $\omega_{nl}$ is the resonant frequency and $\Gamma$ represents the damping rate(line width parameter). The final power spectrum is thus approximated by superposition of all oscillation modes(n,l,m):

$$P(\nu) = \sum_{n=n_{min}}^{n_{max}} \sum_{l=0}^{l_{max}} \sum_{m=-l}^{+l} \frac{H(n,l,m,i_*)}{1 + 4[\nu - \nu(n,l,m)]^2/\Gamma^2(n,l,m)} + N(\nu), \tag{A.9}$$

where $N(\nu)$ is a background noise modeled as two Harvey-like profiles with white shot noise, $H(n,l,m,i_*)$ is the mode height described by $H(n,l,m,i_*) = \mathscr{E}(l,m,i_*)H(n,l)$, and $\nu(n,l,m)$ is the central frequency of mode following

$$\nu(n,l,m) = \nu(n,l) + m\delta\nu_* \approx (n + \frac{l}{2} + \eta_{n,l})\Delta\nu + \delta_{n,l} + m\delta\nu_*. \tag{A.10}$$

## A.2 Stellar Rotation Period of 91 Solar Type Stars

This section contains tables of our photometric measurements for 91 solar-type stars. In the Bin./Multi colomn, 1 indicates that there are more than 1 stars in the system while 0 indicates that there is only 1 star in the system. In planet column, 1 means that this system has planet detections while 0 means that this system has no reported planet.

| No. | target | $P_{\mathrm{LS}}$ | $P_{\mathrm{ACF}}$ | $P_{\mathrm{wavelet}}$ | Bin./Multi | Planet |
|---|---|---|---|---|---|---|
| 1 | 8077137 | $13.26^{+1.19}_{-0.81}$ | $13.29^{+1.14}_{-0.49}$ | $13.39^{+2.59}_{-2.32}$ | 0 | 1 |
| 2 | 10963065 | $12.59^{+1.09}_{-0.99}$ | $12.62^{+0.77}_{-1.03}$ | $12.49^{+2.31}_{-2.31}$ | 0 | 1 |
| 3 | 11807274 | $8.09^{+0.35}_{-0.89}$ | $7.96^{+0.34}_{-0.24}$ | $7.91^{+2.07}_{-1.55}$ | 0 | 1 |
| 4 | 1435467 | $7.07^{+0.52}_{-0.72}$ | $6.82^{+0.39}_{-0.37}$ | $6.74^{+2.56}_{-1.47}$ | 0 | 0 |
| 5 | 5773345 | $11.20^{+0.93}_{-0.61}$ | $11.23^{+0.79}_{-0.52}$ | $11.65^{+5.35}_{-2.35}$ | 0 | 0 |
| 6 | 7103006 | $4.74^{+0.17}_{-0.17}$ | $4.68^{+0.12}_{-0.12}$ | $4.73^{+1.07}_{-0.85}$ | 0 | 0 |
| 7 | 7206837 | $4.11^{+0.01}_{-0.13}$ | $4.04^{+0.08}_{-0.06}$ | $4.09^{+0.62}_{-0.59}$ | 0 | 0 |
| 8 | 12009504 | $9.62^{+0.72}_{-0.56}$ | $9.59^{+0.35}_{-0.47}$ | $9.67^{+2.28}_{-1.79}$ | 0 | 0 |
| 9 | 3425851 | $7.82^{+0.34}_{-0.20}$ | $7.87^{+0.27}_{-0.26}$ | $7.96^{+1.41}_{-1.24}$ | 0 | 1 |
| 10 | 5866724 | $8.19^{+0.56}_{-0.37}$ | $8.21^{+0.58}_{-0.35}$ | $8.18^{+1.45}_{-1.42}$ | 0 | 1 |
| 11 | 7670943 | $5.35^{+0.15}_{-0.20}$ | $5.30^{+0.13}_{-0.17}$ | $5.29^{+0.85}_{-0.89}$ | 0 | 1 |
| 12 | 8292840 | $7.09^{+1.23}_{-0.35}$ | $7.09^{+0.31}_{-0.26}$ | $7.48^{+2.70}_{-1.67}$ | 0 | 1 |
| 13 | 8349582 | $16.96^{+1.68}_{-1.02}$ | $16.87^{+1.65}_{-0.95}$ | $16.95^{+3.28}_{-3.51}$ | 0 | 1 |
| 14 | 9414417 | $10.75^{+0.63}_{-0.39}$ | $10.86^{+0.53}_{-0.49}$ | $10.87^{+1.66}_{-1.57}$ | 0 | 1 |
| 15 | 2837475 | $3.68^{+0.07}_{-0.05}$ | $3.66^{+0.08}_{-0.04}$ | $3.84^{+1.80}_{-0.90}$ | 0 | 0 |
| 16 | 3656476 | $16.91^{+2.11}_{-1.35}$ | $17.07^{+2.36}_{-0.57}$ | $16.95^{+3.28}_{-3.42}$ | 0 | 0 |
| 17 | 6933899 | $16.18^{+1.05}_{-1.58}$ | $15.50^{+1.17}_{-0.95}$ | $15.81^{+3.32}_{-3.45}$ | 0 | 0 |
| 18 | 7771282 | $12.28^{+0.24}_{-1.02}$ | $12.05^{+0.39}_{-0.82}$ | $11.90^{+2.11}_{-2.00}$ | 0 | 0 |
| 19 | 7940546 | $11.70^{+0.96}_{-0.88}$ | $11.62^{+1.05}_{-0.60}$ | $11.74^{+2.66}_{-2.30}$ | 0 | 0 |
| 20 | 9098294 | $19.31^{+2.74}_{-0.84}$ | $20.12^{+1.86}_{-1.63}$ | $20.15^{+3.24}_{-3.03}$ | 0 | 0 |

Table A.1: Stellar rotation period.

| No. | target | $P_{\mathrm{LS}}$ | $P_{\mathrm{ACF}}$ | $P_{\mathrm{wavelet}}$ | Bin./Multi | Planet |
|---|---|---|---|---|---|---|
| 21 | 10454113 | $14.55^{+1.20}_{-1.04}$ | $14.33^{+0.98}_{-0.83}$ | $14.75^{+2.49}_{-2.30}$ | 0 | 0 |
| 22 | 12258514 | $15.24^{+1.05}_{-1.16}$ | $14.92^{+1.23}_{-0.80}$ | $14.85^{+2.75}_{-2.91}$ | 0 | 0 |
| 23 | 3544595 | $15.09^{+1.13}_{-1.75}$ | $14.83^{+0.66}_{-1.34}$ | $14.65^{+3.70}_{-2.95}$ | 0 | 1 |
| 24 | 4141376 | $13.54^{+1.30}_{-0.98}$ | $13.71^{+0.91}_{-1.35}$ | $13.48^{+3.64}_{-3.23}$ | 0 | 1 |
| 25 | 6521045 | $13.78^{+0.77}_{-2.37}$ | $13.71^{+0.77}_{-1.27}$ | $13.11^{+3.20}_{-3.41}$ | 0 | 1 |
| 26 | 8494142 | $14.24^{+0.98}_{-1.49}$ | $14.10^{+0.38}_{-1.31}$ | $13.76^{+4.72}_{-3.65}$ | 0 | 1 |
| 27 | 9955598 | $13.01^{+2.35}_{-1.65}$ | $12.98^{+2.40}_{-1.32}$ | $13.11^{+4.37}_{-3.21}$ | 0 | 1 |
| 28 | 11401755 | $16.82^{+2.16}_{-1.10}$ | $17.38^{+1.00}_{-1.57}$ | $16.60^{+3.77}_{-4.23}$ | 0 | 1 |
| 29 | 4914923 | $7.93^{+0.47}_{-0.20}$ | $7.89^{+0.39}_{-0.18}$ | $14.55^{+6.39}_{-7.20}$ | 0 | 0 |
| 30 | 6225718 | $35.37^{+8.57}_{-5.92}$ | $33.92^{+7.41}_{-4.67}$ | $35.09^{+7.96}_{-6.88}$ | 0 | 0 |
| 31 | 6679371 | $5.80^{+0.05}_{-0.25}$ | $5.68^{+0.14}_{-0.14}$ | $15.06^{+3.68}_{-10.31}$ | 0 | 0 |
| 32 | 7510397 | $33.50^{+12.20}_{-4.19}$ | $39.63^{+5.76}_{-7.82}$ | $35.33^{+13.10}_{-20.53}$ | 1 | 0 |
| 33 | 7680114 | $30.83^{+13.19}_{-6.36}$ | $30.02^{+1.54}_{-5.49}$ | $28.50^{+18.61}_{-7.12}$ | 0 | 0 |
| 34 | 7871531 | $32.28^{+10.11}_{-1.82}$ | $35.01^{+7.49}_{-4.10}$ | $35.09^{+6.21}_{-6.49}$ | 0 | 0 |
| 35 | 7970740 | $13.48^{+1.08}_{-0.71}$ | $13.48^{+1.12}_{-0.56}$ | $13.96^{+7.42}_{-3.98}$ | 0 | 0 |
| 36 | 8006161 | $33.04^{+9.43}_{-4.22}$ | $32.37^{+9.69}_{-2.83}$ | $33.89^{+7.98}_{-6.65}$ | 0 | 0 |
| 37 | 8179536 | $5.35^{+0.20}_{-0.26}$ | $13.17^{+0.23}_{-1.18}$ | $5.40^{+1.32}_{-1.00}$ | 0 | 0 |
| 38 | 8379927 | $17.06^{+1.71}_{-0.97}$ | $17.33^{+1.39}_{-1.22}$ | $17.30^{+2.64}_{-2.60}$ | 1 | 0 |
| 39 | 8394589 | $11.50^{+1.25}_{-0.94}$ | $11.53^{+0.89}_{-0.38}$ | $11.74^{+5.27}_{-3.23}$ | 0 | 0 |
| 40 | 9025370 | $12.35^{+3.59}_{-0.80}$ | $29.80^{+8.50}_{-4.59}$ | $30.97^{+8.10}_{-11.84}$ | 1 | 0 |

Table A.2: Stellar rotation period.

| No. | target | $P_{\mathrm{LS}}$ | $P_{\mathrm{ACF}}$ | $P_{\mathrm{wavelet}}$ | Bin./Multi | Planet |
|---|---|---|---|---|---|---|
| 41 | 9139151 | $6.30^{+0.22}_{-0.28}$ | $14.10^{+0.38}_{-1.42}$ | $12.07^{+7.20}_{-3.44}$ | 1 | 0 |
| 42 | 9139163 | $5.91^{+0.25}_{-0.14}$ | $16.41^{+2.67}_{-3.37}$ | $15.81^{+23.53}_{-5.98}$ | 1 | 0 |
| 43 | 9965715 | $20.69^{+2.64}_{-2.42}$ | $20.39^{+1.35}_{-2.29}$ | $20.29^{+5.84}_{-7.32}$ | 0 | 0 |
| 44 | 11253226 | $3.80^{+0.04}_{-0.09}$ | $13.32^{+0.26}_{-1.23}$ | $12.93^{+8.00}_{-9.93}$ | 0 | 0 |
| 45 | 3632418 | $12.68^{+1.07}_{-0.72}$ | $12.74^{+0.65}_{-0.80}$ | $12.75^{+2.57}_{-2.21}$ | 0 | 1 |
| 46 | 4143755 | $15.17^{+12.07}_{-2.16}$ | $15.26^{+2.06}_{-2.26}$ | $15.59^{+18.89}_{-4.61}$ | 0 | 1 |
| 47 | 4349452 | $22.25^{+3.62}_{-1.23}$ | $22.49^{+3.36}_{-1.36}$ | $22.99^{+4.07}_{-12.37}$ | 0 | 1 |
| 48 | 4914423 | $19.40^{+4.68}_{-3.45}$ | $21.72^{+2.09}_{-4.77}$ | $19.33^{+5.74}_{-10.47}$ | 0 | 1 |
| 49 | 5094751 | $7.29^{+0.35}_{-0.25}$ | $16.50^{+0.85}_{-3.10}$ | $15.06^{+6.46}_{-8.48}$ | 0 | 1 |
| 50 | 6196457 | $16.25^{+1.89}_{-1.13}$ | $16.02^{+1.74}_{-0.88}$ | $16.14^{+3.12}_{-3.69}$ | 0 | 1 |
| 51 | 7296438 | $26.42^{+3.02}_{-3.50}$ | $25.77^{+3.27}_{-3.22}$ | $25.86^{+5.22}_{-4.49}$ | 1 | 1 |
| 52 | 8478994 | $32.83^{+9.88}_{-6.33}$ | $33.64^{+9.79}_{-2.88}$ | $33.89^{+7.98}_{-9.34}$ | 1 | 1 |
| 53 | 8554498 | $13.25^{+3.99}_{-1.16}$ | $42.88^{+3.74}_{-10.98}$ | $35.33^{+11.78}_{-27.12}$ | 1 | 1 |
| 54 | 9592705 | $13.67^{+0.80}_{-0.95}$ | $13.10^{+1.33}_{-0.30}$ | $13.57^{+2.62}_{-2.28}$ | 1 | 1 |
| 55 | 10586004 | $10.10^{+0.42}_{-0.62}$ | $9.86^{+0.45}_{-0.44}$ | $14.85^{+22.88}_{-6.70}$ | 0 | 1 |
| 56 | 10666592 | $32.77^{+11.76}_{-7.08}$ | $32.11^{+11.00}_{-6.14}$ | $32.74^{+11.83}_{-11.51}$ | 0 | 1 |
| 57 | 11133306 | $15.75^{+2.60}_{-2.28}$ | $15.85^{+2.12}_{-2.57}$ | $15.70^{+5.23}_{-3.34}$ | 0 | 1 |
| 58 | 11295426 | $32.90^{+12.09}_{-5.80}$ | $35.01^{+10.04}_{-7.30}$ | $32.96^{+13.82}_{-7.54}$ | 1 | 1 |
| 59 | 11853905 | $35.63^{+9.15}_{-16.00}$ | $38.86^{+6.88}_{-7.30}$ | $34.84^{+9.41}_{-15.04}$ | 1 | 1 |
| 60 | 11904151 | $15.40^{+4.41}_{-2.39}$ | $14.22^{+4.22}_{-0.65}$ | $15.59^{+5.20}_{-3.57}$ | 0 | 1 |

Table A.3: Stellar rotation period.

| No. | target | $P_{\mathrm{LS}}$ | $P_{\mathrm{ACF}}$ | $P_{\mathrm{wavelet}}$ | Bin./Multi | Planet |
|---|---|---|---|---|---|---|
| 61 | 3427720 | $13.18^{+1.50}_{-0.68}$ | $13.24^{+1.45}_{-0.42}$ | $13.48^{+2.50}_{-2.64}$ | 1 | 0 |
| 62 | 3456181 | $28.85^{+4.77}_{-6.83}$ | $11.56^{+0.77}_{-0.46}$ | $27.72^{+7.49}_{-16.88}$ | 0 | 0 |
| 63 | 3735871 | $12.77^{+1.21}_{-1.94}$ | $12.93^{+0.98}_{-0.73}$ | $12.40^{+3.13}_{-3.60}$ | 0 | 0 |
| 64 | 5184732 | $6.70^{+0.31}_{-0.32}$ | $6.69^{+0.21}_{-0.34}$ | $18.04^{+4.87}_{-12.31}$ | 0 | 0 |
| 65 | 5950854 | $31.44^{+16.16}_{-10.88}$ | $32.02^{+19.17}_{-13.24}$ | $30.97^{+15.81}_{-11.57}$ | 0 | 0 |
| 66 | 6106415 | $28.39^{+21.37}_{-13.62}$ | $36.06^{+13.04}_{-8.55}$ | $28.30^{+20.13}_{-15.68}$ | 0 | 0 |
| 67 | 6116048 | $16.81^{+2.28}_{-1.56}$ | $16.85^{+2.29}_{-1.36}$ | $16.71^{+3.79}_{-5.18}$ | 0 | 0 |
| 68 | 6508366 | $6.87^{+0.35}_{-0.20}$ | $6.84^{+0.38}_{-0.08}$ | $3.87^{+4.06}_{-0.78}$ | 0 | 0 |
| 69 | 6603624 | $35.01^{+7.99}_{-7.10}$ | $33.64^{+5.93}_{-5.08}$ | $32.74^{+10.31}_{-6.78}$ | 0 | 0 |
| 70 | 7106245 | $36.89^{+15.82}_{-11.88}$ | $12.54^{+0.80}_{-0.62}$ | $36.32^{+15.58}_{-27.46}$ | 0 | 0 |
| 71 | 8150065 | $45.39^{+14.70}_{-7.84}$ | $45.13^{+14.43}_{-7.55}$ | $45.66^{+10.75}_{-8.44}$ | 0 | 0 |
| 72 | 8228742 | $19.90^{+2.88}_{-2.76}$ | $19.22^{+2.40}_{-2.02}$ | $19.46^{+4.92}_{-10.23}$ | 0 | 0 |
| 73 | 8424992 | $33.68^{+11.07}_{-6.28}$ | $35.21^{+9.34}_{-3.40}$ | $36.07^{+9.11}_{-10.48}$ | 0 | 0 |
| 74 | 8694723 | $7.87^{+0.15}_{-0.42}$ | $15.78^{+0.88}_{-1.25}$ | $7.91^{+10.96}_{-1.72}$ | 0 | 0 |
| 75 | 8760414 | $34.96^{+9.14}_{-3.66}$ | $34.91^{+9.31}_{-3.10}$ | $36.58^{+7.07}_{-6.56}$ | 0 | 0 |
| 76 | 8938364 | $16.58^{+1.50}_{-3.16}$ | $16.52^{+0.80}_{-1.63}$ | $15.59^{+4.35}_{-4.22}$ | 0 | 0 |
| 77 | 9206432 | $9.96^{+0.68}_{-0.66}$ | $9.94^{+0.77}_{-0.38}$ | $9.94^{+2.95}_{-3.40}$ | 0 | 0 |
| 78 | 9353712 | $11.00^{+4.45}_{-0.87}$ | $14.98^{+0.39}_{-1.49}$ | $11.90^{+6.45}_{-3.57}$ | 0 | 0 |
| 79 | 9410862 | $12.31^{+1.57}_{-1.72}$ | $11.33^{+1.66}_{-0.77}$ | $11.98^{+3.13}_{-2.55}$ | 0 | 0 |
| 80 | 9812850 | $4.84^{+0.23}_{-0.15}$ | $6.77^{+0.30}_{-0.60}$ | $5.47^{+3.27}_{-1.37}$ | 0 | 0 |

Table A.4: Stellar rotation period.

| No. | target | $P_{\mathrm{LS}}$ | $P_{\mathrm{ACF}}$ | $P_{\mathrm{wavelet}}$ | Bin./Multi | Planet |
|---|---|---|---|---|---|---|
| 81 | 10068307 | $9.34^{+0.59}_{-0.38}$ | $9.33^{+0.65}_{-0.15}$ | $19.60^{+10.01}_{-5.79}$ | 0 | 0 |
| 82 | 10079226 | $14.87^{+1.89}_{-0.50}$ | $15.76^{+0.75}_{-1.37}$ | $15.27^{+2.95}_{-3.33}$ | 0 | 0 |
| 83 | 10162436 | $11.92^{+2.68}_{-1.11}$ | $12.30^{+1.00}_{-1.12}$ | $12.23^{+6.25}_{-2.73}$ | 0 | 0 |
| 84 | 10516096 | $6.90^{+0.34}_{-0.35}$ | $6.75^{+0.37}_{-0.20}$ | $19.20^{+4.85}_{-13.02}$ | 0 | 0 |
| 85 | 10644253 | $33.31^{+11.45}_{-3.64}$ | $34.02^{+8.63}_{-4.33}$ | $34.60^{+15.53}_{-6.40}$ | 0 | 0 |
| 86 | 10730618 | $8.90^{+0.59}_{-0.77}$ | $9.23^{+0.19}_{-1.12}$ | $8.55^{+2.58}_{-2.45}$ | 0 | 0 |
| 87 | 11081729 | $2.70^{+0.04}_{-0.05}$ | $12.44^{+0.93}_{-0.48}$ | $2.78^{+2.31}_{-0.56}$ | 0 | 0 |
| 88 | 11772920 | $16.10^{+1.69}_{-1.67}$ | $15.72^{+2.01}_{-0.62}$ | $16.37^{+24.64}_{-4.43}$ | 0 | 0 |
| 89 | 12069127 | $17.37^{+1.63}_{-3.13}$ | $17.36^{+1.42}_{-1.60}$ | $16.83^{+5.30}_{-3.85}$ | 0 | 0 |
| 90 | 12069449 | $34.15^{+8.56}_{-6.90}$ | $14.51^{+0.66}_{-1.21}$ | $34.13^{+7.74}_{-13.48}$ | 0 | 0 |
| 91 | 12317678 | $13.36^{+4.97}_{-1.12}$ | $13.48^{+1.99}_{-1.18}$ | $14.15^{+32.95}_{-4.32}$ | 0 | 0 |

Table A.5: Stellar rotation period.

# Bibliography

Aguirre, V. S., Lund, M. N., Antia, H. M., et al. 2017, The Astrophysical Journal, 835, 173,

Ahlers, J. P., Kruse, E., Colón, K. D., et al. 2020, The Astrophysical Journal, 888, 63,

Albrecht, S., Winn, J. N., Butler, R. P., et al. 2011, The Astrophysical Journal, 744, 189,

Alecian, E., Wade, G. A., Catala, C., et al. 2013, MNRAS, 429, 1001,

Anderson, D. R., Triaud, A. H. M. J., Turner, O. D., et al. 2015, ApJ, 800, L9,

Anderson, D. R., Temple, L. Y., Nielsen, L. D., et al. 2018, arXiv e-prints, arXiv:1809.04897.

Anderson, E. R., Duvall, Thomas L., J., & Jefferies, S. M. 1990, ApJ, 364, 699,

Appourchaux, T., Gizon, L., & Rabello-Soares, M.-C. 1998, Astron. Astrophys. Suppl. Ser., 132, 107,

Appourchaux, T., Michel, E., Auvergne, M., et al. 2008, A&A, 488, 705,

Ballot, J., Appourchaux, T., & Toutain, T. 2008, Astronomische Nachrichten, 329, 558,

Ballot, J., García, R. A., & Lambert, P. 2006, Monthly Notices of the Royal Astronomical Society, 369, 1281,

Ballot, J., Barban, C., & Van´t Veer-Menneret, C. 2011, A&A, 531, A124,

Baluev, R. V. 2008, Mon. Not. R. Astron. Soc, 385, 1279,

Barclay, T., Rowe, J. F., Lissauer, J. J., et al. 2013, Nature, 494, 452,

Basu, S., Chaplin, W. J., Elsworth, Y., New, R., & Serenelli, A. M. 2009, The Astrophysical Journal, 699, 1403,

Bate, M. R., Lodato, G., & Pringle, J. E. 2010, Monthly Notices of the Royal Astronomical Society, 401, 1505,

Batygin, K. 2012, Nature, 491, 418,

Benomar, O. 2008, Communications in Asteroseismology, 157, 98

Benomar, O., Appourchaux, T., & Baudin, F. 2009, A&A, 506, 15,

Benomar, O., Masuda, K., Shibahashi, H., & Suto, Y. 2014, Publications of the Astronomical Society of Japan, 66, Benomar, O., Bazot, M., Nielsen, M. B., et al. 2018, Science, 361, 1231,

Berdyugina, S. V. 2005, Living Reviews in Solar Physics, 2, 1,

Borucki, W. J., Koch, D., Basri, G., et al. 2010, Science, 327, 977,

Boué, G., Montalto, M., Boisse, I., Oshagh, M., & Santos, N. C. 2013, A&A, 550, A53,

Bourrier, V., Lovis, C., Beust, H., et al. 2018, Nature, 553, 477,

Bourrier, V., Ehrenreich, D., Lendl, M., et al. 2020, A&A, 635, A205,

Bouvier, J. 2013, in EAS Publications Series, Vol. 62, EAS Publications Series, ed. P. Hennebelle & C. Charbonnel, 143–168

Brown, A. G., Vallenari, A., Prusti, T., & de Bruijne, J. H. 2020, Astronomy & Astrophysics, 61,

Bruntt, H., Basu, S., Smalley, B., et al. 2012, Monthly Notices of the Royal Astronomical Society, 423, 122,

Burke, C. J., Bryson, S. T., Mullally, F., et al. 2014, Astrophysical Journal, Supplement Series, 210, 19,

Carroll, J. A. 1928, Monthly Notices of the Royal Astronomical Society, 88, 548,

—. 1933, Monthly Notices of the Royal Astronomical Society, 93, 478,

Carter, J. A., Agol, E., Chaplin, W. J., et al. 2012, Science, 337, 556,

Cegla, H. M., Lovis, C., Bourrier, V., et al. 2016, A&A, 588, A127,

Ceillier, T., Van Saders, J., García, R. A., et al. 2016, MNRAS, 456, 119,

Chaplin, W. J., Kjeldsen, H., Christensen-Dalsgaard, J., et al. 2011, Science, 332, 213,

Chaplin, W. J., Basu, S., Huber, D., et al. 2014, ApJS, 210, 1,

Chaplin, W. J., Houdek, G., Appourchaux, T., et al. 2008, A&A, 485, 813,

Chatterjee, S., Ford, E. B., Matsumura, S., & Rasio, F. A. 2008, ApJ, 686, 580,

Dai, F., & Winn, J. N. 2017, AJ, 153, 205,

Damasso, M., Biazzo, K., Bonomo, A. S., et al. 2015, A&A, 575, A111,

Davenport, J. R. A., Hebb, L., & Hawley, S. L. 2015, The Astrophysical Journal, 806, 212,

Désert, J.-M., Charbonneau, D., Demory, B.-O., et al. 2011, ApJS, 197, 14,

Duvall Jr, T., & Harvey, J. 1986

Esposito, M., Covino, E., Desidera, S., et al. 2017, A&A, 601, A53,

Fabrycky, D., & Tremaine, S. 2007, The Astrophysical Journal, 669, 1298,

Farge, M. 1992, Annual Review of Fluid Mechanics, 24, 395, Foreman-Mackey, D., Hogg, D. W., Lang, D., & Goodman, J. 2013, Publications of the Astronomical Society of the Pacific, 125, 306,

García, R. A., Ceillier, T., Salabert, D., et al. 2014, Astronomy & Astrophysics, 572, A34,

Gaudi, B. S., & Winn, J. N. 2007, The Astrophysical Journal, 655, 550,

Gizon, L., & Solanki, S. K. 2003, The Astrophysical Journal, 589, 1009,

Goldreich, P., & Kumar, P. 1988, ApJ, 326, 462,

Gregory, S. G., Donati, J. F., Morin, J., et al. 2012, ApJ, 755, 97,

Groth, E. J. 1975, The Astrophysical Journal Supplement Series, 29, 285,

Hall, D. S., & Henry, G. W. 1994, International Amateur-Professional Photoelectric Photometry Communications, 55, 51

Hébrard, G., Evans, T. M., Alonso, R., et al. 2011, A&A, 533, A130,

Hirano, T., Sanchis-Ojeda, R., Takeda, Y., et al. 2012, The Astrophysical Journal, 756, 66,

—. 2014, The Astrophysical Journal, 783, 9,

Hirano, T., Suto, Y., Winn, J. N., et al. 2011, The Astrophysical Journal, 742, 69,

Hogg, D. W., Myers, A. D., & Bovy, J. 2010, The Astrophysical Journal, 725, 2166,

Howard, R., & Harvey, J. 1970, Sol. Phys., 12, 23,

Howarth, I. D., & Morello, G. 2017, MNRAS, 470, 932,

Huber, D., Bedding, T. R., Stello, D., et al. 2011, The Astrophysical Journal, 743, 143,

Huber, D., Carter, J. A., Barbieri, M., et al. 2013, Science, 342, 331,

Kamiaka, S., Benomar, O., & Suto, Y. 2018, Monthly Notices of the Royal Astronomical Society, 479, 391,

Kamiaka, S., Benomar, O., Suto, Y., et al. 2019, The Astronomical Journal, 157, 137,

Karoff, C., Metcalfe, T. S., Chaplin, W. J., et al. 2013, MNRAS, 433, 3227,

Kovacs, Geza. 2018, A&A, 612, L2,

Kozai, Y. 1962, AJ, 67, 591,

Kraft, R. P. 1967, ApJ, 150, 551,

Kuszlewicz, J. S., Chaplin, W. J., North, T. S. H., et al. 2018, Bayesian hierarchical inference of asteroseismic inclination angles, Tech. rep.

Lai, D., Foucart, F., & Lin, D. N. C. 2011, Monthly Notices of the Royal Astronomical Society, 412, 2790,

Ledoux, P. 1951, ApJ, 114, 373,

Leighton, R. B., Noyes, R. W., & Simon, G. W. 1962, ApJ, 135, 474,

Lendl, M., Triaud, A. H. M. J., Anderson, D. R., et al. 2014, A&A, 568, A81,

Lidov, M. L. 1962, Planet. Space Sci., 9, 719,

Lin, D. N. C., & Ida, S. 1997, The Astrophysical Journal, 477, 781,

Liu, Y., Liang, X. S., & Weisberg, R. H. 2007, Journal of Atmospheric and Oceanic Technology, 24, 2093,

Lomb, N. R. 1976, Astrophysics and Space Science, 39, 447,

Lund, M. N., Aguirre, V. S., Davies, G. R., et al. 2017, The Astrophysical Journal, 835, 172,

Mabelcalim. 2014, waipy, `https://github.com/mabelcalim/waipy`, GitHub

Mancini, L., Esposito, M., Covino, E., et al. 2015, A&A, 579, A136,

Mancini, L., Esposito, M., Covino, E., et al. 2018, A&A, 613, A41,

Marcy, G. W., Isaacson, H., Howard, A. W., et al. 2014, The Astrophysical Journal Supplement Series, 210, 20,

Mathur, S., García, R. A., Régulo, C., et al. 2010, A&A, 511, A46,

Mayor, M., & Queloz, D. 1995, Nature, 378, 355,

McLaughlin, D. B. 1924, ApJ, 60, 22,

McQuillan, A., Aigrain, S., & Mazeh, T. 2013a, Monthly Notices of the Royal Astronomical Society, 432, 1203,

McQuillan, A., Mazeh, T., & Aigrain, S. 2013b, The Astrophysical Journal Letters, 775, L11,

—. 2014, The Astrophysical Journal Supplement Series, 211, 24,

Messiah, A. 1959, Mécanique Quantique, Tome 2 (Reading, Massachusetts: Dunod, Paris)

Molenda-Żakowicz, J., Sousa, S. G., Frasca, A., et al. 2013, Monthly Notices of the Royal Astronomical Society, 434, 1422,

Mosser, B., Baudin, F., Lanza, A. F., et al. 2009, Astronomy & Astrophysics, 506, 245,

Mosser, B., Michel, E., Belkacem, K., et al. 2013, A&A, 550, A126,

Naoz, S., Farr, W. M., Lithwick, Y., Rasio, F. A., & Teyssandier, J. 2011, Nature, 473, 187,

Nielsen, M. B., Gizon, L., Schunker, H., & Karoff, C. 2013, A&A, 557, 10,

Ohta, Y., Taruya, A., & Suto, Y. 2005, The Astrophysical Journal, 622, 1118,

Petigura, E. A., Howard, A. W., Marcy, G. W., et al. 2017, The Astronomical Journal, 154, 107,

Reinhold, T., & Reiners, A. 2013, Astronomy & Astrophysics, 557, A11, Ricker, G. R., Winn, J. N., Vanderspek, R., et al. 2015, Journal of Astronomical Telescopes, Instruments, and Systems, 1, 014003,

Rogers, T. M., Lin, D. N. C., & Lau, H. H. B. 2012, The Astrophysical Journal, 758, L6,

Rossiter, R. A. 1924, ApJ, 60, 15,

Rowe, J. F., Bryson, S. T., Marcy, G. W., et al. 2014, The Astrophysical Journal, 784, 45,

Sanchis-Ojeda, R., Winn, J. N., Holman, M. J., et al. 2011, ApJ, 733, 127,

Sanchis-Ojeda, R., Winn, J. N., Marcy, G. W., et al. 2013, ApJ, 775, 54,

Scargle, J. D. 1982, The Astrophysical Journal, 263, 835,

Southworth, J. 2011, Monthly Notices of the Royal Astronomical Society, 417, 2166,

Spalding, C., & Batygin, K. 2015, ApJ, 811, 82,

Stassun, K. G., Collins, K. A., & Gaudi, B. S. 2017, The Astronomical Journal, 153, 136,

Strassmeier, K. G. 1999, A&A, 347, 225

Strassmeier, K. G., & Bartus, J. 2000, A&A, 354, 537

Stumpe, M. C., Smith, J. C., Catanzarite, J. H., et al. 2014, Publications of the Astronomical Society of the Pacific, 126, 100,

Takaishi, D., Tsukamoto, Y., & Suto, Y. 2020, Monthly Notices of the Royal Astronomical Society, 492, 5641,

Tassoul, M. 1980, ApJS, 43, 469,

Thompson, M. J., Toomre, J., Anderson, E. R., et al. 1996, Science, 272, 1300,

Torrence, C., & Compo, G. P. 1998, Bulletin of the American Meteorological Society, 79, 61,

Ulrich, R. K. 1970, ApJ, 162, 993,

VanderPlas, J., Connolly, A. J., Ivezić, ., & Gray, A. 2012, in 2012 Conference on Intelligent Data Understanding, 47–54

VanderPlas, J. T. 2018, The Astrophysical Journal Supplement Series, 236, 16,

Vanderplas, J. T., & Ivezić, Ž. 2015, Astrophysical Journal, 812, 18,

Virtanen, P., Gommers, R., Oliphant, T. E., et al. 2020, Nature Methods, 17, 261,

Vogt, S. S., Hatzes, A. P., Misch, A. A., & Kürster, M. 1999, ApJS, 121, 547,

Winn, J. N. 2010, arXiv e-prints, arXiv:1001.2010.

Winn, J. N., Fabrycky, D., Albrecht, S., & Johnson, J. A. 2010, The Astrophysical Journal, 718, L145,

Winn, J. N., Johnson, J. A., Albrecht, S., et al. 2009, ApJ, 703, L99, Winn, J. N., Holman, M. J., Henry, G. W., et al. 2007, AJ, 133, 1828,

Winn, J. N., Petigura, E. A., Morton, T. D., et al. 2017, The Astronomical Journal, 154, 270,

Zechmeister, M., & Kürster, M. 2009, Astronomy & Astrophysics, 496, 577,

Zhou, G., Rodriguez, J. E., Collins, K. A., et al. 2016, AJ, 152, 136,